Biopolymeric Photonic Structures: Design, Fabrication, and Emerging Applications

Rui Xiong[1], Jingyi Luan[2], Saewon Kang[1], Chunhong Ye,[3] Srikanth Singamaneni[2], Vladimir V. Tsukruk[1]*

[1] School of Materials Science and Engineering, Georgia Institute of Technology, Atlanta, GA 30332-0245, USA

[2] Department of Mechanical Engineering and Materials Science, Institute of Materials Science and Engineering, Washington University in St. Louis, St Louis, MO, 63130, USA

[3] School of Physical Science and Technology, ShanghaiTech University, Shanghai 201210, China

Abstract

Biological photonic structures demonstrate exquisite control of light propagation, scattering, and emission *via* hierarchical structural organization and diverse chemistry, enabling great potential in biophotonic applications for transparency, camouflaging, protection, mimicking, signaling, and mating. Corresponding natural polymers are promising building blocks for constructing synthetic multifunctional photonic structures owing to their renewability, biocompatibility, mechanical robustness, ambient processing conditions, and diverse surface chemistry. In this review, we provide a summary of the light phenomena in biophotonic structures found in nature, the selection of corresponding biopolymers for synthetic photonic structures, the fabrication strategies for flexible photonics, and corresponding emerging photonic-related applications. We introduce various photonic structures, including multi-layered, opals, waveguiding, lasing, chiral structures, as well as photonic networks in contrast to traditionally considered light absorption and structural photonics. Next, we summarize the bottom-up and top-down fabrication approaches and physical properties of organized biopolymers and highlight the advantages of biopolymers as building blocks for realizing unique bioenabled photonic structures. Furthermore, we consider the integration of synthetic optically-active nanocomponents into organized hierarchical biopolymer frameworks for added optical functionalities, such as enhanced iridescence and chiral photoluminescence. Finally, we present an outlook on current trends in biophotonic materials design and fabrication, including current issues, critical fundamentals, as well as promising emerging photonic applications.

Key words: Natural biopolymers; hierarchical organization; biophotonic structures; nanocelluloses; silk proteins; structural colors

*E-mail: vladimir@mse.gatech.edu

1. Introduction

Photonic structures which are capable of manipulating light at multi-length scales *via* hierarchical micro/nano structural organization enable various optical applications related to vision enhancement, camouflaging, energy harvesting, light actuation and colometric biosensing.[1,2,3,4] However, a longstanding challenge is developing environmentally sustainable photonic structures while maintaining excellent structural and optical performance. For instance, wearable optical biodevices in human-machine interfaces and implantable medical devices require materials that possess good mechanical flexibility and stretchability combined with biocompatibility and biodegradability to match skin and tissue properties.[5,6,7] Naturally derived polymers that are produced by living organisms demonstrate extraordinary mechanical flexibility and diverse rich surface chemistry, combined with excellent physical properties such as high decomposition temperature, low-thermal expansion, good transparency and biocompatibility.[8,9,10] Such features make them promising building blocks of flexible bioenabled hierarchical photonic structures.[11,12,13,14,15,16,17,18] Although inorganic materials have been used as the mainstream optical material platform for decades, their inherent mechanical rigidity, fragility, high absorbance, and potential toxicity make it difficult to meet the requirements of emerging applications in various advanced biomaterial-related fields.[19]

Research in the field of bio-enabled photonic structures has rapidly grown in the last two decades with much accelerated growth observed in the past d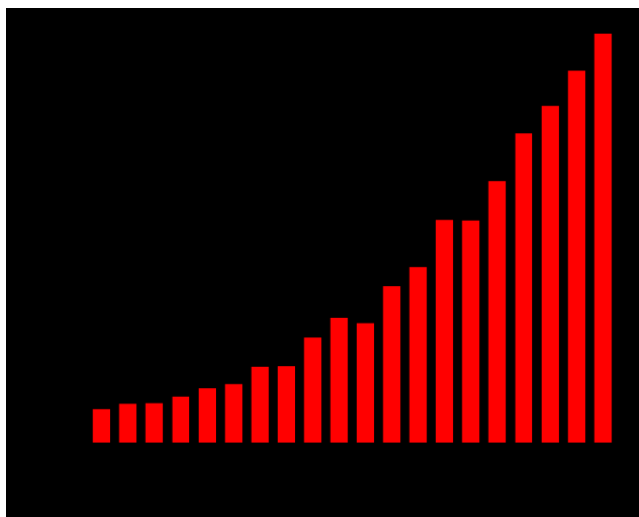ecade (Figure 1). Current original literature provides a large number of examples of biophotonic structures and integration of the spatially organized structures with a variety of biopolymers. These significant efforts can lead to the development of new functional biophotonic materials, extending the range of prospective optical applications, and require careful analysis to establish most interesting common trends and potentials for future impact.

Figure 1. Publications in naturally derived polymers for photonics, 2000-2019. (Web of Science, 2019).

Several recent reviews summarized the bio-related photonic and optical materials, with most of them focusing on the light-matter interactions of the biological optical materials and their applications.[1,2,4,20] However, very few reviews have discussed the combination of the critical

topics in naturally-derived biopolymers, synthetic materials, and resulting unique photonic and optical behavior in one collection. Although some reviews also considered photonics of biopolymers,[21] these topics mostly involved light absorption, fluorescence emission, and chemical reactions of biopolymers.

Due to these advantages of naturally-derived polymers for photonic/optics (e.g. mechanical robustness, transparency, renewability, rich chemistry and biocompatibility), it is extremely important to specifically discus the chemistry, nanostructure and properties of biopolymers, and summarize/analyze the fabrication strategies and mechanisms for constructing biopolymer-based photonics in a very general sense. Usually, a brief discussion of the fabrication and application of biopolymeric optical materials is present, without a detailed consideration of related biopolymer properties, principles of fabrication of hierarchical photonic structures, and underlying physical properties and chemical interactions. Thus, in this review, we discuss the naturally derived polymers serving as components for organized photonic materials, including photonic structures, materials selections, assembly strategies, and emerging applications (Figure 2).[14,15,16,17]
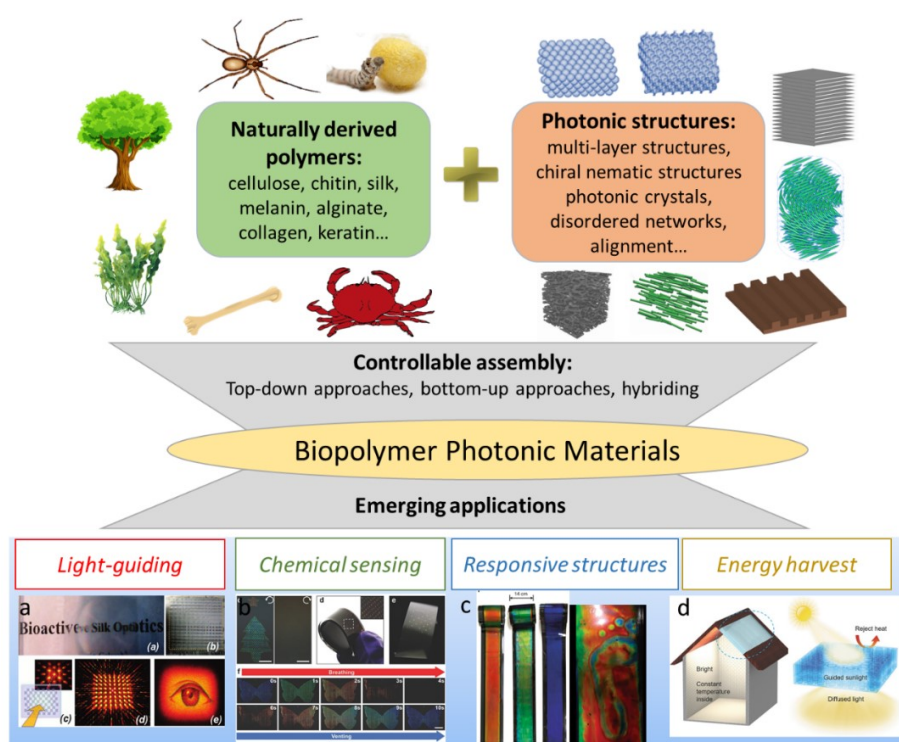

Figure 2. Overview of naturally derived photonic materials, including biopolymers selection, photonic structures, construction strategies, and emerging applications. (a) Silk optical elements[14]. Reprinted from ref. 14 with permission from American Chemical Society, copyright 2008. (b) Cellulose photonic sensors[15]. Reprinted from ref. 15 with permission from Wiley, copyright 2018. (c) Responsive cellulose nanocrystals photonics[18] Reprinted from ref. 18 with permission from Springer Nature, copyright 2018. (d) Transparent wood for light harvest[17]. Reprinted from ref. 17 with permission from Wiley, copyright 2016.

Below, we firstly briefly introduce the fundamentals of most frequently considered photonic structures, including multi-layered structures, opals, chiral structures, and photonic networks. Next, we summarize the corresponding fabrication approaches and relevant physical and chemical properties of biopolymers and the advantages of biopolymers as building blocks for photonic structures. Finally, we discuss current and emerging biophotonics applications with few existing examples, as well as related grand challenges.

2. Photonic and Biophotonic structures

Well-organized hierarchical micro/nanostructures are critical for realizing highly resilient photonic materials, structures, and systems.[22] Photonic structures enable the controllable light-matter interactions because of the hierarchically organized periodic structures at multi-length scales.[2,23,24,25,26,27] This section provides a brief overview of relevant structures and discusses their optical properties.

2.1 Multi-layered photonic structures

Structural colors are frequently produced by layered structures known as Bragg stacks and are caused by multilayer light interference with incident angle dependency. [1,27,28] The condition of incident wavelength, λ, for producing constructive light interference is described with the well-known relationship (Figure 3a):

$$2n_b d\cos\theta_b = m\lambda \qquad (1)$$

where θ_b is refraction angle, n_b is the refractive index, d is the film thickness, and m is an integer. Multilayer interference can be analyzed with periodical stacks of pairs of thin layers (Figure 3b).[27] In a special case of two layers, the A and B layers possess thickness of d_a and d_b, and refractive index n_a and n_b, respectively. Considering $n_b > n_a$, the phase of reflected light at each A-B interface changes by 180°, while remaining unchanged at the B-A interface. This is caused by the phase shift of half wavelength is caused by reflection at the surface with a higher refractive index, while no phase shift occurs at reflection at the surface with a lower refractive index.
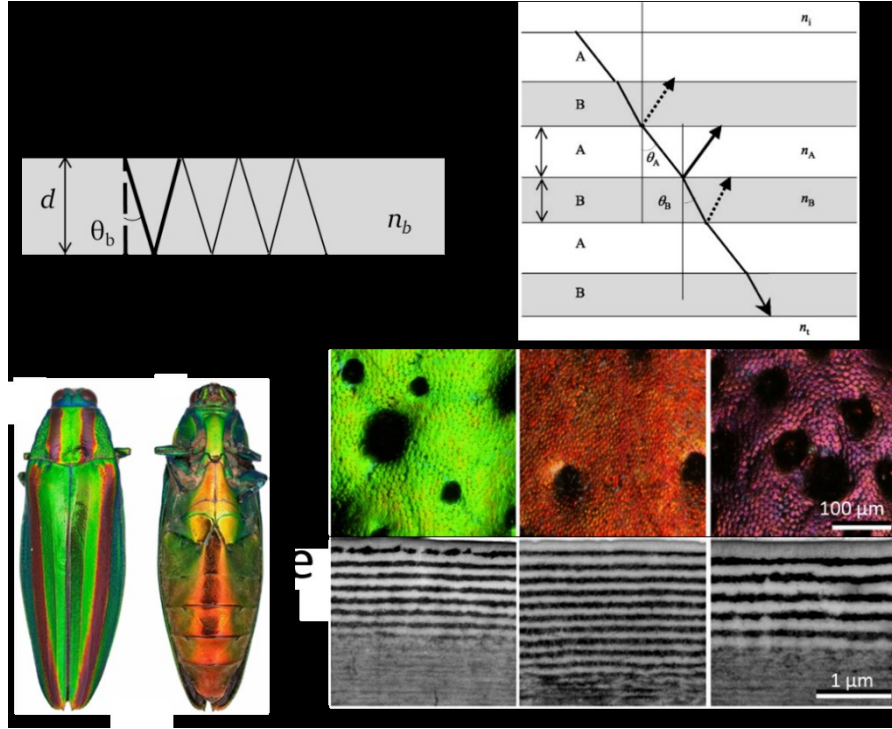
Figure 3. Configuration of common thin-film interference (a) and multilayer interference (b).[27] Reprinted from ref. 27 with permission from Elsevier, copyright 2005. (c) Photos of Japanese jewel beetle, *Chrysochroa fulgidissima*. Microscopy (d) and TEM (e) images of the cuticular surface of the beetles at different locations.[29] Reprinted from ref. 29 with permission from IOP Publishing, copyright 2013.

The general conditions for multilayer constructive interference are presented as [27]:

$$2(n_a d_a \cos\theta_a + n_b d_b \cos\theta_b) = m\lambda \qquad (2)$$

with maximum reflection achieved at:

$$2n_a d_a \cos\theta_a = (m-1/2)\lambda \qquad (3)$$

where the angles of refraction in layers A and B are designated as θ_a and θ_b, respectively (Figure 3).

If light waves interfere constructively, it results in strong structural color; whereas, destructive interference leads to faded colors.[30] Notably, the reflectivity highly depends on the difference of the refractive index between the two layers.[27] With close refractive index that is common in biopolymers multilayers, the number of layers should be significantly increased for achieving sharp light reflection. In contrast, the multilayer structures comprised of materials with large differences in refraction index ($\Delta n > 0.2$), maximum reflectivity intensity can be reached with stacks composed of only several layers. The multilayer interference for thicker films demonstrates

advantages in selectivity, which is more favorable for obtaining highly intense and uniform structural color.

This multilayer interference is exploited by numerous natural creatures, such as *Morpho* butterfly, jewel beetles, birds-of-paradise, mollusks, and fish for survival in natural competition (Figure 3). [31,32,33,34,35] For instance, the metallic structural color of Japanese jewel beetles, *Chrysochroa fulgidissima,* is a well-known example of multilayer interferences.[29,36] As demonstrated in Figure 3c,[29] the elytra favorably reflect the green wavelength that is interrupted with longitudinal, dark-purple stripes, while the ventral area reflects an orange color. These intense structural colors are caused by the multilayer-controlled light interference, which in turn stems from the alternating morphology that consists of bilayers (a chitin layer and a melanin layer) with different periodicities from ~100 nm to 200 nm (Figure 3d, e). These structural colors are highly view angle dependent, as expected for the common multilayer interference.[34] Theoretical calculation indicated that the ideal thickness is around 150 nm for maximum reflection, for alternatively stacking five layers with refractive index varying from 1.5 and 1.6 for each layer.

2.2 Photonic crystal properties

Photonic crystals are organized optical structures with periodic modulation of the refractive index at the sub-micron scale, which enables the controlled light propagation.[37] These highly organized structures demonstrate intense structural colors if the photonic gap is within the visible wavelength range. Photonic crystals can be classified into three categories, one-dimensional (1D), two-dimensional (2D) and three-dimensional (3D) structures as discussed in this section (Figure 4a).[38,39]

In 1D photonic crystals, layers of different refractive materials are deposited in alternating way to form the periodical modulation of refractive index in one direction. For example, the brick-and-mortar structure of mollusks shells is built from inorganic plates and a protein layer, which provides excellent mechanical performance.[40] In addition, the highly ordered multilayer structures with different refractive index enable intense iridescent colors of these shells. For some shells of the mollusks, such as *Haliotis Glabra*, both interference and diffraction are responsible for the vivid structural colors, owing to the fine-scale grating structure and stacks of thin crystalline nacreous platelets under the surface.[41]
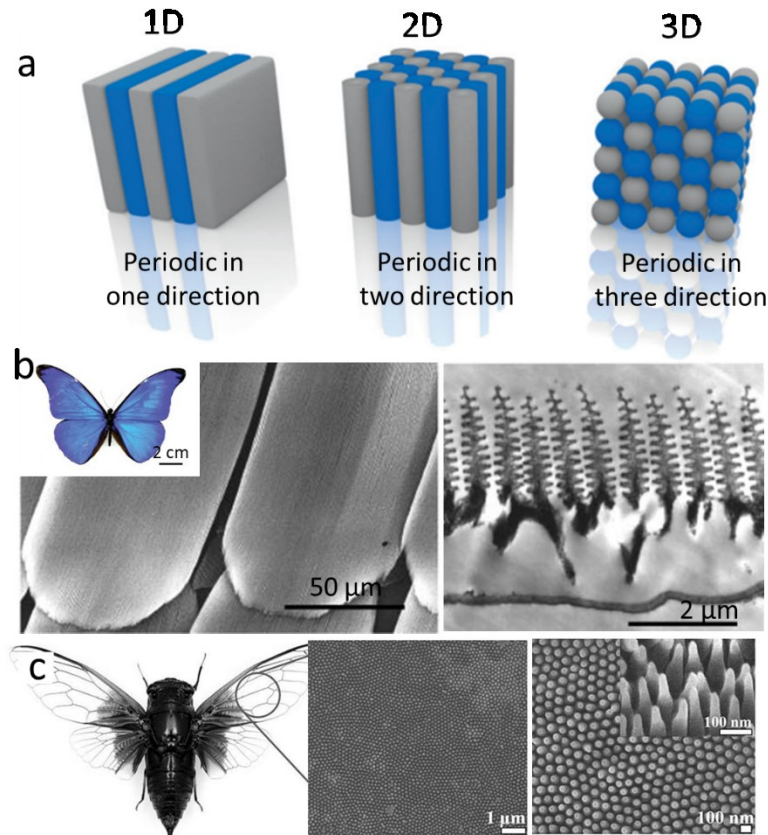
Figure 4. (a) General organization of 1D, 2D and 3D photonic crystals[38], Reprinted from ref. 38 with permission from Wiley, copyright 2014. (b) 1D photonic crystal structure of iridescent scale of butterfly (*M. rhetenor*),[42] Reprinted from ref. 42 with permission from CC-BY license. (c) 2D photonic crystal structure of the wings of a black cicada (*Cryptotympana atrata Fabricius*).[43] Reprinted from ref. 43 with permission from AIP Publishing, copyright 2016.

In addition, some 1D photonic crystals can be considered as parallel alternating layers and layers filled with air, which is very common in synthetic and natural materials such as some species of butterfly wings. These materials display iridescent colors that are attributed to the diffraction effect caused by evenly grooved surface microstructures. As shown in Figure 4b, *Morpho* wing-scales' structures reveal the discretized ridges (~200 nm in width, ~2 µm in height) comprising periodic lamellae of alternating cuticle layers with the thickness of tens of nanometers. Every single ridge exhibits a characteristic tapered shape with an asymmetry of lamella.[42] These two elements can interact with light independently to obtain structural colors resulted of quasi-multilayer interference and thin-film interference, respectively. The synergistic effect produces light reflection at the same wavelength that allows *Morpho* wing to show a brilliant blue color.[27]

2D photonic crystals possess the structural periodicity in two directions (Figure 4a).[38] Common examples of the 2D photonic crystals are periodic arrays of nanorods and periodically arranged pores.[38] Notably, the 2D periodic ordering of nanorods at the surface can minimize the reflection

from surface and significantly enhance the optical transparency. In nature, the most well-known examples are the transparent cicada wing and the moth eye.[43,44] As shown in Figure 4c, the surface of the transparent cicada wing, which mainly consists of chitin, presents highly ordered hexagonal array of nano-nipples with center-to-center top spacing of 160 nm.[43] The average size of nano-nipples, with a height of 200 nm, continuously decreases from 140 nm of basal diameter to 60 nm at the top. The enhanced antireflection performance of such structures is attributed to a refractive index gradient between those of air and the chitin, which enable largely decreasing light reflectance over a broad wavelength range.

Similar to the structure of a cicada wing, the outer surface of the facet lenses in the moth eye consists of an array of excessive cuticle corneal nipples with distance of 180-240 nm and height varying from 0 nm to 230 nm.[44] Similarly, the nipples create a gradient refractive index because their size and distance are distinctly smaller than the wavelength of visible light. The gradient refractive index highly depends on the shapes, spacing, and height, based on experimental and theoretical studies.[44] Nipples with a paraboloid shape demonstrated ideal, complete antireflection properties across the visible spectrum, which can minimize the eye glare to make them less visible for predators.

The optical properties of 3D photonic crystals are determined by the periodicity and contrast of refractive index variation in all three directions (Figure 4a).[45] The critical factor that affects the optical properties is the photonic band gap that refers to the energy/wavelength range of prohibited light propagation in photonic crystals. Light in this band gap will be completely reflected.[45] To describe the geometry of photonic crystals, the terms of "lattice" is frequently used.[37] Local defects are sometimes intended to embed into photonic crystals to introduce localized photonic gaps. Such designs can induce the incoherent scattering and hopping-like photon transport for an efficient waveguide.[38,45,46,47]

The most famous 3D photonic crystals are natural opals, which demonstrate rich colorful appearances because of periodic systems with densely packed spheres (Figure 5a).[48,49] These spheres are near monodisperse with diameters within 150-400 nm, forming a face-centered cubic (FCC) lattice (Figure 5b-c).[48] Additionally, they are usually amorphous and can be doped with other elements (e.g. Fe, Al, and Ti) to control their refractive index.[50,51] The voids can be filled with hydrated silica for enhance mechanical stability and lower the refractive index contrast.[48,52] As a result, the light scattering can be significantly minimized, making these structural colors much clearer.
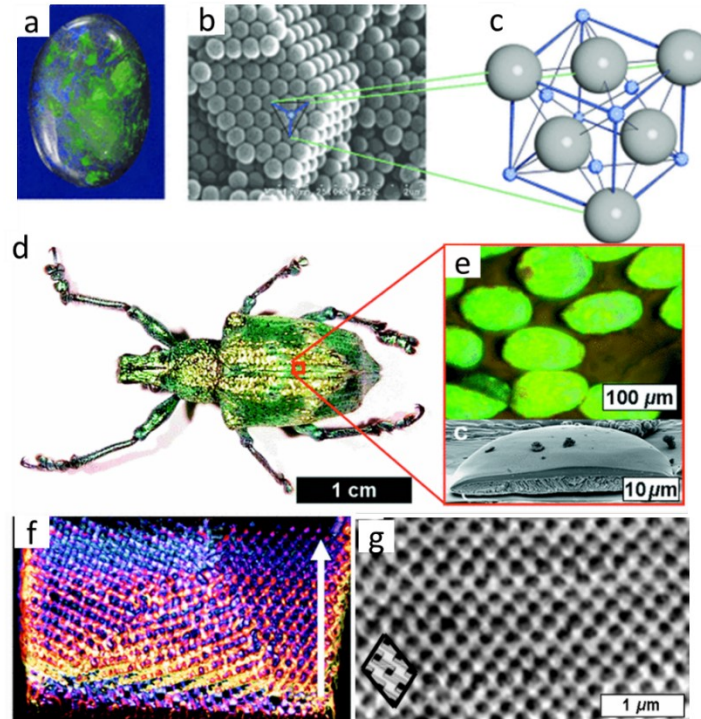
Figure 5. (a-c) Photonic structure of natural opal: (a), (b) SEM image and (c) scheme of the opal structure.[48] Reprinted from ref. 48 with permission from Wiley, copyright 2009. (d-g) 3D photonic crystal structure in beetle scales: (d) photograph of *L.augustus*. (e) Optical micrograph and SEM image of individual scales, (f) 3D reconstruction image; (g) SEM image of the photonic structure.[54] Reprinted from ref. 54 with permission from American Physical Society, copyright 2008.

Natural 3D photonic structures are also found in many living creatures.[53] Take exoskeleton scales of the weevil *Lamprocyphus augustus* as an example (Figure 5d).[54] Their brilliant green iridescence is associated with an interior diamond lattice-like cuticular structure as shown in Figure 5d-g.[54] In sharp contrast to the angle dependent iridescence in multilayer structure and opals, this scale shows near angle-independent structural color because the combination of differently oriented, single-crystalline micrometer-sized domains of the same 3D crystal lattice in each scale. Notably, this 3D photonic crystal cannot possess complete photonic bandgap because of the low refractive index of biopolymeric materials. However, photonic crystals with complete photonic bandgap can be constructed by using the natural photonic crystal as biotemplates for porous opal structures with high refractive index contrast.[55]

Calculating the complex photonic bandgaps is important to gain fundamental understanding of the observed appearance of both natural and synthetic photonic structures and to effectively guide the design and fabrication of synthetic photonic structures made from natural and synthetic materials. It plays an important role in guiding the design of three-dimensional photonic bandgap

materials, the fabrication of which remains resource-intensive. Photonic band gaps can be determined by plotting the appropriate photonic band diagrams.

To numerically calculate such diagram, software packages such as MIT Photonic Bands (MPB)[56] and BandSOLVE[57], can be employed for this purpose. MPB is a software package to compute definite-frequency eigenstates of Maxwell's equations in periodic dielectric structures. It can compute optical dispersion relations and eigenstates for structures such as strip waveguides and optical fibers. In MPB, calculations are typically performed using 32×32×32 grid points to discretize the unit cell. MPB computes fully-vectorial eigenmodes of Maxwell's equations with periodic boundary conditions by preconditioned conjugate-gradient minimization of the block Rayleigh quotient in a plane-wave basis. The BandSOLVE software employs the Plane Wave Expansion (PWE) algorithm to perform band computations, and it also provides a graphical display of the electromagnetic fields and other quantities of interest for further analysis. It also includes several advanced simulation features for more efficient, fast band computations, such as inversion symmetry, mode seeding, and parity for 3D calculations. These computational tools are widely available to researchers interested in designing novel photonic structures.

2.3 Chiral nanostructures

The chiral nematic structures, also called twisted plywood and helicoidal Bouligand structures, are well known arrangements which are identical to those for cholesteric liquid crystals (LC) as shown in Figure 6a.[58,59] This hierarchical architecture consists of superimposing planar layers of parallel-aligned rod-like molecules/nanostructures with a certain twisting angle. A 360° rotation of the planar layer defines the helicoidal pitch (P) (Figure 6a). This chiral morphology reflects circular polarized light of the same handedness as the helicoid structure and transmits circular polarized light with the opposite handedness.[60] The selective reflection of circular polarized light follows the rule of Bragg's law, $\lambda_{max} = n_{av} P \sin\theta$, where n_{av} is the average refractive index of the helicoidal structure and θ is the angle of incidence. The reflectivity for a given color is produced with the half-pitch distance corresponds to the wavelength of the color.[60]

Examples of chiral nanostructures are reported in fruits, beetles, and exoskeletons of crustaceans.[58,61,62] These chiral nanostructures can produce vivid structural color as a result of matching the pitch distance with visible light wavelength. Additionally, these structures exhibit both high toughness and strength because of various toughening mechanisms at multiscale levels, which are mutually exclusive in most artificial materials.[63] Most of these natural chiral architectures only selectively reflect left circularly polarized light because of their left-hand chiral organization. Figure 6b-d shows the metallic green beetle *Chrysina gloriosa*, which selectively

reflects left circular polarized light when illuminated with unpolarized light.[58] However, this brilliant metallic color disappears when viewed under a right circular polarizer. The exoskeleton of this beetle consists of hexagonal domains (~10 µm) that appear to be green with a bright yellow core. These domains are composed of chiral nematic nanostructures that are organized in a near-hexagonal domain, which can produce left-hand reflectance. Interestingly, the beetles not only demonstrate the chirality and selective optical reflections in visible range, but they also show chirality and chiroptical activity in THz range, for unknown purposes. [64]
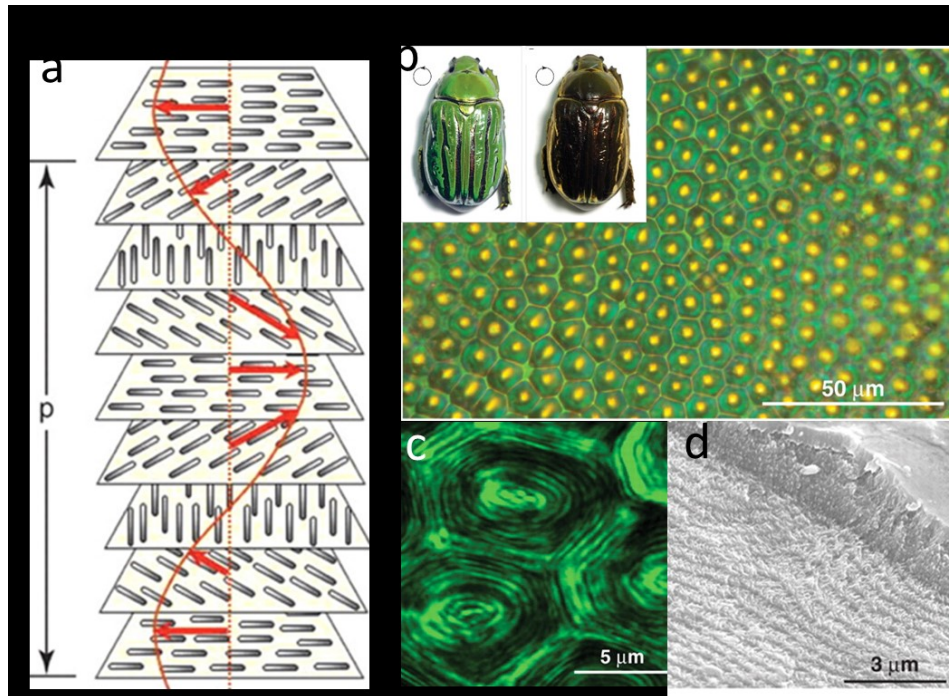

Figure 6. (a) Chiral nanostructure.[58] (b-c) Chiral nematic nanostructure of the beetle *C. gloriosa* that is responsible for the circularly polarized iridescence.[58] Reprinted from ref. 58 with permission from American Association for the Advancement of Science, copyright 2009.

Notably, few remarkable biological structures that are found in beetles and fruits can reflect both left and right circular polarized light. For example, the scarabaeid beetle *Plusiotis resplendens* shows intense green and gold coloration under left and right circular polarizer, respectively.[62] The optically active reflecting layer in the outer exocuticle is composed of a sandwiched structure, which consists of thick upper and lower layer for a total sandwiched layer of 1.81 µm.[65] The upper and lower layers exhibit left twisted chiral nematic structures, while the middle layer exhibits vertically oriented architecture. The left-handed upper layer reflects the left-hand circular polarized light, while allowing the right-hand polarized light to go through. The middle unidirectional layer then acts as a half-wave retardation plate to convert the right-handed circularly polarized light that

was transmitted by the upper layer into left-handed light. Then, the bottom layer reflects the converted left-handed light back, and the light changes into right-hand light again through the middle layer. Finally, the right-hand light can propagate through the upper layer to exhibit right-hand polarized light reflection.   Another example is the *Pollia condensata* fruit in the plant kingdom.[61]   The metallic blue iridescence originates from the thick-walled cell, which bears uniform helicoidal structures. Furthermore, this fruit can reflect both left-hand and right-hand circular polarized light. This unique optical property is associated with the chirality of the organized microfibrils with both left- and right-handedness.

2.4. Semi-organized photonic networks

In contrast to highly-ordered periodic structures, which are capable of producing intense structural color iridescence through light interference, disordered photonic networks can generate bright white color through broadband light scattering.[66,67,68,69] Multiple random scattering of incident light allows materials to exhibit bright whiteness at a small thickness. With the lower refractive index of the scattering elements, the thicker the system must be to achieve a pronounced brightness.[70]
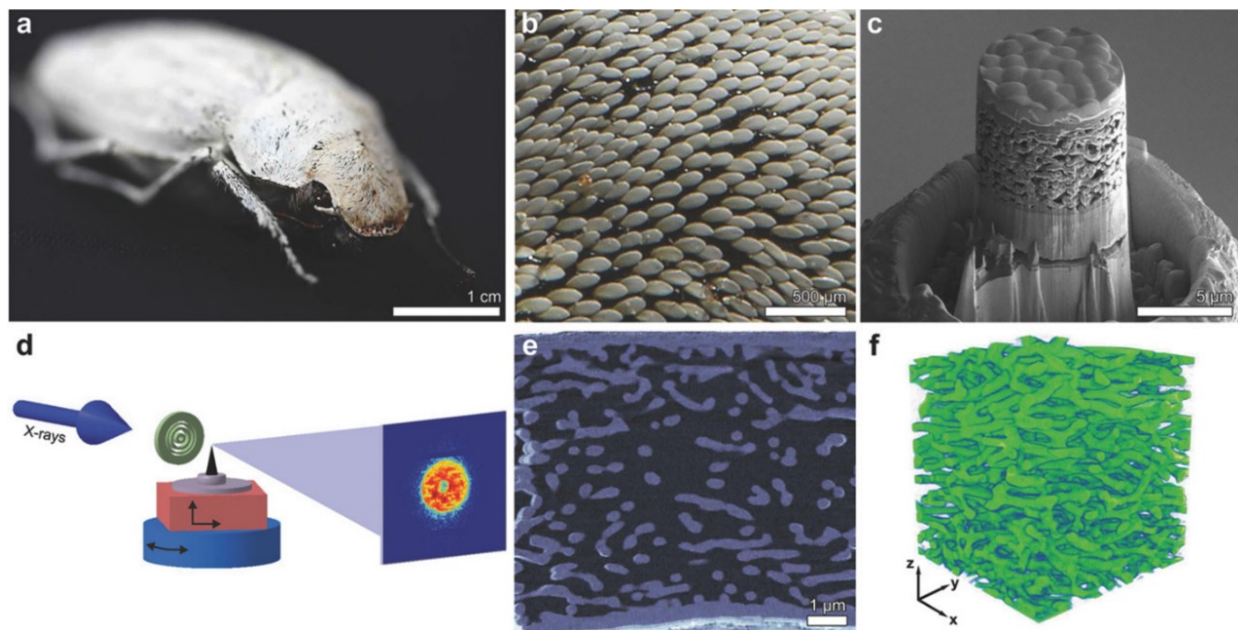

Figure 7. The photo of a brilliant white beetle *Cyphochilus* (a) and the beetle scales (b). (c) SEM of the sample pillar on a pin holder obtained from a beetle scale by focused ion-beam milling. (d-f) 3D reconstruction image of the photonic random networks by X-ray tomography technique.[72] Reprinted from ref. 72 with permission from Wiley, copyright 2018.

Among natural materials, the spongy random networks of keratin found in the barb of bird feathers are known for producing diffuse scattering.[27]   The beneath layer of scales of a butterfly with irregular network structure can produce diffused light through light scattering, which can be

selectively reinforced through the interference of the attached periodical structures.[71] Another striking example is a white beetle, e.g., *Cyphochilus*, which displays brilliant whiteness (Figure 7).[72] The body of the beetle is covered by 7 μm-thick white scales with anisotropic nanostructured network. This network is composed of interconnected chitin fibrils with length less than 1 μm and with a diameter of 250 nm. These anisotropic nanostructures can increase the light scattering in the out-of-plane directions, leading to the enhanced brightness, while minimizing the in-plane scattering that does not contribute the brightness. This unique character makes this network one of the strongest scattering low-refractive-index materials in nature. These kinds of morphologies have been reproduced a number of times with abiotic materials such as plasmonic nanoparticle structures as perfect absorbers and reflectors.[73,74,75]

Overall, these well-ordered hierarchical photonic structures provide extraordinarily examples of unique and often exceptional photonic properties, including vivid structural color, brilliant whiteness anti-reflection, and polarized light. Various efficient manipulations of light are responsible for these attractive optical phenomena through light absorption, multilayer interference, scattering, diffraction, as well as combinations of these effects. Even for the same photonic properties, the light propagation mechanism can be very different. Learning and applying these design and assembly principles are considered for constructing high-performance biophotonic materials. Additionally, these observations clearly point out that naturally derived materials can be a great choice to sophisticated engineering these optical effects in the synthetic materials and structures.

3. Natural polymers for photonic structures

Naturally derived polymers are ubiquitous and produced by plants, animals, and micro-organisms as the main components in of their bodies. In nature, they are constructed into various forms of well-organized photonic structures as summarized in Table 1. These structures demonstrate good mechanical properties, light-weight, renewability, and prospective low-cost combined with prospective biocompatibility and biodegradability. Additionally, other additive properties of biopolymers, such as strong adhesion, good responsive properties, self-healing, and tailored wetting, which may provide additional functionalities. It is worth to note that polynucleotides such as DNAs are too pricy to be used as meaningful structural photonics materials, and most relevant photonic examples in literature are template assembly of plasmonic nanoparticles using

DNAs.[76,77,78,79] Thus, we will not discuss polynucleotides in this review and refer a reader to several reviews suggested above.

In this section, we discuss the chemistry, morphology, properties, and preparation of naturally derived polymers that are frequently used for constructing biophotonic materials from classes of polysaccharides and proteins (Table 1).

Table 1. Biopolymers in natural photonic structures.

Biopolymers	Photonic structure	Natural source	Optical mechanisms
cellulose	chiral nematic structures, gratings	fruits, flowers	chiral photonic crystals diffraction gratings
chitin	chiral nematic structures, multilayered structure, disordered networks	insect cuticles/wings, mollusk shells	chiral photonic crystals, multilayer interference, light scattering, diffraction gratings
keratin	multilayer structure, photonic crystals	avian feathers	multilayer interference
collagen	photonic crystals	avian skin	multilayer interference
melanin	multilayered structure	avian feathers/skin	pigments, multilayer interference

3.1 Cellulose and nanocellulose materials

Cellulose is the most abundant class of biopolymer materials available in nature.[80] Their linear backbones are composed of several hundreds - thousands of β 1,4-linked D-glucose units (Figure 8a). Cellulose is mainly produced by plants and bacteria in the form of cellulose fibers, microfibers, and finally, nanofibers (CNFs), which constitute the cell walls (Figure 8).[81,82] These CNFs possess one-dimensional (1D) anisotropic nanostructure with alternatively packed crystalline regions and small portions of amorphous regions. The predominant crystalline regions, usually called cellulose nanocrystals (CNCs), are composed of parallel linear cellulose chains bound by hydrogen bonding and van der Waals forces.[81]

Such features endow CNFs and CNCs with extraordinary mechanical strength, stiffness, and flexibility, in addition to excellent thermal, optical, and biological properties. These properties are attractive for practical uses in a variety of engineering and biomedical fields. Nanocelluloses demonstrate amphiphilic character because of the different surface chemistries at different crystal planes. The OH groups decorate hydrophilic planes, while CH groups constitute hydrophobic plane.[83] This unique amphiphilic nature facilitates the heterogeneous interaction with other amphiphilic nanocomponents used in assembling hierarchical nanostructures.[84] In many cases, nanocelluloses that are produced by bacteria are classified the third categories (bacterial cellulose), although they possess similar morphology with CNFs.[81] CNCs and CNFs are distinguished by their length and aspect ratio, as well as their crystal structures (Table 2). The dimensions of nanocellulose highly depend on the original cellulosic source and the processing conditions. The primary goal of nanocellulose processing is to have highly efficient exfoliation of these naturally-occurring cellulose nanostructures without destroying their inherent structure. To date, numerous techniques have been developed to isolate CNFs, including high pressure homogenizer,[85] grinder,[86] high-intensity ultrasonicator,[87] and ball mill.[88] The shearing force produced in these intense mechanical treatments is capable of disintegrating cellulose fibers into nanofibers.

Table 2. The classification of cellulose materials.

Types of cellulose	Sub-types	Cellulosic source	Synthesis	Crystal types
	Cellulose nanofibers (CNFs)	wood, bamboo, hemp, flax	Mechanical treatments with/without chemical or enzymatic pretreatments	cellulose I
Nanocellulose	Cellulose nanocrystals (CNCs)	wood, cotton, hemp, flax, wheat straw, tunicate, bacterial cellulose, microcrystalline cellulose	Acid hydrolysis	cellulose I
	Bacterial cellulose (BC)	sugars and alcohols	Bacterial biosynthesis	cellulose I
Regenerated cellulose	_____	Cotton, wood, bamboo, microcrystalline cellulose	Dissolution-regeneration	cellulose II

The resulting CNFs exhibit high aspect ratios (50-100) because they largely preserve the original dimensions of the cellulose nanostructures. However, the strong interfacial strength between neighboring CNFs in cellulose fibers, especially dried cellulose that forms strong hydrogen bonding, make these techniques very low-efficient and energy-intensive. Additionally, the as-

prepared CNFs exhibit large variation in diameter and length of individual nanofibers and entangled network structures are poorly dispersed in water, which largely restricts their aqueous-based processability.   Even if using the same cellulosic source, different preparation and modification methods can lead to nanocellulose structures with different dimensions and surface chemistries (Figure 8).[82]
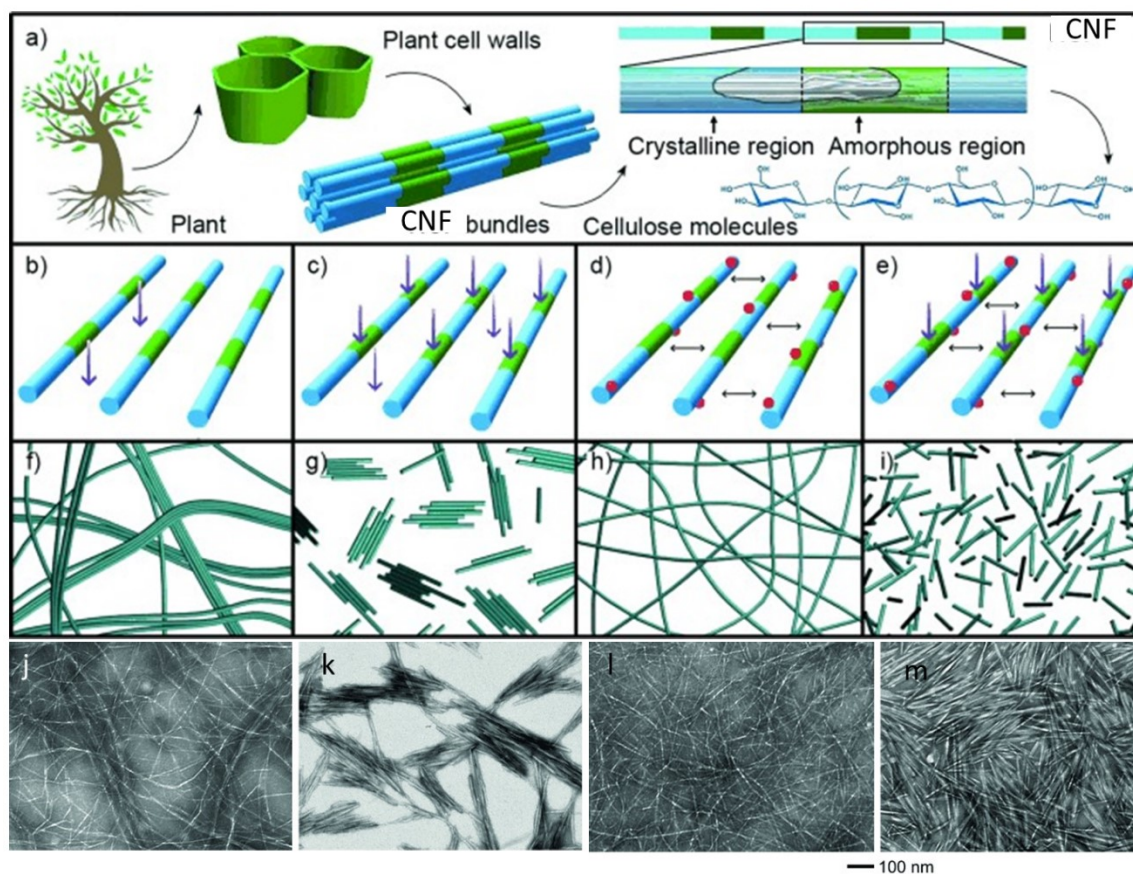

Figure 8. Nanocellulose materials prepared from wood pulp through different methods and the hierarchical structure of wood cell wall (a); (b, f and j) CNFs prepared by high-intensity ultrasonication; (c,g and h) CNCs prepared by HCl hydrolysis; (d, h and l) CNFs prepared by TEMPO pretreatment and ultrasonication; (e, i and m) CNCs prepared by H_2SO_4 hydrolysis.[82] Reprinted from ref. 82 with permission from Wiley, copyright 2014.

To minimize the energy consumption, various chemical treatments or enzymatic hydrolysis were introduced to decrease the interfacial strength of CNCs. The most known example is the TEMPO (2,2,6,6-tetramethylpiperidine-1-oxyl radical)-mediated oxidation method.[89,90,91] In this chemical process, carboxylate groups are grafted on the cellulose molecules. The strong repulsion generated from the negatively charged carboxylate groups allows fast-preparation of CNF dispersions with gentle mechanical disintegration treatment.[89] The as-prepared individual CNFs

from wood pulp exhibit diameters of 3-4 nm and lengths up to a few microns, which are believed to be the elementary nanofibers dimensions in wood cells. Bacterial cellulose is another high aspect ratio nanocellulose structures that presents in a web-like entangled microstructure.[92] Individual bacterial cellulose possess ribbon-like morphology with 30-100 nm in width and around 100 μm length, which consists of elementary nanofibers of 2-4 nm in diameter (Figure 8).[93]

Another class of nanocellulose materials, CNCs, can be synthesized by acid hydrolysis of a wide variety of cellulosic sources, including plants, microcrystalline cellulose, bacterial cellulose and algae.[94,95] Disordered amorphous regions are more vulnerable to hydrolysis than crystalline region of CNFs. Thus, crystalline segments are liberated when the amorphous regions are etched. As a result, the obtained CNCs are short and possess very high crystallinity of 80-90%.[96] The length of individual CNCs usually ranges from 100-300 nm depending on the source, with the CNCs from tunicate reaching microns.

Use of sulfuric acid for hydrolysis allows the grafting of highly negatively-charged sulfate esters, high negative surface potentials (around -50 mV) and the obtaining of stable CNC aqueous dispersions.[97] Hydrochloric acid used for producing CNCs cannot react with the surface hydroxyl groups of cellulose, resulting in poor CNC dispersion.[98] However, this issue can be addressed by using CNFs that are prepared from the TEMPO oxidation method as the original cellulosic source because CNCs can inherit the anion carboxylate groups.[99]

In addition to native nanocelluloses, regenerated celluloses is prepared directly from cellulose materials *via* the dissolution and regeneration process.[100,101] However, the long length of the cellulose molecular chains, their close packing and strong bonding frequently make cellulose materials insoluble in conventional solvents.[102] In the traditional dissolution process, cellulose is converted to cellulose xanthogenate with the help of CS_2, which can dissolve in aqueous NaOH to form a viscous solution, subsequently treated with acidic solution to produce regenerated cellulose. However, the use of toxic, flammable, explosive CS_2 is undesirable.[100] Several approaches with "green" solvents, including N-methylmorpholine-N-oxide (NMMO),[103] ionic liquids,[104] LiCl/N,N-dimethylacetamide,[105] and alkali/urea,[106] have also been suggested for the preparation of regenerated celluloses and forming hydrogels.

As known, crystalline celluloses with usually degree of crystallinity within 70-80%, exhibit four different crystalline types, cellulose I, II, III, and IV, with different symmetries of crystal packings.[107] The crystal structures in native nanocellulose are defined as cellulose I structure. It has two polymorphs: a triclinic structure (Iα) and a monoclinic structure (Iβ). The two polymorphs usually co-exist in nanocelluloses, but with various ratios that highly depend on the cellulosic sources.[108]

For example, Iβ dominate plants and tunicate, while Iα presents more frequently in algae and bacteria.[109,110,111]   Cellulose I is the crystal structure with the highest axial elastic modulus (it reaches 220 GPa).[112]   Cellulose I_α and has a triclinic one-chain unit cell where parallel cellulose chains stack, via van der Waals interactions.   Cellulose I_β has a monoclinc two-chain unit cell, where cellulose chains stack parallel. Cellulose II is the most stable structure, which can be found in regenerated cellulose from the treatment of cellulose I by alkali solution, mercerization, or recrystallization from a solution.[113]   It consists of a monoclinic two-chain unit cell as cellulose I_α but the cellulose chains with opposite polarity are stacked.[114] And, the crystallinity of regenerated cellulose is much lower than that of native nanocellulose, resulting in poor mechanical performance.

Both cellulose forms III and IV could not be found in natural cellulose materials. Cellulose III can be obtained by treating cellulose I and II with liquid ammonia or selected anhydrous alkylamines.[115] Compared to cellulose I_α and I_β, the intramolecular hydrogen bonding between O6 and O2 are broken in cellulose III, resulting in the glucose ring transferred from *tg* conformation of original cellulose glucose ring to a *gt* conformation.[116]   And the cellulose III can be reversibly transformed back to cellulose III by hydrothermal treatment.   On the other hand, cellulose IV generally cannot be prepared directly from cellulose I ascribing to the high crystalline order, only from the lower crystalized cellulose II and III by heat treatment in solvents such as glycerol at 260°C.[117]

3.2 Chitin materials

Chitin is the second most abundant natural polymer, which mainly exists in the exoskeleton shells of arthropods, such as crabs, shrimps, and beetles. Chitin is a structural biopolymer that has high molecular weight and a linear chain of a (1,4)- β-N-acetylglucosamine.[118] Naturally occurring chitin is in the form of ordered crystalline nanofibrils that are often embedded in protein matrix in the crustaceans (Figure 9a).[119,120]

Chitins exist in three different crystalline forms (α, β, and γ-chitin) that differ in the packing and polarities of adjacent chains in adjacent sheets.[9] The γ form was occasionally observed and was suggested as a variant of α form.[121]   Molecular chains in the α form are arranged in antiparallel manner with strong inter- and intra-molecular hydrogen bonding network, whereas the β form has a parallel chain packing resulting in ordered crystals with elastic modulus of 120 GPa.[122,123] This feature allows α-chitin strong inter-sheet hydrogen bonds that are absent in β-chitin, resulting in readily swelling of β-chitin. Compared with the β-chitin, α-chitin is more stable and the β-to-α

transition can be realized thorough recrystallization.[124] The α-chitin is the most common crystal form found in nature and is produced commercially from crab and shrimp shells.[125]
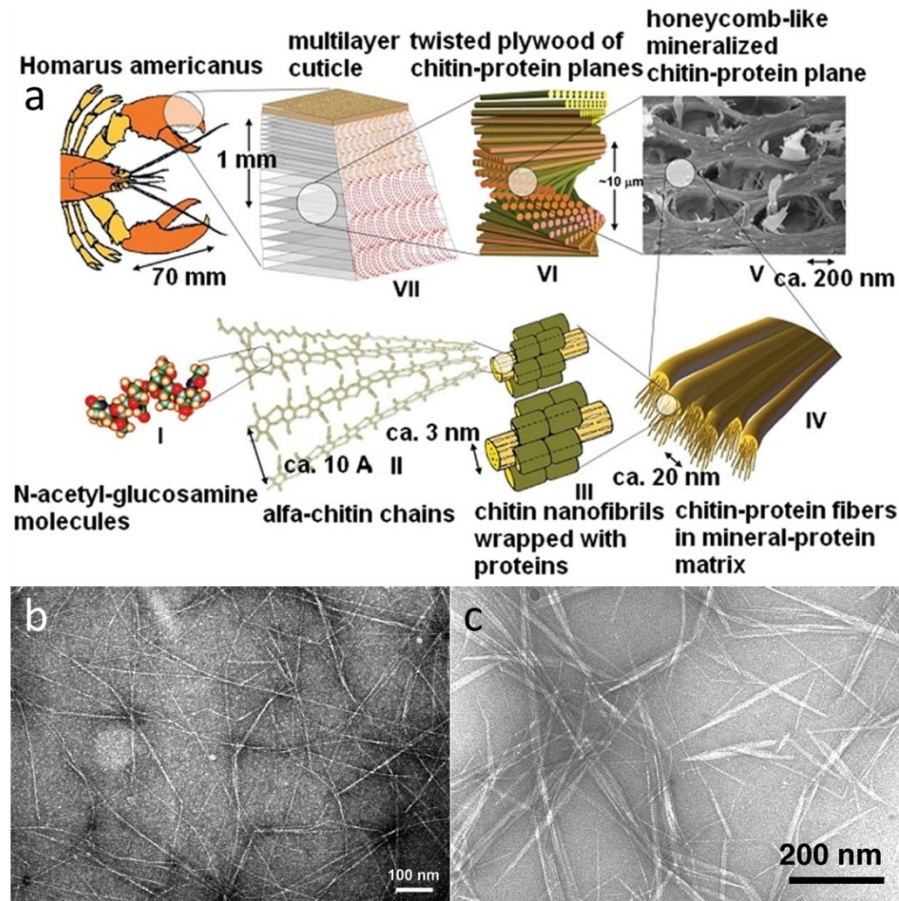

Figure 9. The schematic illustration of natural chitin nanofibers in lobster.[119] Reprinted from ref. 119 with permission from Elsevier, copyright 2005. (b) Chitin nanofibers prepared from squid pen by mechanical treatment under acid condition.[126] Reprinted from ref. 126 with permission from American Chemical Society, copyright 2008. (c) Chitin nanocrystals prepared by TEMPO-mediated oxidation of α-chitin.[127] Reprinted from ref. 127 with permission from American Chemical Society, copyright 2008.

Chitin nanofibers in natural organisms have diameters ranging from 2 to 25 nm depending upon species.[128] Natural chitin sources usually contain large amounts of other components, such as minerals, proteins, and pigments, thus chemical pretreatment has to be carried out to purify the chitin source. This pretreatment usually involves NaOH, HCl, ethanol, and NaClO to remove proteins, minerals, pigments, and bleach chitin, respectively.[125,129]

It is worth to note that chitin and cellulose biomaterials have similar chemical structures, both with linear polymer chains consisting of β 1,4-linked D-glucose units.[130 ,131] The only difference is the

functional group on C2: instead of hydroxyl group of cellulose, an acetamido side group is present in chitin backbones. Similar chemical structures enable comparable balance of inter/intra molecular interactions. For example, the –C(6)H2OH on both chitin and cellulose hydrogen bond with neighboring chain and the next unit along the same chain, which enable the *gt* and *tg* conformation, correspondingly.   However, the acetamido group on C2 introduces additional intrerchain H-bonding between C(2)NH···O=C(7') and C(6)H2OH···O=C(7').[132] The abundant H-bonding contributes to the higher ordered crystalline structure of chitin backbones. The crystal morphs further arranged with protein to form nanofibers with similar hierarchical structure as cellulose nanocrystals. The subsequent mechanical treatment can exfoliate the purified chitin material into chitin nanofibers. Therefore, methods employed in the preparation of nanocellulose materials are widely adopted to isolate the chitin nanofibers because of their similar surface chemistry and nanoscale structure.

In the whole process, the chitin should be kept in the wet state similarly to nanocellulose preparation processing. Otherwise, it is difficult to disintegrate chitin nanofibers because of the strong interfibrillar bonding caused by the drying process. TEMPO-mediated oxidation was also frequently introduced to selectively oxidize the primary hydroxyl groups of chitin into carboxylate groups.[127] Combining the following mechanical disintegration treatments (e.g. homogenizer, blender, ultrasonication, ball mill), individual chitin nanocrystals with diameter of 8 nm and length of 340 nm can be obtained (Figure 9c). Direct exfoliation of β-chitin of squid pen in an acidic aqueous solution is capable of producing uniform chitin nanofibers with 3-4 nm width and length up to several microns (Figure 9b).[126]

Additionally, chitin nanocrystals or whiskers can be prepared using acid hydrolysis.[133] Disordered regions of chitin are preferentially hydrolyzed in the acid solutions, whereas highly crystalline regions have a higher resistance to acid attack, resulting in chitin nanocrystals with high crystallinity.[10] The most important derivative of chitin is chitosan, which is obtained by partial deacetylation of chitin under alkaline conditions.[134,135] The positive charge makes them soluble in dilute acids such as acetic acid or formic acid.[136]

3.3 Silk Proteins

Silk is natural fibrous protein, and acts as the main structural component in insect cocoons and spider webs.[137] In the natural silks, the multidomain silk chains are assembled in nanofibrils composed of inter-connected domains of β-sheets with the diameter of 3-5 nm.[10]   These elementary silk nanofibrills can closely pack together to form silk microfibers with diameter of 20-200 nm, which will further assemble into macroscopic fibers glued by other adhesive proteins.[138]

For example, the *Bombyx mori* (*B. mori*) silkworm silk possess a core-shell fibrillary structures with a diameter of 10-25 μm, where two silk filaments are coated by glue-like sericins, which comprise 25–30% of silk cocoon mass (Figure 10a).[139] Similar to the hierarchical nanostructures in polysaccharide nanofibers, natural silk nanofibers also have stiff β-sheet nanocrystals embedded in semi-amorphous matrix consisting of helices. β-turns, and random backbones.[140]
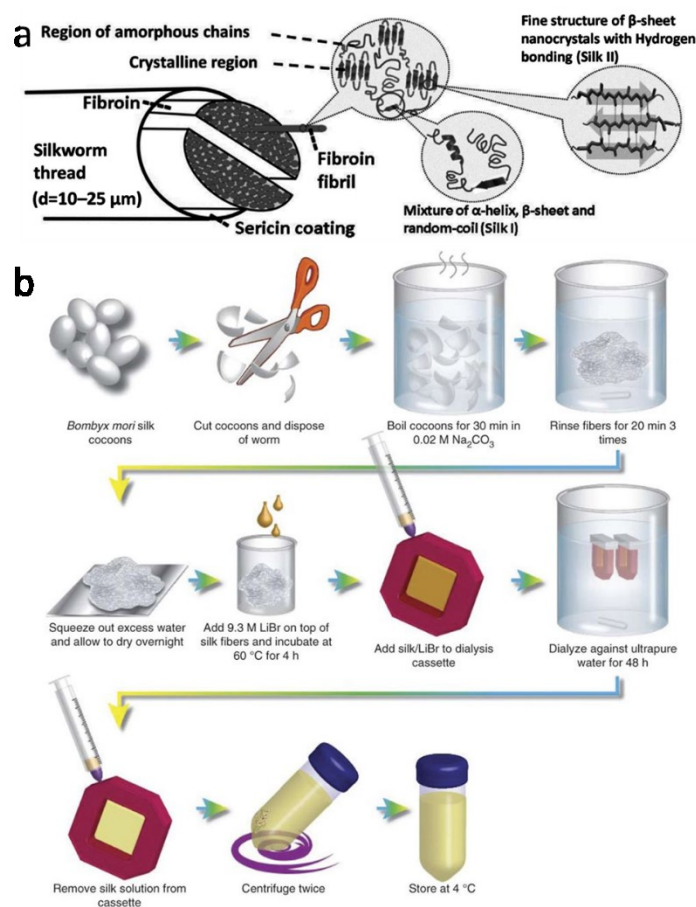

Figure 10. (a) The silkworm cocoon structure.[139] Reprinted from ref. 139 with permission from Wiley, copyright 2015. (b) The extraction of silk fibroin from silkworm cocoon.[141] Reprinted from ref. 141 with permission from Springer Nature, copyright 2011.

The antiparallel β-sheets are stabilized by strong inter and intramolecular hydrogen bonds and van der Waals interactions. The multi-domain morphology is responsible for the superior stretchability and mechanical strength of silk fibers because partially crystallization by β-sheets allows dynamic bonding and reorientation of molecular chains.

The amino acid sequence of silk is complicated and depends on the creature species. For instance, *B. mori* silk consists of 350 kDa heavy chain and 25 kDa terminal light chains, which are linked by a disulfide bond to form heavy-light chain complex.[142] The glycoprotein of ~25 kDa, P25,

bond with the heavy-light chain complex usually by hydrophobic interactions to maintain the chain complex stability. The heavy chains mainly contain 46% glycine (G), 30% alanine (A), 12% serine (S), 5% tyrosine (Y), 1.8% valine (V), and 4.7% of the other 15 amino acids.[138,141] The heavy chain forms the crystalline regions with aliphatic amino acids glycine and alanine assembled into two series of hexapeptides, GAGAGS or GAGXGY.[8,143]

Considering the cost and availability, the most common silk source is the *B. mori* silkworm cocoon.[138] To obtain pure silk from cocoons, a robust silk fibroin extraction protocol has been widely used to obtain silk materials with high purity (Figure 10b).[141] Three steps for extracting silk includes degumming, dissolution, and dialysis. Silkworm cocoons first undergo a degumming process to remove the sericin proteins that often cause immune response in biomedical applications.

Sericin is a proteinaceous glue, which mainly consists of following amino acids: serine (33.43 mol%), aspartic (16.76 mol%), glycine (13.49 mol%), threonin (9.74 mol%) and glutamic acid (4.42% mol%). However, the silk fibroin has different major amino acid composition, e.g. only 1.3 mole% aspartic acid, 1.0% glutamic acid.[144] The difference of amino acid components provides base for selection during degumming. And serein present on the surface of the silk fiber to bind the silk fibroin together, is easily accessible to the degumming chemicals. During the degumming process, the sericin undergoes hydrolytic cleavage followed by dissolving in the solution.[145,146,147] Up to now, mainly three kinds of degumming approaches have been explored in terms of sericin removal efficiency and physico-mechanical properties of silk fiber.

Firstly, alkali, where Na_2CO_3 is frequently utilized, hydrolyses proteins by attacking peptide bonds.[144] However, this chemical reaction is nonspecific. Depolymerization and reduced mechanical property of silk fibroin can happen. Secondly, acidic solution, e.g. organic acids (acetic, formic, lactic) and strong inorganic acids (sulfuric acid, hydrochloric acid) are also utilized, with the latter ones have better sericin eliminating effect.[148] Diluted acids specifically break the bonds linking aspartic and glutamic acid, which are mainly present in secirin. Therefore, good tensile strength and elongation of silk are usually obtained in purified materials. Third, enzymes (such as trypsin, papain and bacterial enzymes), can be used for treatment. This approach usually carries out at mild condition and has advantage of high reaction specificity.[144,146] After degumming, other approaches can be utilized for dissolving silk fibroin to obtain homogenous silk solution. Inorganic salts, fluorinate organic solvents, ionic liquids and concentrated acids can be used for these purposes.[149]

The general mechanism of dissolution is based on the cleavage of the intermolecular hydrogen bonding in silk crystalline regions and avoiding peptide bonding hydrolysis.[146,150,151,152] Among many solvents utilized for silk fibroin dissolution, lithium thiocyanate aqueous solution,[153] calcium nitrate/methanol,[154] N-methylmorpholine N-oxide,[146] $CaCl_2/H_2O/EtOH$ mixed solution,[155] LiBr aqueous solution[156] and ionic liquids[150] are the most frequently used with negligible silk decomposition. Finally, pure silk aqueous solutions can be obtained after intensive dialysis, with resulting materials to be processed into various forms such as fibers, films, gels, and foams.

To enhance the mechanical properties and water stability, methanol and water vapor annealing can be exploited to control the formation and content of β-sheets.[157,158] However, these regenerated silk materials are far weaker than natural silk counterparts.[158,159] To maintain the original structure of native silk nanofibers, liquid exfoliation of silk fibers recently is developed to prepare silk nanofibers.[160,161] Partial dissolution of silk fibers can significantly weaken the interfacial strength of nanofiber aggregates, and the subsequent intensive sonication will separate the nanofibers. Overall, in such a common approach, chemical treatment to decrease interfacial strength is combined with strong shear force for further exfoliation.

4. Fabrication and assembly of photonic structures

The next challenge in quest for high-performance photonic structures is fabrication of organized materials with periodicities at the different spatial scales. Although living creatures can create fascinating photonic architectures *via* natural growth, this process is very slow, and can last for years. To recreate these natural structures, different top-down engineering and bottom-up directed assembly are used as discussed in this section.

4.1. Top-down engineering of natural polymers

Engineering of nanostructured biomaterials to mimic the natural architectures requires advanced manufacturing techniques. In particular, well-established micro/nanofabrication techniques for bioderived polymers have been explored to construct photonic structures at multi-scales with high-resolution including photolithography, soft lithography, and nanoimprinting.[162]

4.1.1 Photolithography techniques

The photolithography is a universal fabrication technique that can be adapted to a wide selection of biopolymer materials.[162,163,164,165] Photolithography is exploited for micro/nanoscale patterning with a spatial resolution reaching a nanometer scale.[162] To adapt photolithographical approach,

the biopolymers can be modified by grafting photoactive functional groups to act as the photoresist layer. For example, the patterning of silk fibroin has been proposed by using so-called protein photolithography.[162,166,167] In this method, silk fibroin can be used as "bio-photoresist" after grafting the photo-reactive group (2-isocyanatoethyl methacrylate, IEM) to native silk fibroin, which renders them photo-sensitive.[162] The modified silk can be crosslinked in the presence of UV light to enable patterning over macroscale areas.[166] These photo-crosslinking approaches can also be extended to the patterning of cellulose materials.[163] With the help of photo acid generators and UV light, soluble trimethylsilyl cellulose can be converted into pristine insoluble cellulose. Thus, the photo-reaction under a photomask allows the fabrication of well-defined cellulose patterns.[163]

Another ubiquitous nature protein, keratin, has also been used with very similar fabrication strategy. Keratin is one of tough, durable biological materials possessing both high toughness and modulus, and with high content of cysteine and half cysteine.[168] The high sulfur content introduces abundant inter/intra-molecular disulfide bonding, enabling complex hierarchical structure of keratinous materials with polypeptide chains and filament-matrix forming lamellar/sandwich structures.[169]

According to X-ray diffraction, keratin crystalline structures can be classified as α- and β-type. The α-keratin is mainly found in mammals, such as wool, hair, nails, with basic right-handed α-helix conformation, which further organizes to intermediate filament by disulfide links.[170] The β-keratin is the primary component of hard avian and reptilian tissues, such as feathers, claws and scales, with laterally packed β-strands, which can be assembled to pleated sheet and further distorted to left-handed helical filament through hydrogen bonding.[171] Abundant disulfide bonds hinder the solubility of keratin in most solvents. And only strong oxidants are able to extract keratin to form aqueous soluble derivatives and enable further chemical modifications.[172] Photoactive keratin resist can be prepared by grafting with the photoreactive reagent 2-isocyanatoethyl methacrylate. The photoactive keratin resist can be further photo-crosslinked using photomask and UV-light. The un-crosslinked water-soluble area can be removed, leaving periodical microstructures for generating brilliant structural color.[173]

To further improve the resolution of the periodical patterns, electron-beam lithography has been introduced to fabricate partterned silk materials with feature dimensions of a few tens of a nanometer.[174] In this approach, 2D- and 3D-photonic structures can be constructed by using crystallized and amorphous silk either as a positive or negative resist (Figure 11a). In the case of positive resist, e-beam irradiation degrades crystallized silk into short polypeptides that are

water-soluble and therefore can be washed away during the process. On the other hand, the e-beam treatment of the amorphous silk in negative resist version can crystallize silk to make them water insoluble. As a result, photonic crystals with different periodicities with vivid structural colors can be constructed in both positive and negative resist processes (Figure 11b and c). Through multiple e-beam exposure, pyramid-like structures with the nanoscale dimensions can be generated (Figure 11d).[174] The resulting spatial resolution is around 30 nm, but the resolution could be further improved to 5 -10 nm by optimizing the fabrication parameters (such as resist layer thickness and electron-beam current). This technique shows great potential to overcome the main issues that face the current high-resolution nanopattern fabrications, including low electron sensitivity, line edge roughness and scalability constraints.
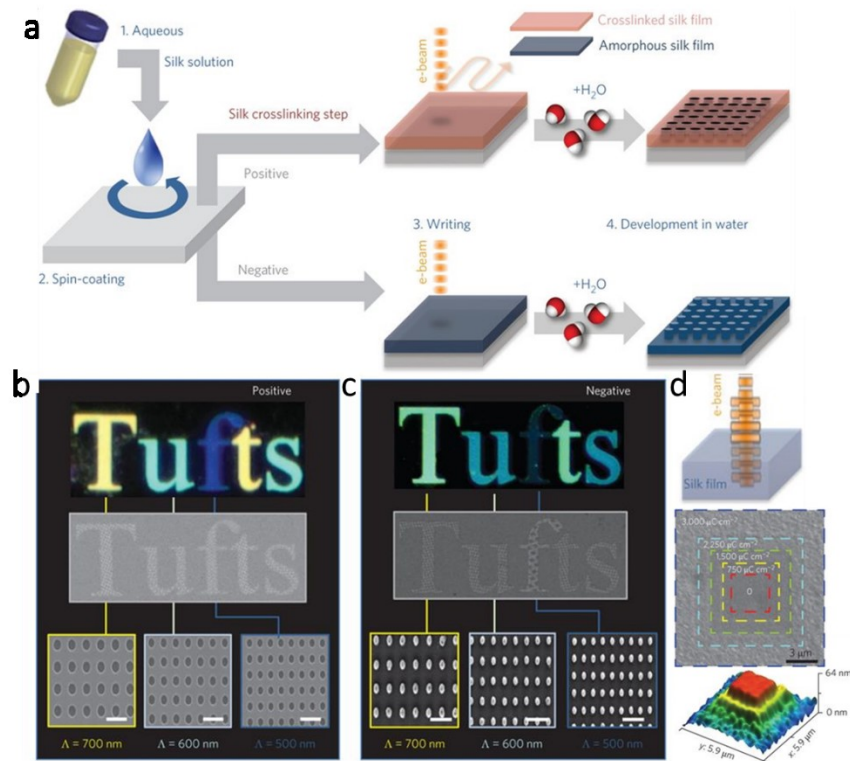

Figure 11. (a) The e-beam lithography on silk fibroin film. Dark-field and SEM images of patterned silk films produced on positive (b) and negative (c) resist. (d) Schematic illustration, SEM and AFM images of 3D silk nanostructure.[174] Reprinted from ref. 174 with permission from Nature Springer, copyright 2014.

Similarly, an ion beam and argon fluoride excimer laser can be adapted to pattern silk materials. [175 , 176] Combing ion beam and e-beam exposure enables the realization of complex 3D nanopatterns with desired shapes.[176] In recent studies, the fabrication approaches have been extended by the introduction of multiphoton lithography, which facilitates direct 3D patterning without photomask with high resolution and is applicable to various biopolymers.[177,178,179]

4.1.2 Soft-lithography

Soft lithography enables photonic arrays with a feature size down to nanoscale with examples including gratings, holograms, prisms, photonic lattices, and microlens arrays.[187] In a typical fabrication process, predesigned photonic structures are fabricated as a hard mold (e.g. silicon wafer) or soft mold (e.g. PDMS). By casting the aqueous biopolymers solution/dispersion on patterned surfaces, the complex topographies of a master can be replicated in the freely standing biopolymers film.

To date, various biopolymers, such as silk, chitin, chitosan, and nanocellulose, have been exploited for the fabrication of photonic structures with this approach.[180,181,182,183,184] For example, silk fibroins are ideally suited for soft lithography approach because of their good flexibility and strong adhesion with various substrates.[185] The patterned silk fibroin films can be subsequently crystallized by the formation of β-sheets when exposed to methanol vapor to improve stability. In this way, the free-standing silk fibroin films that replicate the original photonic structures can be obtained. By using simple casting of silk fibroin solutions, multi-phase micropatterning can be achieved that enables complex projected images.[185]

In addition to the replication of photonic structures in planar configuration, silk fibroin has also been used to replicate 3D photonic crystals resulting in the silk inverse opals (Figure 12a).[186] Due to the strict requirements of monodispersity of individual elements, artificial opals usually are constructed from very uniform silica or polymer spheres, such as polystyrene and poly(methyl methacrylate).[187,188,189,190] However, the resulting opals lack efficient and complete photonic bandgap because of the low refractive index contrast and incompatible filler ratio between spheres and space filling materials. To address this issue, replicas of these opals' structures can be fabricated in the form of so called inverse opals.[191] Subsequent removal of the opal templates produces high refractive contrast, and, thus, facilitates complete photonic bandgap.[192,193] The silk solution can infiltrate into the pre-assembled opals and, after drying and crystallization, form the inverse opal replicas after removing the original synthetic template by dissolving in an organic solvent. As a result, freestanding, mechanically strong, and flexible silk inverse opal structure are fabricated (Figure 12a). By choosing the initial templates, silk inverse opals with various photonic bandgaps are obtained to produce different structural color materials. To realize multiple optical functionalities, a combination of 2D diffraction gratings and 3D photonic crystals has been suggested.[194] In this strategy, PS opals are assembled on a silicon mold that possesses a diffraction grating surface, where PS opals can replicate the diffraction gratings pattern. This photonic structure is used as a template for "hierarchical inverse opals." The resulting diffractive

structure composed of 3D photonic lattice allows simultaneous control over the reflection (through the 3D photonic bandgap) and the transmission (through 2D diffractive structuring).[194]

In addition to the physical patterns of diffraction grating, chemical approach is also adopted to pattern the silk inverse opals. Silk as a protein is very sensitive to water vapor and UV light. The former can induce the formation of β sheet, and the latter is able to induce modest photodegradation of silk, further leading to the molecular rearrangement of silk fibroin. Controlling silk secondary structure allows the regulation of the photonic lattices, which can be utilized to fabricate silk inverse opals with different structural colors by the selectively exposing those to water vapor and UV light (Figure 12b).[195]
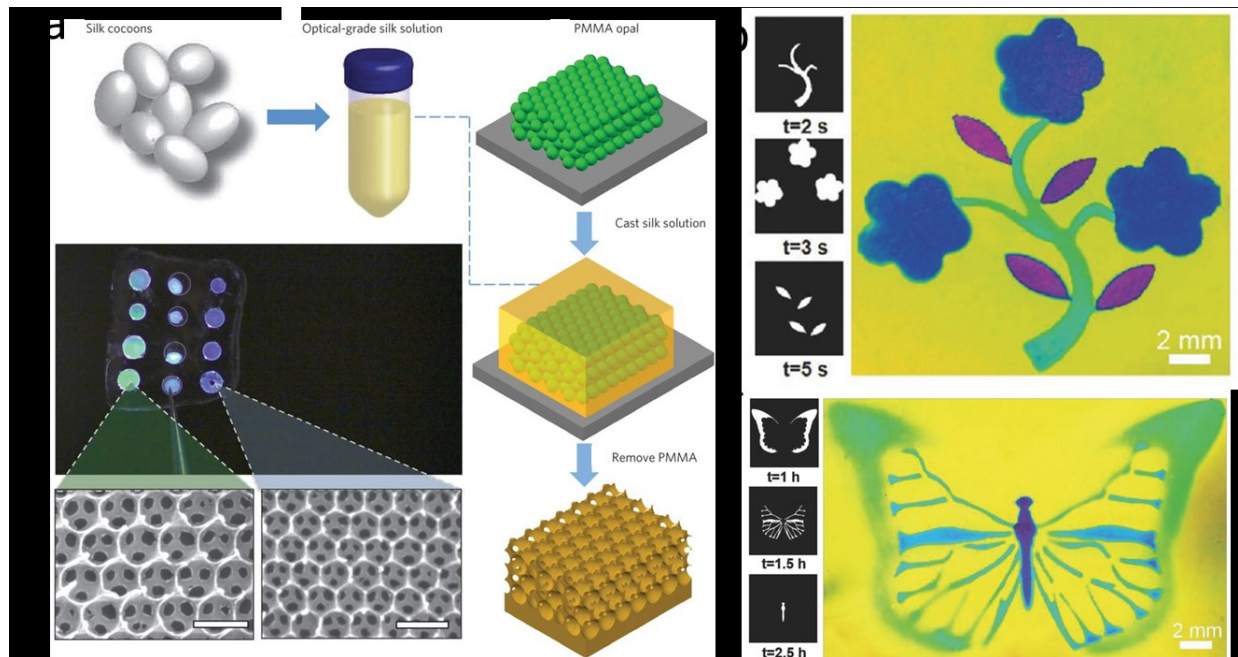

Figure 12. (a) Fabrication of freely standing silk inverse opal.[186] Reprinted from ref. 186 with permission from Nature Springer, copyright 2012. (b) Patterned silk inverse opal fabrication by exposing water vapor (top image) and UV light (bottom image) for different time.[195] Reprinted from ref. 195 with permission from Wiley, copyright 2017.

Comparing with a single photonic structure, the pre-engineered hierarchical structures with photonic-photonic coupling usually exhibit the brighter structural color, combined with additional optical functionalities. Indeed, this concept can be found in numerous examples in the living creatures.

For example, the combination of surface optical gratings and bulk chiral organization enables polarization sensitive iridescent colors for attraction of insects, communication and aid in their

camouflage against predators as, for instance, observed in flower petals and beetles. On the other hand, inspired by unique hierarchical organization, photonic nanocellulose-based films that contained cholesteric/chiral organization and microscopic surface gratings have been constructed through combination of top-down lithography and bottom-up self-assembly.[196,197,198] In this process of self-assembling CNC LC inks on a pre-designed patterned surface, the 1D nanocrystals can maintain the chiral organization if the grating trench width is significantly large than the CNC length (>200 nm).[197,198] Otherwise, the CNCs at the surface grating layer will be highly oriented along the imprinted trenches due to the packing constraints arising both from close-packing conditions under external confinements.[196] The resulting structures can be peeled-out to form free-standing films with polarized structural colors and enhanced asymmetric broadband circular dichroism. Additionally, other 2D photonic crystals and 3D micro-lens photonic elements can be integrated onto chiral CNC films for controlling the selective polarized light reflection and propagation that are non-achievable for regular chiral CNC film.[196]

4.1.3 Nano-imprinting

Nanoimprinting lithography (NIL) is a rapid fabrication technique, enabling large-area patterning of micro/nano-scale features.[199,200,201] Typically, NIL is facilitated by physical deformation of thermoplastic materials, which is induced by a hard mold under controlled pressure and temperature above the glass transition of a polymer. In particular, hot embossing imprinting technique has been well developed for patterning biopolymers with a high resolution.[49] Nanocellulose materials have been patterned with high-resolution micropillar arrays with different structural colors.[202]

Various 2D photonic crystals from silk fibroin have also been fabricated with NIL.[203] Photonic silk structures with high resolution can be obtained in both hot and room temperature NILs (Figure 13a).[203] After a crystallization where the silk films are annealed by the exposure to methanol to form primarily β-sheets, water-saturated silk films with a periodic pattern have been fabricated with a grating period of 277 nm.[203]
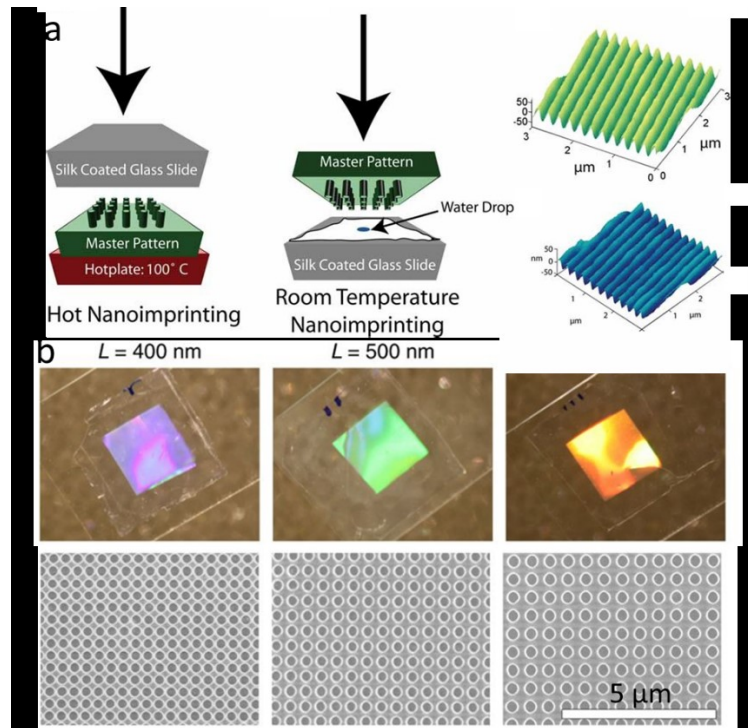
Figure 13. (a) Nanoimprinting with hot embossing and room-temperature embossing (left), and AFM image of diffractive grating patterned by room-temperature imprinting (right).[203] Reprinted from ref. 203 with permission from Wiley, copyright 2010. (b) Photograph of photonic crystals on hydroxypropyl cellulose film produced by a combination of roll-to-roll and nanoimprinting.[204] Reprinted from ref. 204 with permission from Springer Nature, copyright 2018.

In a recent study, the common nanoimprinting technique was shown to be compatible with roll-to-roll processing to produce cellulose photonic crystals.[202, 204] This combination allows the fabrication of large-scale 2D photonic cellulose structures with submicron periodic lattices (Figure 13b).[204] The patterned photonic films exhibit tunable structural colors and offer different optical functionality by integrating with optically active components.

4.2 Bottom-up directed assembly of biopolymers

Bottom-up assembly is capable of controlling biopolymer organization at the molecular scale, which enable construction of hierarchical photonic structures at multi-length scales by exploiting different environments (e.g. pH, temperature, humidity, shearing).

4.2.1 Solvent evaporation driven assembly of chiral nematic nanostructures

To obtain chiral photonic properties, the natural chiral structure with defined pitch into submicron range for visible wavelength reflection should be assembled. Aligning 1D nanoscale building blocks into hierarchical 3D organization at nanoscale length scale is challenging.[40] Efforts have been made to fabricate artificial chiral materials by using 3D printing,[205] brush-induced self-

assembly,[206] and magnetic-field-assisted slip-casting techniques,[207] but characteristic structural features of such composites are usually orders of magnitude larger than their natural counterparts. The common approach to fabricate the chiral nanostructures is the self-assembly of 1D biopolymers nanocrystals in concentrated and drying dispersions undergoing LC-solid transition. Various biopolymers have been reported to assemble into chiral nematic LC phase in dispersion when the concentration reaches a critical value, such as *fb* virus,[208,209] cellulose nanocrystals,[210] chitin nanocrystals,[211] and amyloid nanofibrils.[212] During the assembly, these biopolymers undergo isotropic-chiral nematic transitions when concentration increases (Figure 14a).[212]
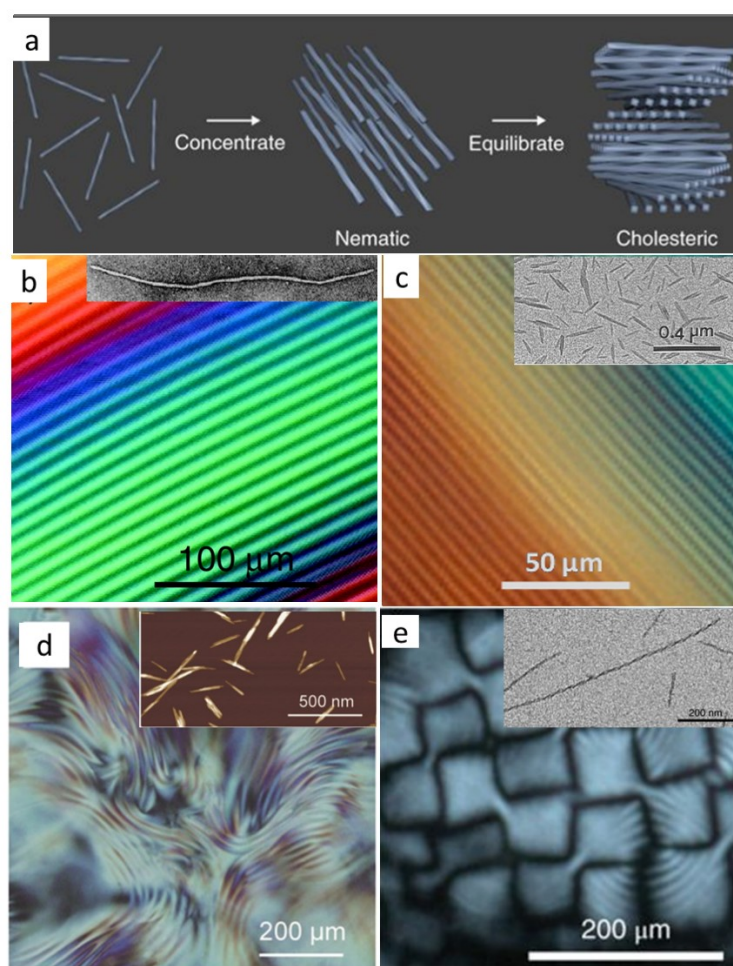

Figure 14. (a) Self-assembly of rod-like biopolymers into chiral nematic nanostructures in the concentrated dispersionss.[212] Reprinted from ref. 212 with permission from Springer Nature, copyright 2018. Polarized optical microscopy images of chiral nematic liquid crystal phase of fb virus[208] (b). Reprinted from ref. 208 with permission from American Chemical Society, copyright 2000. Cellulose nanocrystals[210] (c). Reprinted from ref. 210 with permission from American Chemical Society, copyright 2014. Chitin nanocrystals[211] (d) Reprinted from ref. 211 with permission from Wiley, copyright 2015. and Amyloid fibrils (e)[212]. Reprinted from ref. 212 with permission from Springer Nature, copyright 2018. Insets: the morphology of the films from corresponding rod-like biopolymers.

Above critical concentration, these LC dispersions presents a typical "fingerprint" textures observed by optical microscopy between crossed polarizers (Figure 14b-e).[208,210,211,212] The uniformity of pitch morphology and their orientations critically affect the appearance and the width of reflection maximum. To date, however, only the CNCs films demonstrate intense structural color after complete drying. The loss of colors that observed in other biopolymers films is usually related to distortion of chiral morphology during drying or the pitch distance does not match the wavelength of the visible light. Chiral CNC phases acquire an appearance often called iridescence because the reflectance changes as the angle of view changes thus producing vivid colors with a broad spectral range.[213]

The assembly of the CNC dispersions into chiral nematic phase is governed by balancing the attractive (hydrogen bonds and van der Waals forces) and repulsive (steric and Coulombic) interactions as CNCs dispersions undergo phase transition from an isotropic to a cholesteric LC phase upon increasing concentration. This phase transition strongly depends on the aspect ratio, length and surface potential of CNCs and ions strength in aqueous dispersion. The onset phase transition concentration is expected to be lower if the CNCs have higher aspect ratio.[214]

For example, the onset concentration of CNCs (aspect ratio of 44-73) that are derived from bacterial cellulose is around 0.42 wt%,[215] while onset concentration of wood CNCs with smaller aspect ratio of 34 increases to above 2 wt%.[216] The role of aspect ratio and onset transition concentration can be explained using the classic LC phase transition theory by Onsager: $C_i = 3.3\rho/AR$,[217] where C_i is the onset (isotropic to biphasic) transition concentration (wt.%), ρ is the density and AR is the aspect ratio. The experimental results of the CNC LC transition have been demonstrated to be well consistent with this theory.[218] However, too long CNCs are less rigid, which frequently results in the formation of disordered/web-like or nematic organization without the chirality.

Before the CNCs completely organize into chiral nematic phase, there is an isotropic−anisotropic biphasic region with a wide concentration range of 2-15 wt%.[216] In this biphasic region, the pitch length decreases because of remove solute. Generally, chiral nematic phases in concentrated solution have long-range LC order with the pitch of helical structures ranging from 1 to 50 μm. For instance, it has been reported the average pitch length drops from 15 to 2 μm when the dispersion concentration is increased from 2.5 to 6.5 vol%.[216] Accordingly, an increase of twisting angle between neighboring CNCs from about 1° up to 4° has been observed.[216] In polydisperse CNC dispersions, the CNCs with higher aspect ratio firstly self-organize into chiral nematic phase, while the shorter CNCs are still maintained in the isotropic phase thus forming bi-phasic region.

Adding electrolytes can significantly increase the onset concentration for LC phase formation because the H^+ counterions on CNCs will be replaced by larger ions, which will increase the effective CNCs diameter and repulsive forces.[219] With the increase of counterion size, the critical concentration generally increases in the order $H^+ < Na^+ < K^+ < Cs^+$.[220] However, the electrolytes should not involve multivalent ions such as Al^{3+} and Mg^{2+}, which will produce an ionic crosslink with CNCs to form hydrogel with random network morphology and no chiral properties.[221]

The interesting property of the CNC LC phase is the ability to preserve the chiral nematic structure in the solid film after complete drying.[222] Total removal of water causes chiral pitch to decrease to submicron range, resulting in Bragg's reflection in the visible spectrum and the appearance of bright structural colors. The appearance of a light reflection with exclusively positive ellipticity in the circular dichroism spectra of CNCs films suggests the left-handed chirality. This left-handed helicoidal arrangement of nanocrystals in solid films show the helicoidal axis mostly perpendicular to the film surfaces.[223] However, CNCs films still show iridescence under left-hand and right-hand polarizers in many cases, although the reflection in the right-hand channel usually is much higher than that of the left-hand channel.[15,224,225] This difference may be partially related to the mis-aligned multi-domain CNC LC structures.

Photonic properties of CNC solid films are closely related to the intrinsic microstructure as controlled by phase state transformations during the drying process. Apart from these intrinsic structures, other variable drying conditions (different humidity, temperature, hydrophobicity of substrates, and magnetic field presence), might affect the pitch length and overall uniformity of chiral structures.[226] For example, the hydrophobicity of substrate was shown to affect the orientation of LC tactoids as well as the emergence of macroscopic ordered phases in non-spherical LC droplets (Figure 15).[227] In the case of hydrophobic substrate (Figure 15 a and b), the CNC tactoids firstly merge into partially ordered phase beneath the upper liquid−air interface and then vertically spread along the side face to the bottom. In sharp contrast, the long-range ordered phase initially appears at the bottom center of the droplet and then horizontally spreads from the center to the edge in the presence of hydrophilic substrate (Figure 15 c and d). The behavior was associated with the Marangoni flow, pinning effects and the dynamic interactions between modified substrates and CNCs. However, details of the chiral organization formation in the solid state are still poorly understood, which largely restricts the control of the alignment and the resulting pitch value of the LC phase.
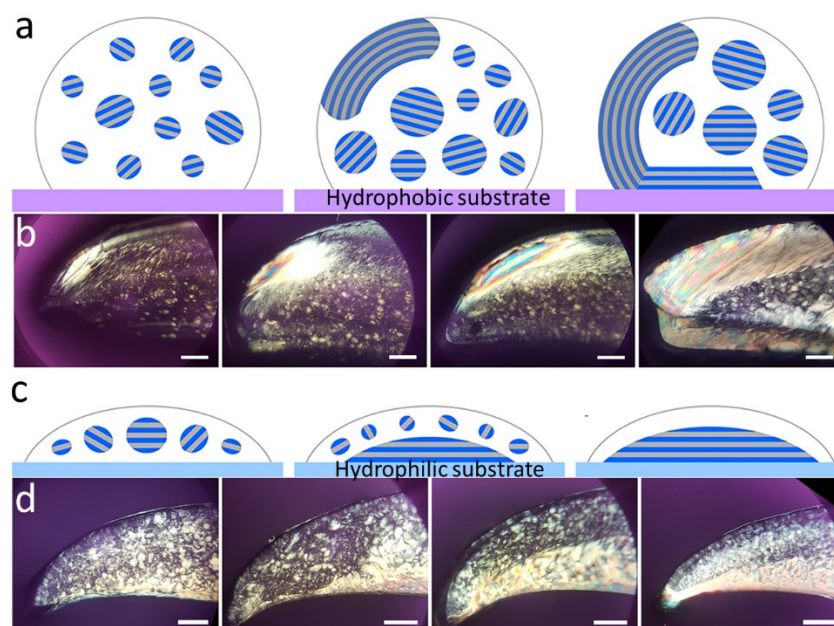
Figure 15. The evolution of discrete LC tactoids and continuous chiral nematic phases in the droplets of aqueous CNC dispersions on hydrophobic (a-b) and (c–d) hydrophilic substrates. (a and c). (b and d) are the polarized optical images of CNC droplets with standing time of 1, 3, 6, and 24 h. Scale bars are 500 μm.[227] Reprinted from ref. 227 with permission from American Chemical Society, copyright 2019.

Assembling in confined geometry has been demonstrated to be a promising method to control the chiral properties. For instance, uniformly aligned chiral LC CNC structure can be obtained by confined drying within thin capillaries.[228] This confinement enables tight control of fast and uniform birefringent CNC film formation under directional flow with uniform chiral structure that possesses narrow optical reflection band. On the other hand, microfluidic flow can be used to generate monodisperse CNCs microdroplets in oil.[229] This confined geometry allows the formation of an ordered chiral nematic shell, growing inward from the water-oil interface. After complete drying, however, these LC microspheres shrink into non-uniform microparticles with wrinkles. Slowing down the water evaporation rate has been recently proved to be efficient for the fabrication of CNC films with uniform structure.[15] The conventional ambient environmental conditions usually lead to the outward capillary flow, resulting in the well-known "coffee stains". Introducing an immiscible layer of hexadecane oil on the CNCs LC dispersion micro-layers enables the slow water evaporation for avoiding the capillary flow.[230] It is worth mentioning that many strategies are only demonstrated to produce uniform chiral structural color at micro-level, and it still remains unknown whether it is possible to extend these concepts to large-area materials with uniform color.

In addition, a cellulose derivative, hydroxypropyl cellulose (HPC), is a promising chiral photonic material with the advantages of low-cost, industrial scale production, and being non-toxic.[231] At high concentration (usually more than 50%), HPC aqueous dispersions can form a chiral nematic phase due to the chain stiffness of the polymer.[232] This chiral organization can be preserved in the solid film after totally removal of water as similar with the CNCs. The resulting films show vivid iridescent structural colors.[233] Manipulation of the reflection light is accessible by controlling the initial HPC concentration with higher concentration leading to smaller photonic bandgap and the structural color shifting from red to blue.[234]

4.2.2 Self-assembly of polymer-CNC chiral composites

As known, completely dried thin CNCs films are brittle, which largely limits the practical optical applications. The addition of the external components has been demonstrated to manipulate the mechanical stability and the pitch length of the chiral structures.[235] A common example is the combination of CNCs with water-soluble polymers. Blending CNCs with polymers can not only control the pitch length, but also significantly enhances the mechanical performance of the CNC composite films. The selection of polymers for matrices is extremely important for realizing uniform chiral morphology and balancing the attractive and repulsive interactions that governs the CNC-polymer assembly.

To date, zwitterionic surfactants and various synthetic polymers, such as polyacrylate, poly(ethylene glycol) (PEG), and poly(vinyl alcohol) (PVA), have been introduced to co-assemble with CNCs to produce flexible iridescent films.[239,235,236,237] For example, CNCs can be assembled with PEG into large-area flexible chiral nematic solid films with uniform structural color upon slow drying (Figure 16).[239] The combination of flexible polymers and stiff CNCs also result in enhanced mechanical performance. The structural color can be regulated in a wide spectrum range from blue to red by controlling the composition. The increase of polymer content increases the photonic bandgap to reflect the light at higher wavelength with multi-color domains visible at microscopic level (Figure 16d, e). No phase separation occurs in these systems due to the affinity of PEG with CNCs through hydrogen bonding interactions.[239]

Natural polymers are also explored for combining with chiral CNCs for controllable photonic band gap and enhanced mechanical properties. For instance, hemicellulose is abundant natural polymer derived from plants, which wraps around nanocelluloses in the natural wood cell wall.[238] The strong interactions with nanocelluloses make them a good candidate for the fabrication of robust CNC/polymer nanocomposites.
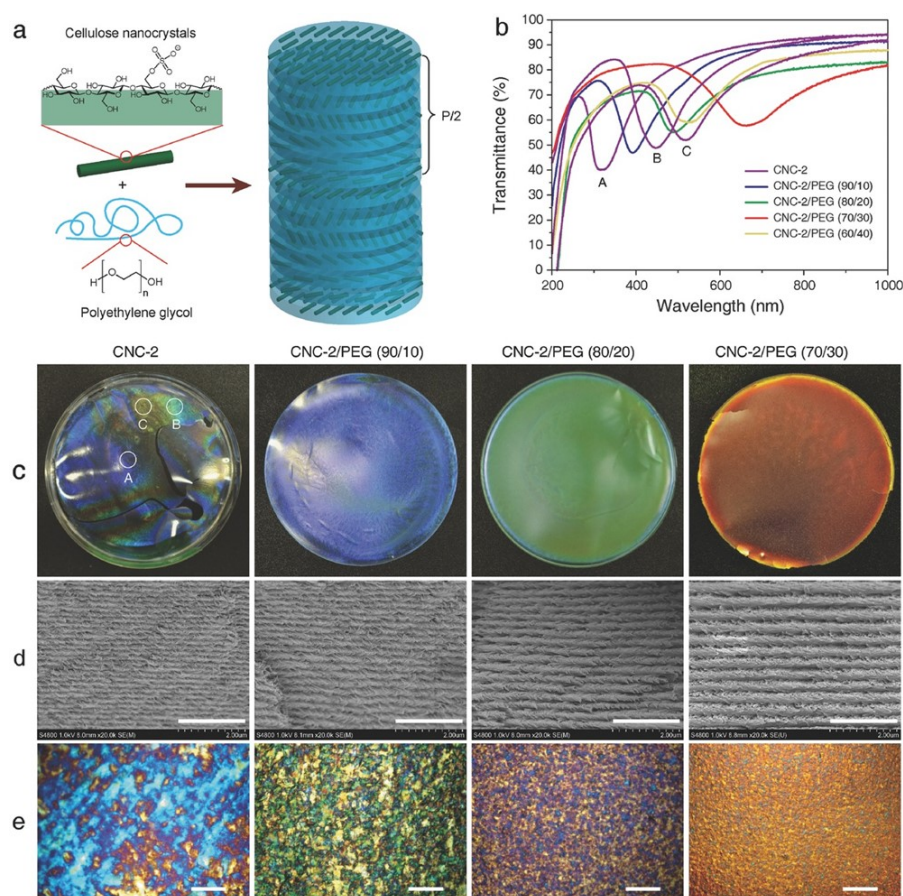
Figure 16. (a) The co-assembly of CNC/PEG chiral films. (b) UV-vis spectra of CNC/PEG photonic films with different PEG loading. (c-e) Morphology of CNC/PEG photonic films with different PEG loading: photograph (c), SEM images of film cross-sections (d), and POM images (e). Scale bars in d and e are 2 μm and 200 μm, respectively.[239] Reprinted from ref. 239 with permission from Wiley, copyright 2017.

In recent study,[240] three types of hemicelluloses (xylan, dextran, and pullulan) have been blended with CNC and it has been demonstrated that the CNC chirality is maintained in all CNC composite films without phase separation. The resulting hemicellulose/CNC films show improved mechanical strength and vivid structural colors ranging from blue to red by controlling the compositional content.

4.2.3 Mechanical force induced alignment and birefringence

The anisotropic alignment of biopolymer nanocrystals directly affects the refractive index difference along and perpendicular to the alignment direction.[241,242] This optical anisotropy, birefringence (Δn), is defined as the double refraction of light in a transparent molecularly-ordered material due to the existence of orientation-dependent differences in refractive index.[243] Light polarization can be changed when light passing through anisotropic materials with a phase difference (δ) between parallel and perpendicular direction to the alignment according to

$\delta = 2\pi d\Delta n/\lambda$, where d is the thickness of the sample and λ is the wavelength of light.[244,245] The capability of altering light polarization makes birefringent materials common in natural materials such as the eyes of mantis shrimps and the shell of a beetle.[65,246] Unlike the iridescent colors that can be directly observed for the chiral CNC films, the birefringence-caused colors are only visible under crossed polarizers.

To obtain uniform orientation at all spatial scales, the most frequently used strategy is the shearing-induced alignment. For instance, Tseng et al.[247] reported that assembling silk fibroin in confined geometry combined with mechanical tension could generate hierarchical organization with controlled morphology at multi-length scales (Figure 17a). Strong shearing force can induce the isotropic-anisotropic transition and the orientation of biopolymer chains for significantly enhancing the mechanical properties, accompanying with induced birefringence.[248] Mechanical tension is applied on biopolymer hydrogel materials because they have good stretchability, which allows large deformation for realizing high degrees of orientation.[249] As shown in Figure 17b, chemical and physical crosslinked cellulose hydrogels exhibited deformation-induced anisotropy under shearing force.[249] This orientation then is permanently fixed after drying, with the orientation degree higher than that in regular hydrogels because the shrinkage of volume will further increase the molecular chains orientation.

In addition, in-situ polymerization or crosslinking of CNCs are widely adopted to fix the orientation of nanofibrils.[244, 250] As a result, the alignment, can be permanently maintained even after removing the external stresses. For example, centimeter-scale mono-domain nematic hydrogels have been demonstrated by in-situ polymerization of highly aligned CNCs.[244] CNCs that mix with monomer (acrylamide) and photoinitiator can self-align along the shearing direction by shearing with a cover slide. After UV-polymerization, the mono-domain nematic organization is capable of producing homogeneous birefringence under crossed polarizers, even after multiple reversible swelling cycles. By controlling the swelling volume, this hydrogel demonstrates different structural color because of the change of the CNC packing (Figure 17c).[244]

Strong shearing flow produced by the printing and spinning of dispersions was shown to be an efficient way to control the alignment of LC phases.[251] For example, the 3D printing has been adopted for local control the orientation to reach site-specific mechanical and optical properties. The alignment dynamics under the shear stresses applied to concentrated CNC inks during inkjet printing has been recently studied.[251] The alignment dynamics of CNCs under shear flow results in dynamic birefringence, which is used to evaluate the alignment behavior. Higher shear rate and

CNCs concentration can induce the CNC alignment much faster because of steric constraints and hydrodynamic interactions.
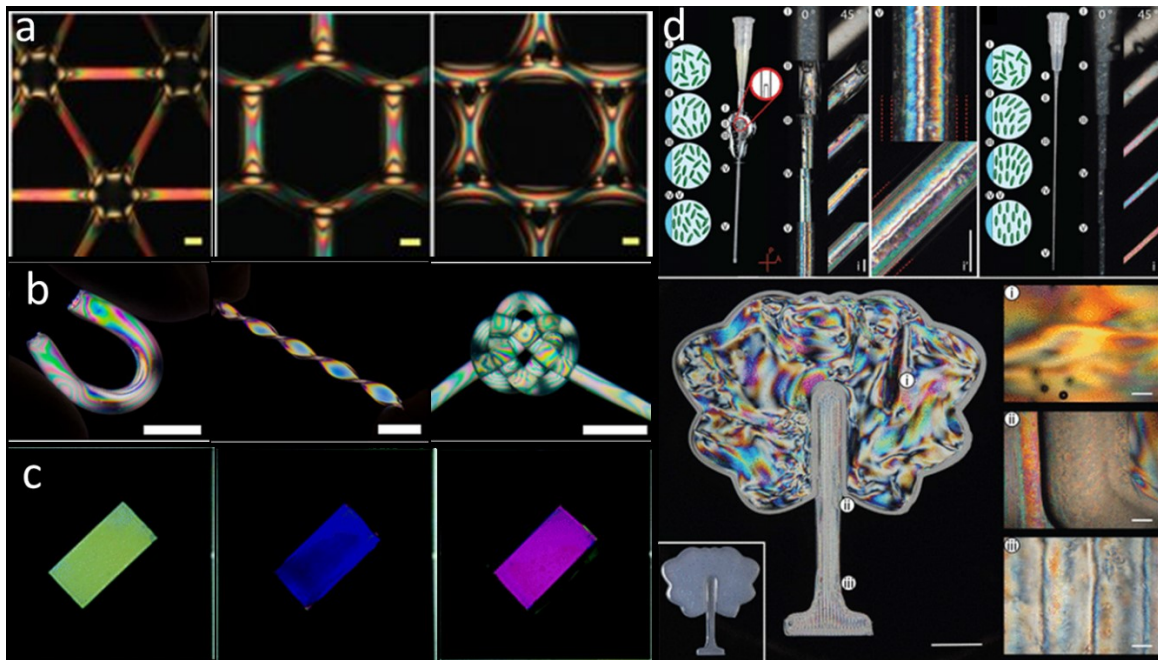

Figure 17. Birefringent structural colors of biopolymer alignment. (a) Birefringence of silk nanofibrillar alignment generated within periodic topography (triangular, hexagonal and tri-hexagonal), scale bars: 100 μm.[247] Reprinted from ref. 247 with permission from Springer Nature, copyright 2017. (b) Iridescent birefringence patterns of deformed cellulose hydrogels under polarized light. Scar bar: 1 cm.[249] Reprinted from ref. 249 with permission from American Chemical Society, copyright 2017. (c) Homogeneous birefringence of CNCs fixed in in-situ polymerized hydrogel.[244] Reprinted from ref. 244 with permission from Royal Society of Chemistry, copyright 2018. (d) Birefringent patterns with CNC alignments produced by 3D printing.[251] Reprinted from ref. 251 with permission from American Chemical Society, copyright 2018.

Complex CNC birefringent patterns have been be printed by controlling the shear flow in 3D printing nozzles of different geometries (Figure 17d).[251] In addition, this anisotropic alignment leads to anisotropic stiffness and swelling behavior in the longitudinal direction compared to the transversal direction, yielding complex 3D morphologies in water.[252] Mittal et al.[253] used extensional flow field produced by a double flow-focusing channel to achieve structural nanocellulose materials with high arrangement. Individual nanocellulose fibrils can rotate to pack together under fast shear flow. The resulting alignment provides the mechanically strong microfibers with mechanical strength of 1.5 GPa and elastic modulus of 80 GPa.

4.2.4 Assembly of nanofibrillar biopolymer networks

Random fibril networks can achieve controllable optical transparency from clear state to bright whiteness.[70] Manipulating the surface roughness, diameter of biopolymer fibrils, and the porosity of the films allows regulation of light scattering in the fibril networks. For instance, regular

cellulose papers, such as filter paper, show high whiteness due to the rough surface, large fiber size and high porosity.[254] Significant decrease of the fiber size can largely minimize the light scattering for obtaining highly transparent cellulose papers, so-called cellulose nanopapers. These cellulose nanopapers with smooth surfaces can be produced by filtration of nanocellulose and subsequent hot-compression (Figure 18a).[254] The 40 μm-thick papers that are produced from CNFs show high optical transmittance of 92-93%, while papers with 25 μm fibers with the same thickness exhibit transmittance of only 40% with the haze value decreased from 77% to 20%. Surface polishing of cellulose nanopapers can enhance the optical transparency by minimizing the light scattering (Figure 18b).[255]
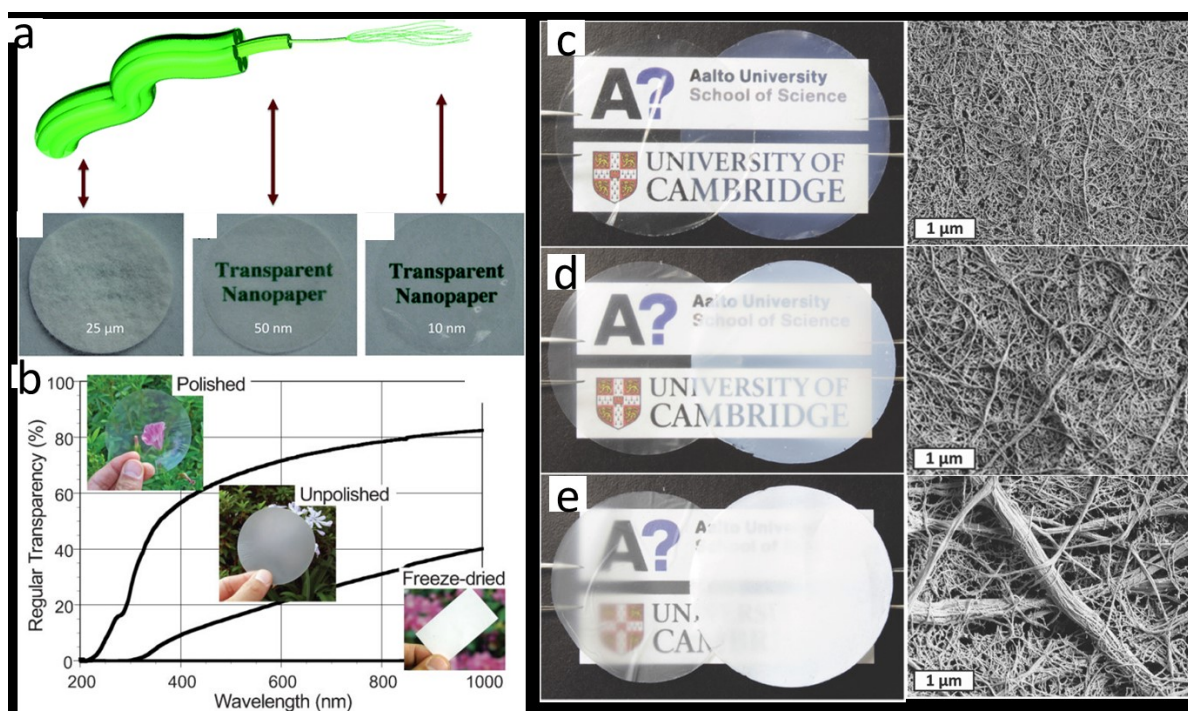

Figure 18. (a) The size effect of cellulose fiber on the optical transparency of cellulose films.[254] Reprinted from ref. 254 with permission from Royal Society of Chemistry, copyright 2013. (b) Light transmittance of the cellulose nanopaper before and after polishing.[255] Reprinted from ref. 255 with permission from wiley, copyright 2009. (c) Photographs of the compact CNF films (left) and, porous membranes of CNFs dried from octane (right) when using c) the finest, d) the medium, and e) the coarsest fibrils.[256] Reprinted from ref. 256 with permission from Wiley, copyright 2018.

The porosity of the cellulose films with proper dimensions also significantly affects the light scattering. The internal random pores in cellulose films can cause strong light scattering due to the large difference of refractive index between air and cellulose.[257] Recently, porous photonic CNC materials with monodisperse polystyrene spheres (diameter ~1.27 μm) as sacrificial templates have been reported.[258] The porous geometry combined with a high filling fraction facilitates the greatly increased light scattering.

Freeze-drying can be used to construct opaque materials because of its capability of forming highly porous structures. Inspired by the photonic network structures in white beetle wing scales that can achieve brilliant whiteness, CNF films with comparable scattering efficiency have been fabricated.[256] To obtain large fibrils, a sequential centrifugation technique is used to separate CNFs from polydisperse CNF dispersion. Solvent exchange combined with freeze-drying resulted in a highly porous structure because drying water based hydrogels in ambient conditions will result in a dense structure. The resulting CNF membranes look brilliantly white and exhibit a high broadband reflectivity (60-80%), reaching up to 90% for the shorter wavelengths (Figure 18c-e).

4.2.5 Infiltration of porous structure for transparent biomaterials

To obtain transparent nanocellulose films, the presence of large pores in the fibrillar network should be minimized. An alternative strategy to conventional compressing/capillary methods for preparing transparent structures is filling up pores with other materials that possess a similar refractive index. For example, filling the pores of cellulose microfibers papers with ultrafine CNFs resulted in transparent composite paper with transmittance up to 90% (Figure 19a).[259]
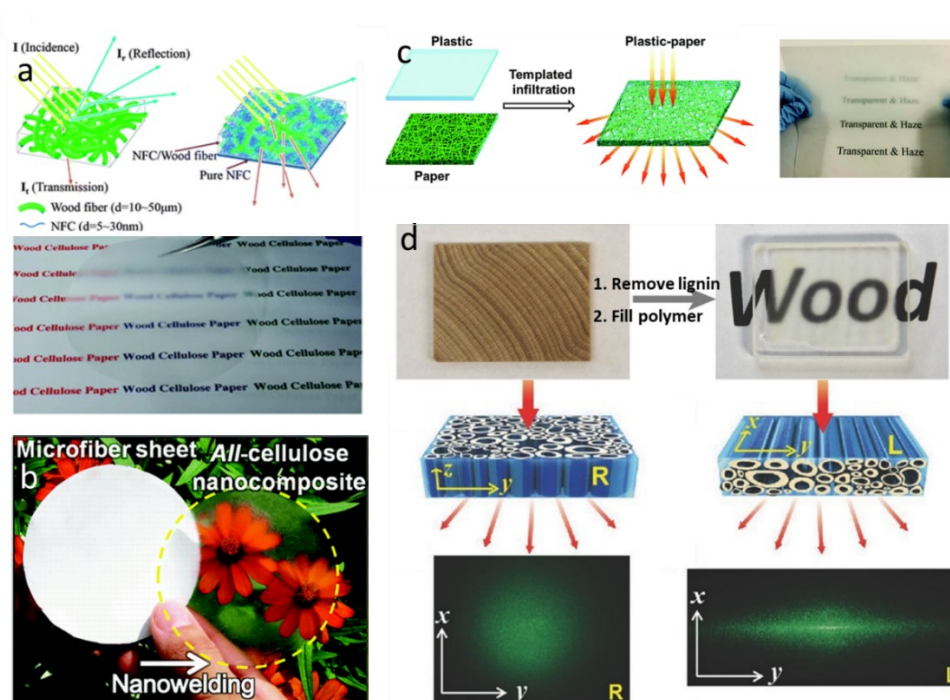

Figure 19. (a) Clear cellulose film by filling cellulose paper with cellulose nanofibers [259] Reprinted from ref. 259 with permission from Royal Society of Chemistry, copyright 2013. (b) Transparent cellulose paper by partially dissolving/regeneration.[260] Reprinted from ref. 260 with permission from American Chemical Society, copyright 2011. (c) Transparent cellulose-polymer paper by filling conventional paper with refractive-index matching polymer.[261] Reprinted from ref. 261 with permission from Royal Society of Chemistry, copyright 2016. (d) Transparent wood by filling delignined wood with refractive-index-matching polymer.[264] Reprinted from ref. 264 with permission from Wiley, copyright 2016.

Regular cellulose papers can be directly transformed into transparent paper through self-dissolving and regeneration (Figure 19b).[260] Decreasing fiber diameter through partial dissolution and filling the pores with cellulose solution dramatic reduces the light scattering. Other polymers such as epoxy resins have also been added into cellulose papers to reduce optical losses (Figure 19c).[261] The similarity of refractive indices and smooth surface led to a minimized surface and bulk scattering with resulting high optical transparency.

This design principle can be also extended to constructing transparent plastic-wood materials, so called transparent wood.[262,263,264] Wood shows highly anisotropic structures, where vertical micro-channels and wood cells uniformly align along the axial direction with the wood cell walls composed of lignin, cellulose fibers, and hemicellulose. After the removal of lignin by chemical treatment, the wood shows a white appearance due to light scattering in empty micro-channels. Infiltrating refractive index-matching polymer into these channels leads to a highly transparent wood composites with anisotropic optical properties (Figure 19d).[264]

4.2.6 Evaporation assisted assembly of biopolymer opals

The widely used building blocks for artificial opals are silica and polystyrene (PS) spheres because of their availability, controllable size, surface chemistry, and relative monodispersity. [48,265,266] However, preparing monodisperse submicron spheres from biopolymers is extremely challenging. Biopolymers directly derived from natural sources can form nanoparticles only using the additional post-fabrication approach. The common fabrication method is the microfluidic technique, which is appropriate for uniform microhydrogels, but these hydrogel spheres will shrink and be distorted after drying.[229] Thus, biopolymers are commonly used as a matrix to replicate the artificial opal to fabricate the inverse opal.

Among recent examples, natural pigment biopolymer (melanins) is capable of forming nanoparticles organized into periodical photonic structures to generate vivid structure colors similar to those in plants and animals (e.g., structurally colored feathers).[267,268] Additionally, polydopamine (PDA) is widely used for constructing photonic structures.[269,270] For instance, PDA nanoparticles with diameter of 146±15 nm and a high refractive index of 1.74 have been used for constructing the opal structures.[271,272,273] Vertical evaporation-based self-assembly facilitates the formation of well-organized thin films with different structural colors (Figure 20a).[274]

In contrast to conventional PS particles that display a negligible absorption of light in the visible range, the broad absorption spectrum of PDA microbeads can reduce incoherent scattering and enhances color saturation and non-iridescent photonic structures.[275] In addition, PDA/silica core-

shell structures, featuring high-reflective-index cores and low-reflective-index shells, are assembled, which show much higher reflectance than pure PDA spheres.[275] The large reflective-index contrast between the core (1.74) and shell (1.45) as well as the broad absorption range largely increase the brightness and saturation of the resulting color (Figure 20b).
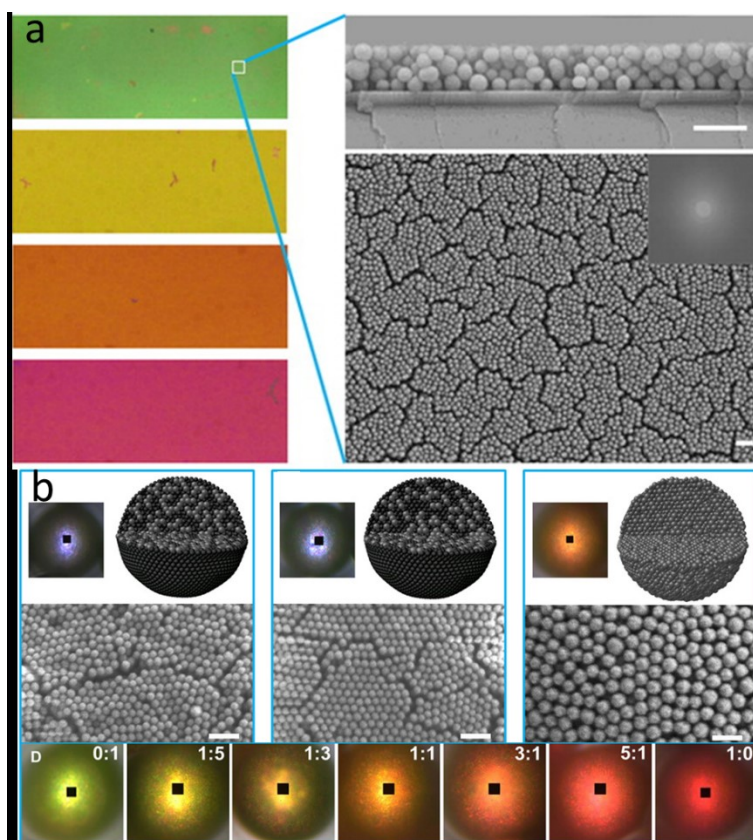

Figure 20. (a) Iridescent opal-like films self-assembled from monodispersed PDA spheres with different concentration.[274] Reprinted from ref. 274 with permission from American Chemical Society, copyright 2015. (b) Iridescent microbeads from binary PDA-silica core-shell spheres with different core-shell ratio.[275] Reprinted from ref. 275 with permission from American Association for the Advancement of Science, copyright 2017.

4.2.7 Layer by layer assembly of biopolymer structures

Layer-by-Layer (LbL) assembly is a facile, highly versatile and universal approach to build layered nanocomposites with uniform and precisely controlled thickness on both planar and non-planar structures.[276,277,278,279] A variety of complementary intermolecular interactions such as ionic pairing,[280] hydrogen bonding,[281] covalent bonding[282] and specific recognition[283] can be used as the driving force for the organized assembly. It affords a wide diversity in the selection of building blocks (e.g., polyelectrolytes, quantum dots, plasmonic nanoparticles, nanocrystals, nanofibers, nanosheets) and various deposition techniques (spin-coating, dip-coating, or spray-coating).[284,285,286,287,288]

Alternating deposition of two components that possess different refractive indices can results in 1D photonic structures, which exhibit bright structural color through multilayer interference.[27] Additionally, it has been demonstrated that alternating multilayered thin film deposited from high-refractive-index plasmonic nanoparticles with low-refractive-index polyelectrolyte can generate extensive red-shift and broadening of plasmon bands.[289,290,291] Super-efficient Förster resonant energy transfer (FRET) was also obtained by LbL assembly of different CdTe/CdSe quantum dots and charged polyelectrolytes, which present promising applications in photonic devices such as nanocrystal-based lasers.[292,293,294] These concepts were also well-demonstrated in the LbL assembly of biopolymeric photonic structures.

It has been exhibited that LbL assembly of low-refractive-index biopolymers with other high-refractive-index components can generate bright interference colors. For example, multilayered structure has been fabricated from titanate nanosheets/silk and silk components.[295] The refractive index of the 80 nm thick silk and the 40 nm thick titanate/silk layers were 1.56 and 1.82, respectively. Owing to the high refractive index contrast and uniform multilayer morphology, the resulting organized materials exhibit blue color with absorption peak centered at ~385 nm.
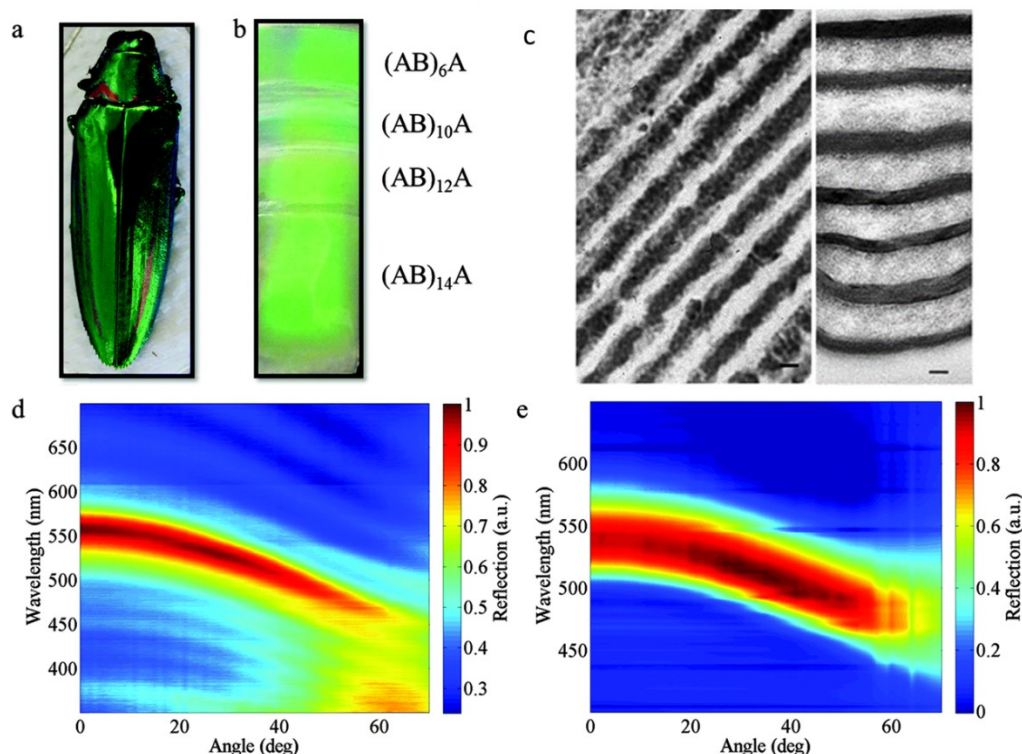

Figure 21. Photographs of the (a) *C. rajah* beetle and (b) LbL-assembled CNCs Bragg stacks with different stacks. (c) layered structure of beetle and CNC stacks. Color plots showing reflection as a function of wavelength and incidence angle for the (d) stacks film and (e) *C. rajah* beetle.[296] Reprinted from ref. 296 with permission from Royal Society of Chemistry, copyright 2015.

In another example, iridescent Bragg stacks have been fabricated from CNCs by LbL technique to mimic the structural color of beetles (Figure 21).[296] The high refractive index layer comprised of 13 bilayers of cationic polyethylenimine and anionic vermiculite clay, which possesses a refractive index of 1.65 with the thickness of 90 nm. The complementary layer of 40 bilayers of cationic colloidal SiO_2 and anionic CNCs has a refractive index of 1.42 and thickness of 288 nm. The resulting multilayer structure shows strong green color with reflection above 80%,[296] which is comparable to the natural beetle appearance. In addition, freestanding LbL films from anionic CNFs and cationic poly(vinyl amine) show angle-dependent structural color because of the thin film interference.[297] Alternatively, LbL assembled ultrathin CNC films demonstrate strong antireflection properties due to highly porous morphology.[298]

In addition to the above mentioned 1D photonic structures, 3D photonic structures can be also fabricated by combining the LbL assembly with other fabrication approaches including nanotransfer printing (nTP) and Langmuir-Blodgett (LB) deposition. For instance, large scale multilayer photonic opal crystals from colloidal micro-particles was fabricated by transferring monolayers of colloidal crystals formed at the air-water interface.[299] Moreover, chirality can be generated through manipulating the deposition angle of each layer during the LbL assembly. For example, biomimetic chiral photonic crystals with facile and precise tunable chirality were also fabricated utilizing LbL-LB assembly of colloidal inorganic nanowires with an accurately controlled rotating angle between layers. Not only a helical structure and homo-circularly polarized color reflection were observed, but also a chiroptical asymmetry factor by an interlayer arrangement was obtained.[300] Furthermore, large-area and crack-free 3D optical nanostructures fabricated by stacking multilayer gold grating were reported with linear polarization rotation at infrared wavelength.[301]

However, most of 3D optical structures are "rigid" solid systems, lacking capability for dynamic tunability and reversibility due to complexity of these transformations. Recently, reconfigurable chiroptical structures have been fabricated with LbL assembly of plasmonic nanoparticles onto a pre-twisted elastic PDMS substrate.[302] It demonstrates reversibly reconfigurable and cyclical chiral optical activity by simply macroscales stretching, ascribing to the transformation of macroscale deformation of flexible substrates to plasmonic nanoparticle nanoscale geometry. Although most of these LbL assembly-based 3D photonic structures are based on the synthetic polymers and nanoparticles, these findings indicate a huge potential for fabricating more sophisticated biopolymer-based 3D photonic materials due to the universality of this strategy.

4.3 Integrating synthetic optical components for hybrid photonics

Integrating optically-active synthetic nanoparticles into the periodical photonic biopolymers can be used to induce surface plasmon resonances (SPR) and fluorescence emission.[204,303] Hybrid photonic crystals with optically active components can possess interesting optical functionalities depending on the types of optical dopants (e.g., quantum dots, metal nanoparticles (NPs), organic dyes) to enable plasmonic, photoluminescent, and surface-enhanced Raman scattering (SERS) phenomena for sensing and lasing. In this section, we discuss recent advances of the integration of synthetic plasmonic/fluorescent nanoparticles within biophotonic structures discussed above.

4.3.1 Plasmonic components with biopolymers

Recent advances in assembly of metal NPs within biopolymers opens a new route to fabricate advanced nanostructures with optical functionality.[304,305,306] For example, silver nanoparticles (AgNPs) were integrated into silk fibroin matrix *via* spin assisted LbL assembly.[307] Dense monolayers of AgNPs reinforced membranes and induced high reflective properties. Moreover, metal NPs that are arranged in photonic structures can confine the light beyond the diffraction limit to render different optical functionalities in a hierarchical arrangement.[308,309,310] Incorporating metal NPs can realize the plasmon-induced coloration, due to the coupling between diffracted light and plasmonic resonances.[311,312] Moreover, plasmon-induced photonic colors can be tuned by the change of the concentration, the shape, and the size of NPs.[313] When metal NPs are added into photonic structure, the plasmonic absorption of metal NPs can selectively enhance the hue and the reflected color with specific wavelengths that are matched to the plasmon resonance peak.[314]

Plasmonic properties can be directly integrated into functional silk photonic crystals by a transfer printing technique.[315][316] Various plasmonic nanostructures were incorporated in both periodic and aperiodic arrays on silk films doped with fluorescent dye (Figure 22a-d).[315] In these hybrid bioplasmonic materials, the fluorescence of doped silk film can be strongly enhanced by designing periodic array with proper periodicities due to resonant coupling between the reflected light and the light emission. Functionalized silk inverse opals doped with AuNPs have been prepared by using a template of PMMA opal structure.[186] The surface plasmon absorption of AuNPs can be significantly enhanced when their absorption is matched to a pseudo-photonic band gap. The cellulose-based photonic crystals have been modified through thermal evaporation of Ag layer onto photonic grating of HPC film.[204] The overall refractive index contrast of this hybrid system can be enhanced due to negative dielectric permittivity of metal coating, which generates vivid colors due to strong electromagnetic field at the metal surface.
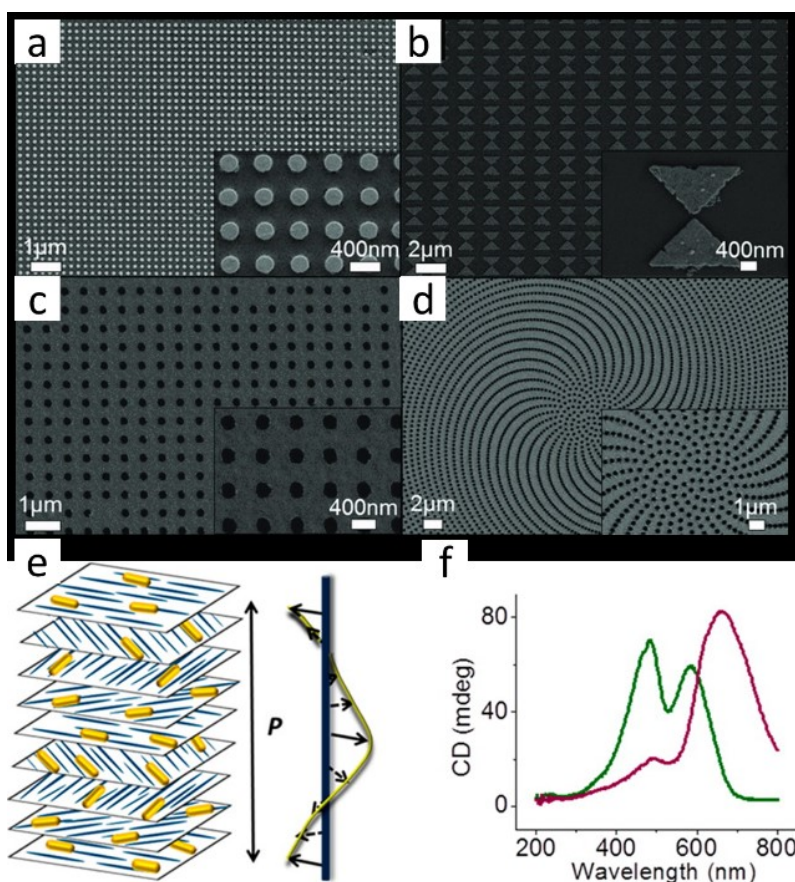
Figure 22. SEM images of plasmonic nanoparticles (a), bow tie (b), nanohole (c), spiral arrays (d) deposited onto doped silk fibroin films by transfer printing method.[315] Reprinted from ref. 315 with permission from Elsevier, copyright 2008. (e) The schematic illustration of cholesteric CNC doped with Au NRs and the CD spectra (f).[303] Reprinted from ref. 303 with permission from American Chemical Society, copyright 2014.

Another remarkable example is chiral plasmonic materials with plasmonic metal NPs integrated into CNC chiral structure.[317] Metal NPs are co-assembled into a chiral structure coupled with the plasmonic nanoparticles generate so-called "chiral plasmonic response". In such a hybrid metal-biopolymer material, the plasmonic nanoparticles assembled in a chiral manner are responsible for enhanced optical circular dichroism over a broad spectral range.   For instance, chiral plasmonic nanostructures were fabricated by incorporating anisotropic Au nanorods (AuNRs) into chiral CNC phase (Figure 22e).[303] The resulting chiral plasmonic films give rise to distinct chiral extinctions with CD peaks corresponding to their transverse and longitudinal SPR of AuNRs, due to the strong interaction between the plasmonic and photonic properties (Figure 22f).[318] In the later study, the fabricated plasmonic core–shell Au/Ag nanocubes within the CNC chiral structures show similar two-peak CD spectra.[317] However, this phenomenon can be related to the reduction of the CD signal because of excessive absorption by the metal nanostructures.

In addition, adding nanoparticles (e.g. silica or silver) in the silk gratings that match the lasing wavelength enables the enhanced light scattering and the laser emission linewidth reduction, resulting in the enhancement of distributed lasing emission.[319] Besides, the co-assembly of silica precursor with cholesteric CNCs allows replicating the CNC organization after selectively removing the CNCs via calcination, which creates new optical functionality in mesoporous photonic structures.[320] In this approach, AgNPs can be further embedded into these mesoporous silica films. The CD spectra of AgNP-doped mesoporous silica films are highly sensitive to the pitch length and silica wall thickness with greatly enhanced CD behavior.[320]

4.3.2 Synthetic photoluminescent components with biopolymers

Highly emissive QDs assembled into photonic crystals provide a powerful platform to construct functional architectures.[321,322,323,324] This combination not only enables them to modulate their emission spectrum due to the photonic bandgap, but also enhances the photoluminescence owing to the coupling between photonic structures and the emission. Significant enhancement of fluorescence has been observed by placing the QDs onto photonic crystals.[52,315,325] For example, the photonic crystals from patterned silk fibroin doped with QDs and fluorescent proteins have been fabricated by using e-beam lithography.[174] The QDs combined with the silk photonic structures showed a five-fold enhanced fluorescence under the illumination of light source with 480 nm (Figure 23a).

The incorporation of luminescent components within photonic chiral structures can generate circularly polarized light (CPL) emission.[326] Transparent and fluorescent cellulose CPL films have been obtained through the assembly of fluorescent molecules into the chiral nematic phase of CNC dispersion.[326] This cellulose CPL film can transform spontaneous emission to right-handed circularly polarized (R-CPL) emission due to the left-handed chiral photonic structure (Figure 23b and c). It is challenging for traditional strategies to generate high CPL emission because of low dissymmetry factor (*g*), quenched luminescence, and unpredictable handedness.[327,328] In this structure, however, R-CPL emission with an enhanced *g* value has been obtained when the emission band is matched to the photonic bandgap of CNC structures, which prevents the propagation of the left-handed CPL light.

In addition, free-standing iridescent and luminescent photonic films with chiral ordering have been fabricated by the co-assembly of CNCs and carbon quantum dots (CQD).[332,329,330,331] Due to the heterogeneous amphiphilic interactions between natural CNC and synthetic CQD components, they co-assemble into highly emissive needle-like "nanocob" nanostructure, which can further form chiral nematic LC phases in concentrated dispersions. After drying, LC phase organizes

into solid-state chiral luminescent film while retaining original long-range chiral ordering with positive ellipticity (Figure 23e).[332]   The resulting film demonstrates an intense iridescent appearance superimposed with significantly enhanced luminescence (Figure 23d).[332]
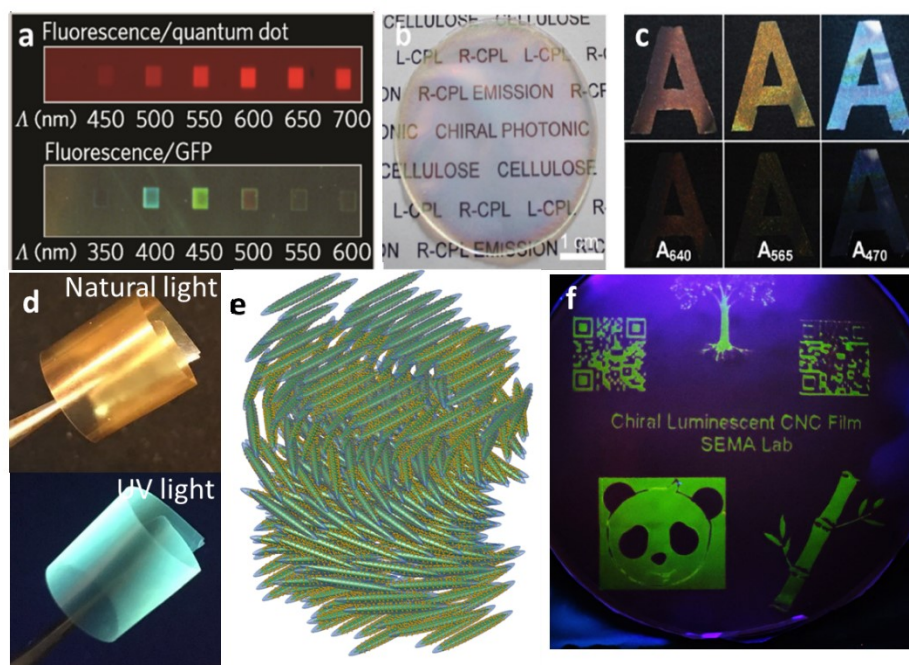

Figure 23. (a) Microscope image of nanostructured silk film doped with QD (upper) and (fluorescent proteins).[174] Reprinted from ref. 174 with permission from Springer Nature, copyright 2014. (b) Photograph of transparent, iridescent, and fluorescent CNC composite film. (c) Photograph of A-shaped CNC composite film through left-handed (upper) and right handed (bottom) polarizing filter.[326] Reprinted from ref. 326 with permission from Wiley, copyright 2018. (d) Photographs of freestanding flexible chiral luminescent CQDs/CNCs film under natural light and UV light. (e) The helicoidal arrangement of CQDs in the chiral CNC matrix. (f) Chiral fluorescent patterns enabled by the ink-jet printing localized pH-initiation.[332] Reprinted from ref. 332 with permission from ACS, copyright 2019.

Because of the integration with left-handed helical organization, spontaneous emission of carbon dots can change to right-handed circularly polarized luminescence. The organization of helical CNC/CQDs superstructures showed right-handed CPL luminescence with high asymmetry value of -0.2. Additionally, large-area chiral luminescent patterns through soft lithographical processing and ink-jet printing can be fabricated with enhanced structural color, polarization-dependent light diffraction and pH-responsive patterned luminescent appearance (Figure 23f).[332]

The chiral organization of CNCs has also been used as a template to prepare other chiral materials, such as containing silica and organo-silica nanoparticles and polymers.[333,334,335,336] The high porosity of chiral host-guest systems could be further explored for the integration with fluorescent NPs. For example, semiconductor CdS QDs were combined with chiral mesoporous silica that is templated by CNC to retain high luminescent photonic structure (Figure 23 d and e).

[337] The resulting iridescent chiral nanocomposites show positive CD ellipticity as well as bright luminescence, indicating QD emission is preserved during photonic structure formation. Although many attempts to realize QDs with chiro-optical activity have been made, it has been still challenging to pre-program the circularly polarized luminescence in biophotonic structures.

4.3.3 Hybrid chiral nematic droplets

Scalable and stable self-organization of optically active components into liquid dispersions has been rarely reported. For example, monitoring the assembly process of CNCs confined by spherical microdroplets allows investigation of dynamic formation of chiral nematic phase of CNC suspensions (Figure 24a).[229]
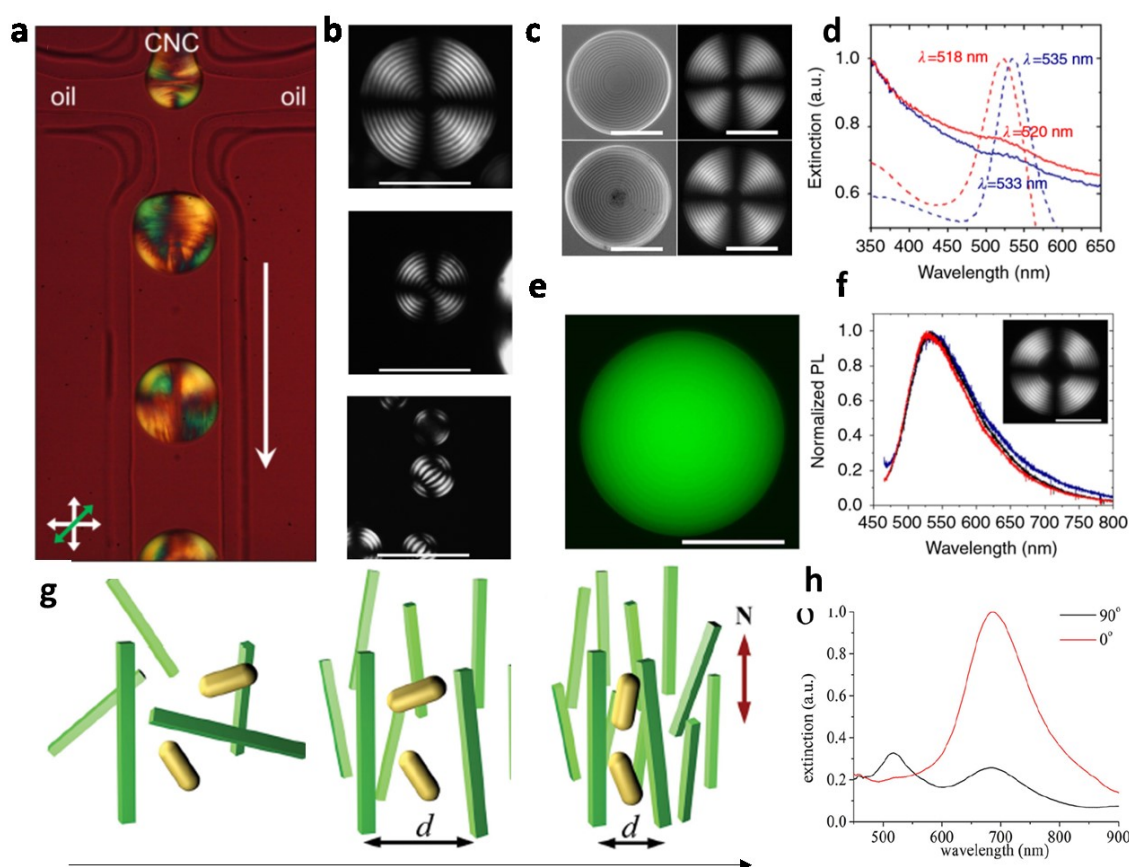

Figure 24. (a) Microfluidic systems to generate the droplet containing chiral nematic CNC phase.[229] Reprinted from ref. 229 with permission from American Chemical Society, copyright 2016. (b) POM images of the cholesteric CNC droplets with different radius. (c) Bright field (left panel) and POM (right panel) images of cholesteric droplets doped with 10 nm(upper) and 50 nm (bottom) AuNPs. Corresponding extinction spectra of AuNPs in cholesteric droplet. (e) Fluorescence image of the cholesteric droplet doped with carbon dots and (f) photoluminescence spectra of core(red) and shell (black) of droplet doped with carbon dot and (black) pristine carbon dot solution.[338] Reprinted from ref. 338 with permission form licensed under CC BY 4.0., copyright 2016. (g) The illustration of phase transition from random orientation to nematic phase for AuNR in a dilute CNC dispersion. (h) The polarization dependent extinction spectra of nematic CNC-AuNR composites.[318] Reprinted from ref. 318 with permission from Wiley, copyright 2014.

This study gives insight to control the assembly processes in cholesteric LCs for integration with optically active components to fabricate biophotonic materials. The organization of optically functional NPs in confined LC droplets can produce unique structures where photonic properties of LCs and NPs are coupled. [338] In this system, confined microdroplets with different sizes can be controlled by emulsification with different NPs (Figure 24b-f). Spherical micro-droplets can act as a template to control functional NPs partitioning in the isotropic core and the chiral nematic shell. The co-assembly of biopolymers and anisotropic NPs can align them as demonstrated by organization of gold nanorods in cholesteric dispersions of CNCs.[318] In this approach, aqueous CNC dispersions show the transition from an isotropic to a nematic phase when the concentration reaches a critical value of ~3 wt.%. Gold nanorods in in LC CNC dispersion are aligned due to entropic and excluded-volume effect while they are randomly oriented in the isotropic phase (Figure 24g, h).

5. Applications of biopolymer photonic structures

Structural colorations are frequently used in nature for camouflaging, protection, mimicking, and attraction. Efficient manipulation of light by the natural organisms, which utilizes various optical phenomena such as absorption, reflection (broadband and selective), emission, scattering, interference, transmission, wave guiding and lensing, facilitates the use the natural materials for a broad range of advanced optics/photonic applications as discussed in this section.

5.1 Light manipulation

Novel photonic materials that enable more efficient light manipulation are important to advance optical applications in various fields including biomedical photonics, optoacoustics, and optomechanics. For instance, in biomedical optics, waveguides and optical transducers from natural materials are designed to directly interact with tissues offering distinct advantages. Recent advances of related biomedical applications, such as photothermal and laser therapy, implantable optical and optoelectronic sensors, and bioimaging, require highly efficient methods to analyze light interactions with cells, tissues, or organs.[339,340,341,342,343]

5.1.1 Photonic light waveguides

Current light guiding venues include glass,[344] polymers,[342,345], and inorganic nanoparticles[346]. While most of these materials have been optimized for efficient light guiding with low losses, they are not ideal for *in vivo* applications owing to their poor biocompatibility and large mechanical mismatch with the biological tissues that can lead to damage of soft tissues. These considerations highlight the unmet need for efficient photonic waveguiding that exhibits long-term biocompatibility

and biodegradability in human tissues. Naturally derived photonic materials can serve as next generation light guiding media. Apart from being biocompatible and biodegradable, these materials exhibit mechanical properties that are compatible with the biological media.

Silk films are optically transparent with transmittance >95% in the range of 350-800 nm.[347] Due to its higher refractive index (1.54) as compared to human tissue (1.44), silk has been employed as *in vivo* photonic light guides which can be fabricated using direct ink printing.[348] *B. mori* silk fibroin was employed as the stabilized concentrated bioink, which was ejected through a glass nozzle into a methanol environment to induce fast crystallization via β-sheet formation. Direct-writing allows the fabrication of straight and wavy fibers within silk pattern up to several centimeters, which showed high uniformity in the dimensions and smoothness.

Recently, it has been demonstrated that low-loss light guiding fiber can be fabricated based on spider silk.[349] Compared to that made from *B. mori* silkworm, the spider silk optical waveguides exhibited a smoother surface and higher refractive index (Figure 25a). When light propagates inside the silkworm optical waveguide, it scatters strongly and leaks from the fibers. However, light can be seen only at the terminal of the spider silk fiber, with minimal leaking from the waveguide walls. Correspondingly, these fibers showed low optical loss with attenuation coefficient of 0.8 ± 0.1 dB/cm in air, which is significantly lower than that made by regenerated silkworm silk (1.7 ± 0.1 dB/cm and 3.1 ± 0.4 dB/cm, respectively). The higher β-sheet content and refractive index of the recombinant spider silk might be responsible for this difference.

Next, 1D micro/nanostructures (rods, wires, and belts) comprised of peptides (such as diphenylalanine and tri-phenylalanine) have been explored as passive and active light waveguides.[350,351,352,353] For example, peptide-based nanowires have been obtained through the self-assembly of diphenylalanine in the aqueous phase.[351] More recently, large-area light guiding structures have been fabricated using tri-phenylalanine peptides tends to assemble across large area wafers with uniform dimensions (Figure 25b,c). [355]

This biomaterial exhibited several intrinsic advantages such as optical transparency over wide wavelength range, nonlinear optical properties, as well as the ability to actively and passively guide light. The refractive index within 400-800 nm was measured to be 1.58-1.66, highlighting the potential application of these materials in *in vivo* bio-optical chips.[354] Passive waveguiding was demonstrated by its ability to guide normally incident light through reflection, refraction, and diffraction (Figure 25d).
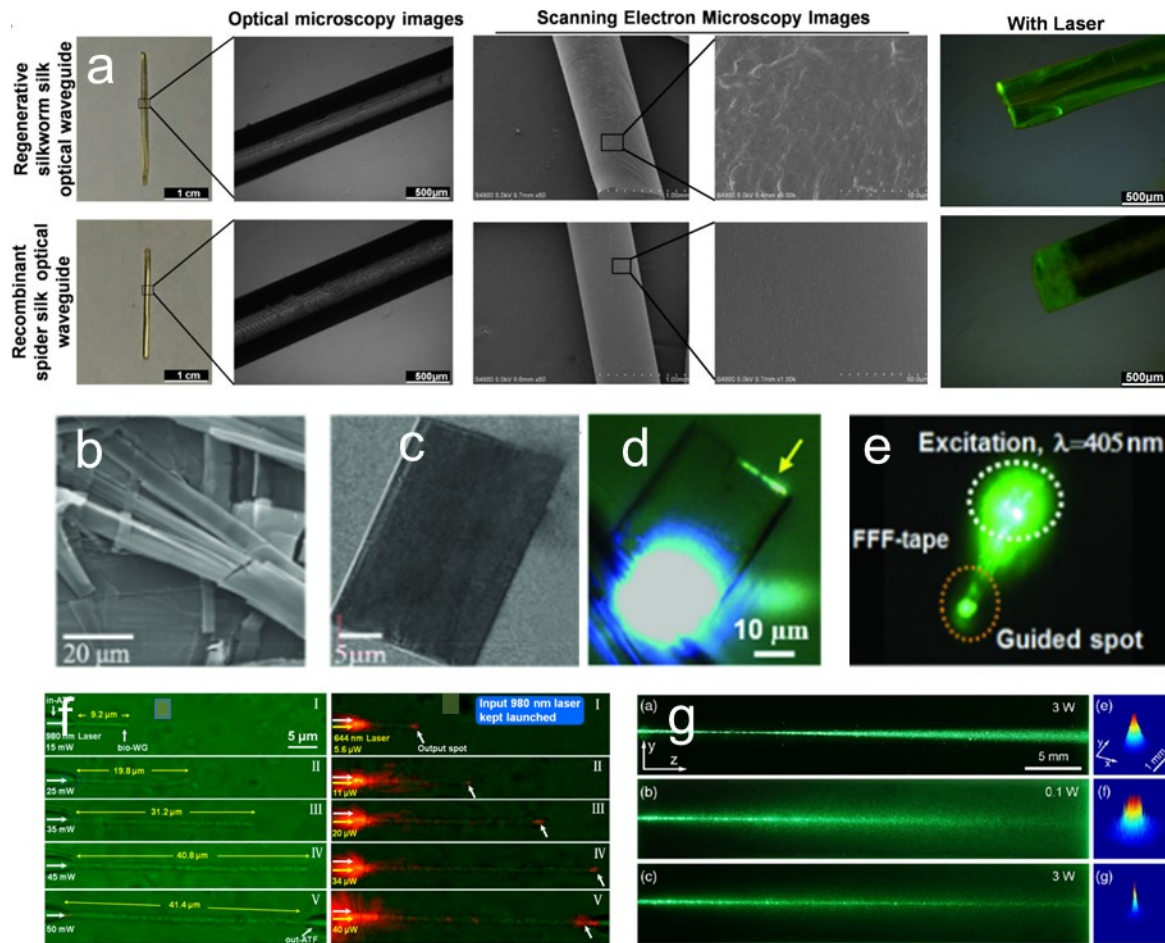
Figure 25. (a) Images of optical waveguides made by recombinant spider silk (bottom) and regenerative silkworm silk (top) taken with camera, optical microscopy, and SEM and their laser propagation properties.[349] Reprinted from ref. 349 with permission from American Chemical Society, copyright 2017. (b) SEM image of self-assembled elongated tri-phenylalanine (FFF) tapes. FFF tapes in such a distribution have random orientation and inhomogeneous thickness, length, and width, and thus are inappropriate for integrated photonic devices. (c) SEM image of FFF planar wafer of dimensions 15 µm × 34 µm × 1.4 µm. (d) Passive optical waveguiding in 2D FFF wafer. (e) Active optical waveguiding in 2D FFF wafer.[355] Reprinted from ref. 355 with permission from Wiley, copyright 2018. (f) Optical microscope images of formed *E. coli* bio-waveguides with various lengths and formed bio-waveguides with 644 nm red-light transmitted. White slanted arrows indicate the output spots of the red light.[356] Reprinted from ref. 356 with permission from American Chemical Society, copyright 2013. (g) Nonlinear self-trapping of light through cyanobacteria in seawater.[357] Reprinted from ref. 357 with permission from American Physical Society, copyright 2013.

Apart from the passive capability, one of its unique advantages is the ability to switch to an active mode, which involves the optical absorption of the incident light followed by light emission. This transformation can be achieved by heat trigger, which induced formation of β-sheet, leading to red-shift of absorption wavelength (Figure 25e). Even individual biological species such as *Escherichia coli (E. coli)* can be directly utilized as light guiding media.[356] This photonic waveguide was fabricated by aligning *E. coli* into different lengths using a tapered optical fiber (ATF) by

launching a 980 nm light with various power (Figure 25f). The *E. coli* bacteria were gradually trapped along the laser beam due to the optical gradient force.[358,359] The photonic waveguide shows good light propagation performance. More recently, the nonlinear transmission of light through *Synechococcus* cyanobacteria was demonstrated.[357] When the illuminating laser power is low, light is linearly scattered by the biological suspensions. However, at a high laser power, light is able to propagate over a long distance. They showed that this phenomenon is due to the alignment of bacteria at high power, which acted as an efficient light guiding media (Figure 25g).

Overall, *in vivo* biomedical applications critically depend on the ability to deliver light locally at the desired site. Considering the limited penetration of light into the biological tissues and poor efficiency of the implantable light sources, biocompatible and implantable waveguides are attractive for the abovementioned applications. While it is difficult to overcome the intrinsic optical loss of these biomaterials, the loss emanating from the parasitic scattering can be reduced, which should certainly be one of the goals of the future efforts. Ability to control the biodegradation of the waveguides at the end of their desired function through either an external trigger or prior programming is also important for biomedical applications.

5.1.2 Bio-enabled diffraction

Complex 3D structures can act as diffractive optical elements such as (micro-)lens to focus light into a confined region. To date, only several examples of these elements comprised of natural polymers have been demonstrated as well.[14,360,361,362] Harnessing the facile processability of silk and soft lithography, the fabrication of optical components, such as diffraction gratings or microlens arrays, has been demonstrated.[14] Silk films with a thickness of few tens of microns exhibited near 100% optical transparency over the entire visible spectrum making them excellent candidates for the diffractive elements. Silk elements have been used for the incorporation of biomolecules such as hemoglobin and peroxidases, enabling bio-active optical elements as well as media for stabilizing bioactive compounds.[363,364,365]

Microspheres and microcylinders can focus incident light beyond the diffraction limit, a phenomenon known as a "photonic nanojet" that enables a form of super-resolution optical microscopy.[366] A photonic nanojet is a narrow, high-intensity electromagnetic beam that propagates into the medium illuminated from lossless light source.[367] Recently, a micro spindle with epoxy-knot-decorated spider silk have been reported, to exhibit photonic nanojet effect.[368] In this work, a single spider silk fiber was obtained from *pholcus phalangioides* with a diameter of 2 μm (Figure 26a). The laser beam was focused on the left side of the spindle knot convex, and photonic nanojet was observed (Figure 26d). The authors demonstrated that it is possible to

realize different photonic nanojets with distinct shapes through changing the knot dimensions.
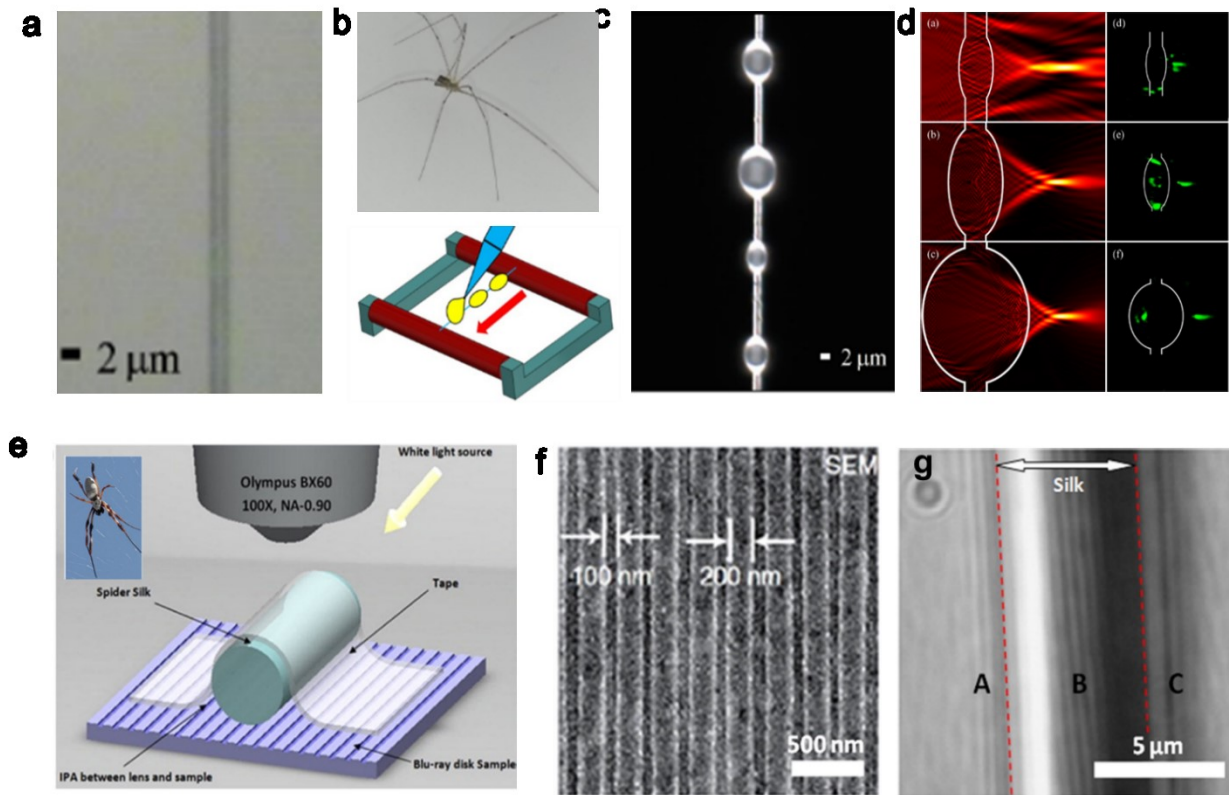

Figure 26. (a) Microphotograph of a bare spider silk fiber. (b) Schematic showing the process of decorating the spider silk fiber using adhesive UV cure. (c) Microphotograph of spindle knots decorated spider silk. (d) Simulation of normalized power flow patterns for the spindle knots at diameter of (a) d=3 μm, (b) d=6 μm, and (c) d=10 μm. Experimental images showing the focused light from the spindle knots at (d) d=3 μm, (e) d=6 μm, and (f) d=10 μm.[368] Reprinted from ref. 368 with permission from Optical Society, copyright 2019. (e) Schematic showing reflection mode silk biosuperlens imaging. The spider silk was placed directly on top of the sample surface by using a soft tape. The gaps between silk and sample were filled with IPA which improves imaging contrast. The silk lens collects the underlying near-field object information and projects a magnified virtual image into a conventional objective lens (100×, NA:0.9). (f, g) The integrated surface pattern is magnified by the spider silk. The 100 nm channels (f; SEM image) are resolved by the spider silk superlens (g; optical nanoscope image).[369] Reprinted from ref. 369 with permission from American Chemical Society, copyright 2016.

Furthermore, spider silk has been shown to serve as materials for a super-resolution lens (superlens) that can focus the light beyond the diffraction limit (Figure 26e).[369] Conformal contact between the nanostructures and the silk fiber is found to be critical for achieving the near-field nanoscale resolution. This proximity enables the conversion of the surface-bound evanescent waves into propagating waves, which can be detected in the far-field regime.[370,371] Silk superlens demonstrated distinctive advantages such as simplicity, biocompatibility, and ready availability for use in biomedical research. These silk superlenses can resolve features of about 100 nm (Figure 26f, g).

In another example, freely standing silk microprisms have been demonstrated, which can potentially serve as an optical platform for reflecting forward-scattered photons through tissue for improved imaging of malignancies.[372] The micropatterned silk film was shown to significantly increase the reflected light that helps to enhance intrinsic sensitivity. Overall, diffractive optical elements based on natural materials provide new avenues for high-resolution bioimaging, which can potentially be employed for light harvesting, spectral signal enhancing, and optical sensing.

5.1.3 Photonic structural color

In contrast to pigment-based coloration, the astonishing structural colors observed in organized natural and biological materials is the consequence of interference, diffraction or the selective reflection of light from modulated distribution of the refractive index. The camouflaging and optical tunability in various biological organisms such as cephalopods, chameleons, *paradise whiptail*, *hercules beetles*, *blue damselfish* serve as great source of inspiration for the design of hybrid materials that exhibit responsive tunable color. Among underlying phenomena are intense iridescence,[373] angle-independent coloration,[374] ultra-blackness,[375] and ultra-whiteness[69].

For example, bright colors of bird feathers are produced by nanoscale structures of biological materials (keratin and melanin) and organized structures that periodically modulate the refractive index.[376,377,378] Male peacock feathers exhibit brilliant iridescence, diversified coloration, and intricate patterns due to the presence of nanoscale periodic structures of melanin rods arranged in the melanin layers. Changes in the periodicity of the photonic crystal structure shift the partial photonic bandgaps and secondary overtones, which eventually leads to the formation of diversified colors with additive and mixed coloration. These observations provide inspiration to the design of novel optical synthetic materials and devices by either enhancing the refractive index contrast or increasing the relative amount of low refractive index materials. [379]

Extensive efforts have been dedicated for mimicking these vivid natural structural colors by design of complex periodical nanostructures. [225,296,380] For example, structurally colored films comprised of polyelectrolyte/clay and colloidal silica/cellulose nanocrystals layers were prepared using LbL assembly.[296] These films mimic the structure of elytra of a *C. rajah* beetle and they are comprised of alternating low and high refractive index layers with controlled thicknesses. With increasing incidence angle, the film exhibited brilliant iridescence due to the blue shift in the reflected wavelength. In another example, mimicking the bi-structural color reflection of creatures such as *Papilio* butterflies, was conducted with silk-fibroin photonic crystals.[380] These structures exhibit two partial photonic bandgaps, thus, causing bi-structural colors appearance from UV/visible to visible/IR region. In addition, multicolored chiral nematic cellulose films were produced by the

slow evaporation of cellulose nanocrystals suspensions on polystyrene substrates, which shows left-handed helicoidal structures. The bioinspired film exhibited distinct colored domains with sizes ranging from a few micrometers to several tens of micrometers.[223]

5.2 Photonic-enabled physical/chemical sensing

Next, photonic structures are extensively investigated for prospective physical, chemical and biological sensing. Design and realization of novel materials that sense various changes in the environment *a.k.a.* external stimuli such as temperature, light, chemical ambient, electrical field, magnetic field and dynamically change their organization are not only an exciting fundamental challenge but also highly attractive for a wide range of applications including mechanical and optical sensors, energy-saving smart windows, transparent flexible displays, telecommunications, and tunable lasing. [381 , 382] Natural materials can be harnessed and exploited to engineer responsive optical materials, which exhibit distinct changes in optical properties with external stimuli with several recent examples summarized below.

5.2.1 Pressure sensors

Mapping of mechanical pressure distribution was demonstrated with HPC materials, which exhibit a structure similar to natural cellulose with hydroxyl groups of the glucose being hydroxypropylated.[231] This naturally derived material can form a cholesteric LC phase, and undergoes structural changes in response to external stimuli such as stress, temperature, and light, resulting in tunable reflective colors. Based upon this phenomena, biocompatible strain responsive photonic sensors were fabricated with an aqueous LC phase.[233] The HPC strain sensor showed a color change (from yellow to blue) upon applying compression, due to the change in the pitch length (Figure 27 a,b). Recently, a large-area HPC photonic material was fabricated using a roll-to-roll method, continuous coating and encapsulation.[18] The HPC was fabricated into photonic films under the low-pressure roll-to-roll process, resulting in large-area uniform chiral films. As pressure increased, the hue value increased a blue shift in the reflectance wavelength that enabled real-time mapping of the pressure distribution with spatial resolution of less than 1 cm.

In another study, a CNC stretchable sensor was fabricated with the reversible unwinding of chiral CNCs embedded in an elastomer under large deformation of 900% (Figure 27c).[16] Stretching the CNC/elastomer composites unwinds the chiral organization of the CNCs in uniform alignment along the stretching direction. As a result, the deformed materials show vivid birefringence, which reversibly changes when the elastomer returns to its original shape (Figure 27d). In their follow

up study, the authors demonstrated pressure-responsive chiral photonic aerogels through freeze drying the CNC LC hydrogels.[383] The applied pressure can transform the 3D porous structure of the aerogel into a compressed material with the structural color changes.
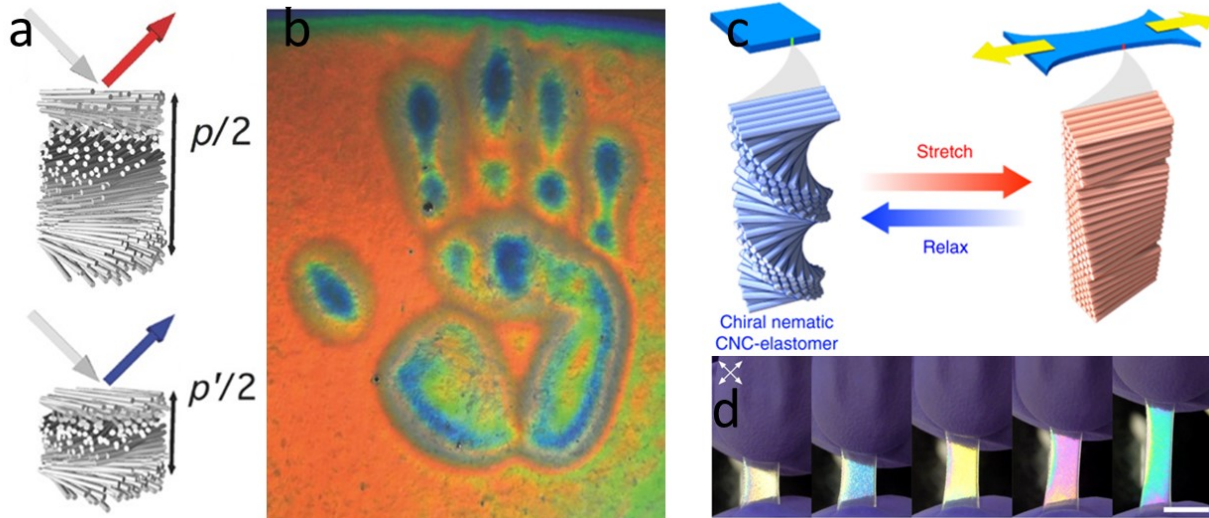

Figure 27. (a) Schematic illustration of the chiral HPC touch sensor based on the change in the pitch length. (b) A handprint recorded on the HPC sensor.[233] Reprinted from ref. 233 with permission from Wiley, copyright 2016. (c) Schematic illustration of the stretchable CNC sensor mechanism. (d) Photographs of CNC stretching sensor as viewed under crossed polarizers.[16] Reprinted from ref. 16 with permission from license under CC BY 4.0, copyright 2019.

Overall, these studies demonstrated the utilization of natural biopolymers in configuring micro and macroscale structures that respond to physical cues such as mechanical stresses. These concepts can be extended to biopolymer-based photonic materials, which could broaden the dynamic range of the mechanical sensors.

5.2.2 Temperature, humidity, and chemical sensors

One of the major hallmarks of biophotonic systems is their ability to dynamically respond and reversibly reconfigure in response to external stimuli.[384,385,386] One of the strategies used by biological organisms is the combination of multiple photonic elements to achieve multi-parametric response, greater dynamic range, and a finer degree of control of photonic properties.[239,387,388] These considerations have inspired the use of natural polymers in the design of chemically-responsive photonic structures.

Recently, a biomimetic photonic structure based on CNCs that can reflect both left circularly polarized light (LCP) and right circularly polarized light (RCP) has been demonstrated.[389] The biological example, *Plusiotis resplendens*, has a ~1.8 µm thick unidirectional layer, which is

embedded between two layers of anticlockwise helicoidal architectures (left-handed cholesteric layers), which acted as a half-wave retardation plate (Figure 28f).[390] Inspired by the insect, researchers have fabricated various photonic materials to mimic the naturally built architectures. The iridescent CNC films that can simultaneously reflect LCP and RCP have been fabricated.[389] This photonic structure was fabricated by impregnating iridescent CNC films with 4-cyano-4′-pentylbiphenyl (5CB) nematic LC phase, which filled into the micro gaps between the two left cholesteric domains of CNC materials (with different pitch, Ch'1 and Ch'2) (Figure 28a). The resulting nanocomposite film exhibited the ability to reflect LCP (green light with λ=518 nm) and RCP (orange-red light with λ=610 nm) (Figure 28b-d). This ability can be explained by the close match of the phase difference between the ordinary and extraordinary rays to 180°. In this design, the LC layer acted as a λ/2 retardation plate and changed the transmitted right-handed circularly polarized light into left-handed one. The converted LCP light was then selectively reflected (λ~600 nm) by the bottom chiral layer with a different pitch as compared to the top layer (Figure 28e).

On its way back, this reflected left-handed polarized light is in turn converted to right-handed light while passing the retardation layer and is finally transmitted through the top chiral layer. The wavelength of the reflected RCP and LCP can be tuned by changing the birefringence Δn through temperature changes or stimulation of electric field. This ability renders the material to serve as a good candidate for thermo(electro)-chromic effects. The interfacial LC layer changed from the nematic to the isotropic state at an elevated temperature, resulting in the right circularly polarized light to become colorless while the image of the left circularly polarized light persisted with an intense reddish color with quick response time (milliseconds). Similar chromic changes can be induced by the external electric field.   Indeed, Ribeiro et al. reported thermal and electrical responsive photonic composite films through penetrating nematic-induced molecules, 4 -(hexyloxy)-4-biphenylcarbonitrile (HOBC) into the chiral nematic phase of CNC dispersions.[391] This unique combination of two chiral components can significantly enhance the structural integrity of the resulting chiral organization with reversible thermal and conductive response of the LC phase as caused by crystal-nematic transition and nematic-isotropic transitions.

In addition, CNC-based photonic nanocomposites have been fabricated as humidity responsive chromic actuators.[392] In these materials, uniaxially oriented polyamide-6 layer was sandwiched between two left-handed chiral structures, which consisted of CNC/polyethylene glycol diacrylate (PEGDA) (Figure 28g). In this case, polyamide-6 layer acted as a λ/2 retardation plate, which led to the hyper-reflection of the film. This film showed dual response as well as colorimetric change with increased humidity (Figure 28h,j).   Under increased surrounding moisture, the

nanocomposite film showed deformation due to the asymmetric swelling of the stimulated side; the helical pitch on the stimulated side increased, resulting in a wavelength red shift (Figure 28h, i). In the final stage, the film became flat again due to the diffusion of the water to the non-stimulated side. For example, the CNC films show fast color change from blue to red in response to the humidity because the intercalation of water molecules results in the increased chiral pitch length.[239]
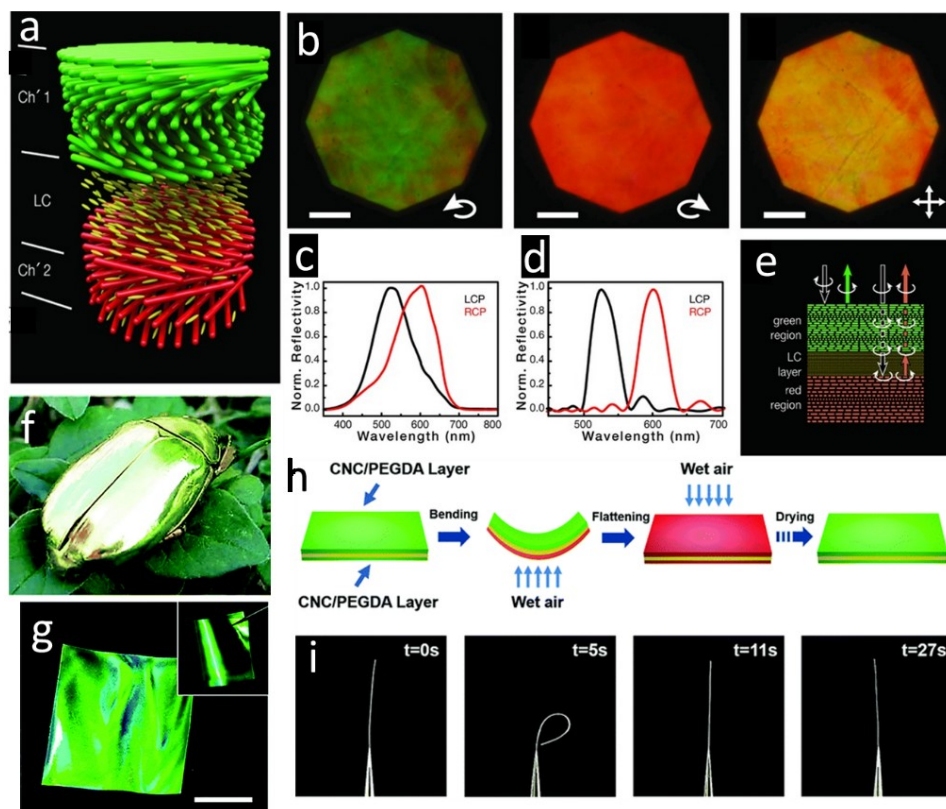

Figure 28. (a) The gap filled with the anisotropic layer sandwiched between the two CNC left cholesteric domains (Ch'1 and Ch'2). (b) POM images of the sandwiched film with left-hand polarizer, right-hand polarizer, and crossed polarizer, scale bar: 50 μm. Spectra from LCP and RCP channels (c) and simulated reflectance spectra using Berreman's method (d).[389] Reprinted from ref. 389 with permission from Wiley, copyright 2017. (f and g) Photograph of the jewel beetle *Chrysina resplendens* and the hyper-reflective CNC-based nanocomposite film with a sandwich structure (scale bars, 20 mm). (h) Vapor-based actuation in the sandwich structures. (i) The deformation processes of the sandwich structured film.[392] Reprinted from ref. 392 with permission from Royal Society of Chemistry, copyright 2016.

Responsive photonic structures can act as a chemically responsive material when exposed to variable environmental stimuli. Generally, this type of the responsive behavior originates from the photonic lattice changes caused by the changing chemical interactions and their effects on spatial dimensions and state of the elements. For instance, inverse opals change their structural color with a change of the solvent quality.[393,394] Recently, photonic CNC hydrogels have been

prepared with the addition of a wide range of monomers and crosslinkers.[335] As-formed CNC hydrogels' reflected color can be tuned by changing CNC concentration or the ionic strength of the mixture through adding sodium chloride, which leads to a decrease in the pitch length of the chiral nematic phase. These LC hydrogels are responsive to surrounding pH and solvent quality. An immediate red-shift in the light reflectance was observed when the CNC hydrogel was immersed in water. In contrast, the hydrated CNC hydrogel underwent a blue shift due to contraction when it was subsequently immersed in ethanol. The reflected color of the hydrogel can be reversibly controlled by immersion into various media over multiple cycles with no obvious degradation. The response rate was shown to be controlled by the hydrogel crosslinking degree. This property can be further harnessed to produce patterned materials, with masked regions swelling at higher rates and, thus, producing a patterned image.

Apart from cellulose-based structures, other natural polymers have been employed to form photonic responsive materials for physical and chemical sensing. [395] The growth of living cardiomyocyte tissues into methacrylated gelatin (GelMA) inverse opal template lead to structural color hydrogels that can response to electric stimulation.[396] A biomimetic infrared camouflage coating has been demonstrated based on self-assembly of a water-soluble *Loligo (Doryteuthis) pealeii* reflectin isoform into a thin film.[397] The reflection wavelength of the reflectin film showed a gradual red shift, to near-infrared range, with the increase in the film thickness. When exposed to acidic vapor, the reflectance spectrum of the RFA1 film exhibited a new peak at around 1200 nm, correlating to the film thickness of ~394 nm. The significant increase in the thickness of the film under acidic condition was explained by the swelling of the closely packed reflectin nanoparticles. This work demonstrated a chemo-responsive material with the largest reflectance window that extends to ~1200 nm, matching infrared imaging needs.

5.3 Photonic biosensors

Detection of biological fluids is of fundamental importance to biomedical research and clinical diagnostics to monitor complex, non-linear, biochemical systems. Photonic structures have been shown to be a promising optical platform for biosensing applications. Various bioassays have been integrated with photonic structures to attain higher sensitivity, real-time monitoring, label-free detection[398], and biocompatibility with inexpensive setup[306]. Moreover, when interfaced with other photonic platforms can exhibit stronger local electromagnetic field enhancement, which can benefit a variety of biosensing applications.[399]

5.3.1 Fluorescence biosensors

In recent study, autofluorescence of silk fibroin has been harnessed to realize vitamin B_{12} sensing platform.[400] When excited by 290 nm light, aqueous solutions of *Bombyx mori* silk fibroin exhibited fluorescence emission at around 350 nm.   The intrinsic photoluminescence of silk fibroin originates from the indole chromophore of tryptophan.[401] The authors found that the emission intensity of silk decreased with the addition of vitamin B_{12} (Figure 29a). The emission intensity progressively decreased with an increase in the vitamin B_{12} concentration, which indicates quenching of silk photoluminescence in the presence of vitamin $B_{12.}$ This quenching effect was related to the efficient energy transfer process between the energy donor (silk fibroin) and the acceptor (vitamin B_{12}) due to the overlap between the emission of silk fibroin and the absorption of vitamin B_{12} and Coulombic interactions between vitamin B_{12} and silk fibroin (Figure 29b). The authors showed that the simple silk fibroin platform can detect vitamin B_{12} down to 3 ng/µL in a label-free manner. Presence of other biological components such as serum proteins and amino acids caused minimal quenching, indicating a good selectivity of the vitamin B_{12} sensing platform.

As mentioned above, photonic structures have also been utilized for enhancing the emission from fluorophores employed as signal reporters.[402,403] Fluorescence-based technologies are widely utilized for the detection of various soluble and cell-bound biomolecules.   However, feeble fluorescence signal and the associated low signal-to-noise ratio remain persistent challenges in meeting the ever-increasing demand to image, detect, and quantify biological entities of low abundance. It has been demonstrated that periodic cellulose structures, termed as a "photonic pseudopaper", can be utilized as a highly sensitive platform for enzyme-linked immunosorbent assay due to the enhanced emission of natural fluorophores (Figure 29c).[402]

The photonic pseudopaper was fabricated by drop casting nitrocellulose solution into a template comprised of close-packed SiO_2 nanoparticles. After the removal of the SiO_2 nanoparticles, the photonic cellulose structures contained ordered interconnected pores allowing for the transport of biomolecules into the matrix. The photonic pseudopaper exhibited tunable colors with reflectance peaks ranging from 400-600 nm, as achieved by changing the size of the silica nanoparticles of the template (Figure 29d). These periodic structures increase the fluorophore-light interaction due to the slow-photon effect[404], leading to enhanced emission. The photonic pseudopaper further served as a platform for sandwich immunoassay, where the presence, abundance, and binding of the target analyte reflected in the fluorophores generated.

Furthermore, a digital nucleic acid assay based on the formation of micro-droplet array on the photonic pseudopaper has been demonstrated by the same group (Figure 29e).[403] In a digital nucleic acid assay (e.g. with loop-mediated isothermal amplification (LAMP)), samples are first

diluted and evenly divided into large partitions, where each partition contains either one or two analytes, or no analyte at all. After the reaction, the amount of partitions containing positive signals can be detected, which represents the total concentration of the target analytes. These micropatterned photonic arrays served as holders for micro-size reactions after hydrophilical modification to realize photonic microwells. After casting the aqueous sample on the photonic array, discrete microdroplets were formed by preferential wetting on non-patterned photonic nitrocellulose areas. Additionally, this micropatterned photonic pseudopaper enhances the fluorescence signal generated within the micro-chambers due to the appropriate location between the photonic stopband and the fluorophore emission, leading to high sensitivity and a shortened detection time (Figure 29f).
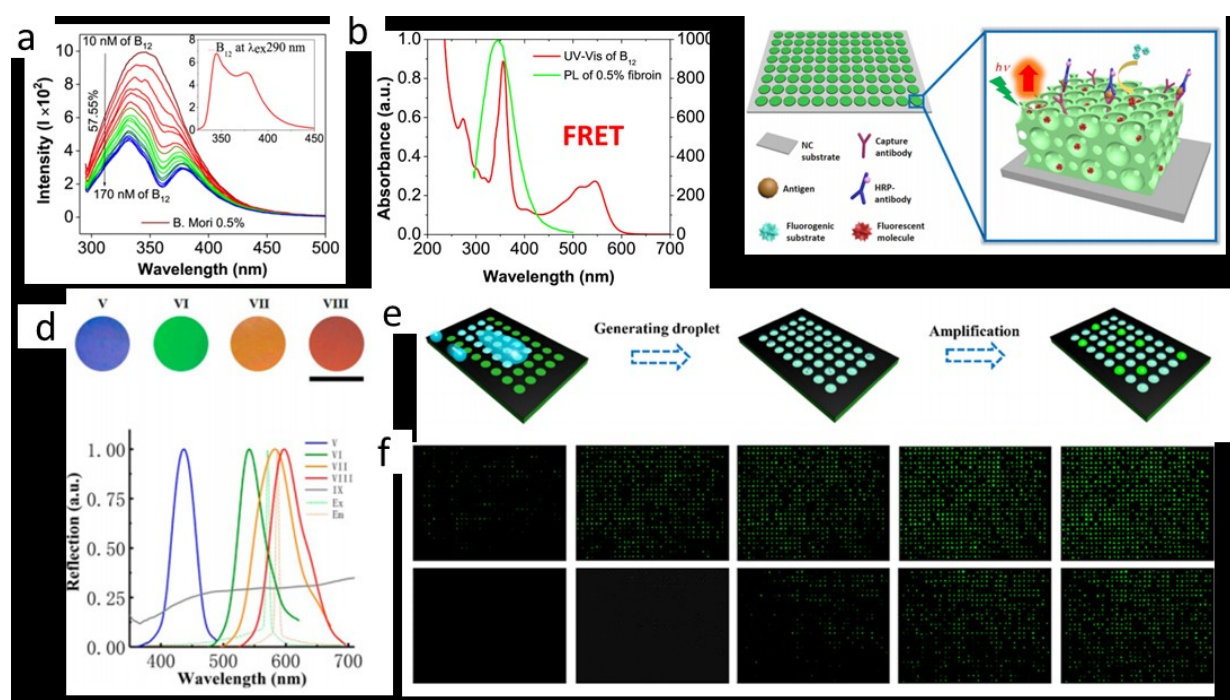

Figure 29. (a) Photoluminescence of *B. mori* silk fibroin aqueous solution in the presence of vitamin B_{12} (λ_{exc} is 290 nm). (b) Overlap between the fluorescence emission of silk fibroin and the absorbance of vitamin B_{12} indicating efficient FRET between the donor and the acceptor.[400] Reprinted from ref. 400 with permission from Elsevier, copyright 2018. (c) Photonic nitrocellulose enhanced fluorescence of enzyme linked immunosorbent assay. (d) Photonic nitrocellulose showing tunable colors and reflectance spectra.[402] Reprinted from ref. 402 with permission from American Chemical Society, copyright 2017. (e) Schematic showing the digital nucleic acid assay. (f) Fluorescence micrographs of the substrate after completion of the digital nucleic acid assays in the microdroplet arrays with (top row) and without (bottom row) photonic nitrocellulose.[403] Reprinted from ref. 403 with permission from American Chemical Society, copyright 2018.

5.3.2 Biosensors based on the reflective structures

Photonic colloidal crystals based on PDA/SiO₂ nanoparticles can serve as a signal barcode for potential applications in suspension arrays.[397] In a typical microbead suspension array, the

intrinsic characteristic signal from the microbead competes with the fluorescence signal from the biomolecular reporter bound on the microbeads. The intrinsic signal of the microbeads serves as the barcode, representing different target analytes, therefore enabling high-throughput multiplexed detection from a small sample volume. Fluorescence signal from the microbeads is employed as one of the most common barcodes.

The photonic structure is an attractive alternative as a "photonic barcode" due to the stable reflection characteristics and low fluorescent interference with the target signal.[405,406,407,408,409] PDA coated SiO_2 nanoparticles were assembled into micro-spherical colloids after droplet-based microfluidic synthesis.[410] Due to the broad PDA absorption, the PDA/SiO_2 photonic structures exhibited high color saturation and narrower half-peak width of the reflection as compared to photonic structures from bare SiO_2 microbeads. Moreover, these photonic structure showed much higher mechanical strength under ultrasound treatment. Multiple fluoroimmunoassays were then performed on the PDA/SiO_2 photonic microbeads, which exhibited good sensitivity and specificity. Further optimization of the photonic properties of the beads can result in fluorescence enhancement, which might improve the bioassay sensitivity.

5.3.3 Surface enhanced Raman scattering for SERS biosensors

Photonic structures can serve as a versatile platform for the integration with plasmonic nanostructures to generate SERS from analytes in close proximity to plasmonic nanostructures.[411,412,413] SERS has been shown to enable the rapid and efficient detection of trace amounts of biological analytes such as proteins, lipids, nucleic acids, pigments, and metabolites.[414,415,416,417,418] The highly ordered photonic structures provide multiple advantages when combined with plasmonic nanostructures: 1) they serve as ordered 3D templates for the fabrication of hybrid plasmonic-photonic structures with complimentary optical properties, allowing for the generation of high-density hotspots to increase the detection sensitivity; 2) photonic structures from natural materials provide rich chemical functionality to interface with plasmonic nanostructures or to grow the nanostructures *in situ* and render chemical selectivity; 3) the close packed large-area photonic structures allow for the generation of active hotspots with high uniformity.

Recently, gyroid-structured SERS substrates using wing scales of the butterfly *Callophrys rubi* as soft templates have been demonstrated.[419] *Callophrys rubi* exhibited a bright green color, which is due to the photonic structure of the gyroid photonic crystals (unit cell size of 360 nm). These three-dimensional photonic structures are usually difficult to achieve using conventional photolithography methods. Plasmonic nanogaps were formed by growing a thin layer of gold on

the gyroid photonic crystals to achieve various volume ratios via proper control in the metal deposition time. The density of the plasmonic nanogaps in the matrix was optimized to achieve ultrasensitive SERS detection of a variety of chemical analytes such as crystal violet and bis(2-ethylhexyl) phthalate with a low limit of detection reaching 1 fM.

Gold coated butterfly wings have been shown to be effective as the SERS substrate for the detection of cancer biomarker, carcinoembryonic antigen (CEA, ~180KDa protein) (Figure 30a).[420] A thin layer of gold (~40-70 nm) was uniformly grown on the wings of *E. mulciber* to replicate the hierarchical micro-structures of *E. mulciber* wing scale, leading to a higher density of the electromagnetic hotspots as compared to planar SERS substrate. The authors showed that Au coated photonic substrate exhibited good signal uniformity and reproducibility, which is critical for reliable detection of cancer biomarkers. CEA was then specifically captured by the antibody immobilized on the Au photonic substrate and subsequently probed by Rhodamine G-tagged aptamer acting as a Raman reporter. The authors showed a CEA detection limit of ~10 ng/ml, which is an order of magnitude lower than that obtained from a commercial SERS substrate.

Cellulose based photonic/plasmonic composite films can serve as a flexible and sensitive SERS substrate (Figure 30b).[421] A photonic crystal template consists of PS nanospheres, which were assembled into hexagonal close packed array based on the gas-liquid interface method.[422] The template was subsequently immersed in a mixture of silver nanoparticles and cellulose solution and followed by etching the template by methylbenzene, leaving a well-ordered inverse opal photonic/plasmonic structure. Methylcellulose and carboxymethyl celluloses were employed in this study due to their high stability in organic solvents. Using HPC as a supporting material, photonic/plasmonic structures have been fabricated using a soft nanoimprinting lithography.[204] To introduce strong electromagnetic field enhancement, a thin layer of silver (50 nm) was deposited on the top of HPC membranes and employed as a SERS substrate. To test the SERS performance, the sample was exposed to thiophenol, a Raman reporter. Notably, the SERS signal was significantly higher between the metallic pillars when illuminated with 532 nm laser. On the other hand, the SERS signal mainly originated at the pillar area when excited at 633 nm laser.

This SERS-based sensing is mainly attributed to the difference in the spatial distribution of the electric field under different excitation wavelengths. The rich chemical functionality enables facile surface modification of the micro and nanostructures based on natural materials, which is important for immobilization of the highly selective bio-recognition elements and passivation of

the surface to minimize overwhelming non-specific binding and fast clogging of the sensing elements.
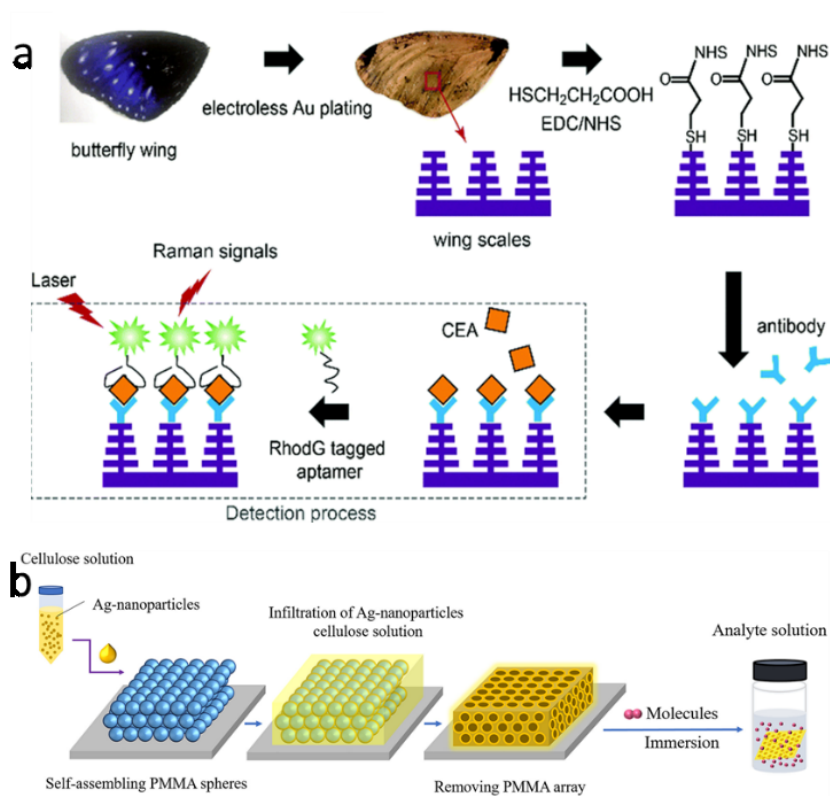

Figure 30. (a) Schematic illustration of CEA detection on Au butterfly wings based on the photonic SERS structure.[420] Reprinted from ref. 420 with permission from Royal Society of Chemistry, copyright 2017. (b) Ag-nanoparticles modified photonic flexible cellulose film for SERS detection.[421] Reprinted from ref. 421 with permission from Elsevier, copyright 2019.

In the context of implantable devices, the biodegradability of these materials obviates the need to surgically explant the devices at the end of their functional life. Optimizing the micro and nanostructures allows to tune the optical behavior in IR windows and the fabrication of biosensors that can continuously monitor important bioanalytes and their deployment *in vivo*.

5.4 Energy harvesting with biophotonic structures

Natural photosynthesis captures of sunlight by various biological systems such as plants and cyanobacteria followed by the efficient conversion of CO_2 into organic molecules of sugars and carbohydrates. [423]   Among the series of photo-electrochemical processes involved in the photosynthesis, light harvesting is the most efficient process that drives and induces the subsequent photochemical reactions. In terms of efficiency, light harvesting occurs at greater than light 90% conversion with a nearly perfect quantum yield.[424] Light harvesting machinery of general photosynthetic systems, different types of light-absorbing chromophores and pigment-

protein complexes, energy transfer processes/mechanisms, and adaptations/mechanisms used to mitigate the effects of high intensity light exposure have been extensively investigated.[425,426,427] In this section, we will highlight a few recent examples for light harvesting.

The redox activity of quinones, organic compounds that contain two adjacent carbonyl groups in an unsaturated six-member ring structure, is widely utilized in nature for energy transduction and storage.[425] PDA can be synthesized *in situ* through oxidative self-polymerization of dopamine, which is one of the simplest ways to harness quinone.[428,429] Consequently, PDA has been extensively investigated in artificial photosynthesis, photocatalysis, and energy harvesting and storage devices.[430,431] Ultrathin PDA films were fabricated as the light-harvesting interface for heterogeneous palladium catalyzed coupling reactions under visible light. [432] Palladium nanocrystals were grown in the PDA film to realize photocatalytic Suzuki coupling reaction involving a broad range of aryl bromides/iodides and arylboronic acid substrates.

One of the distinct advantages of PDA as a light harvesting interface is that it can be deposited on organic and inorganic materials through oxidative polymerization of dopamine with excellent control over the thickness. Such a universal deposition approach combined with the rich chemical functionality (catechol, amine, imine) of PDA makes it an attractive material for interfacing with other catalytic materials such as platinum and iridium to control couplings, oxidations, and reductions.

The multifunctional properties of PDA have been harnessed to realize bio-derived plasmonic hybrids for enhanced light harvesting and catalytic activity. *In situ* polymerized PDA on plasmonic nanostructures have been utilized to realize core-shell assemblies that exhibited enhanced light absorption and superior charge carrier generation in the photosensitizing molecules trapped within the PDA layer.[433] The PDA layer served an adhesive and reducing agent for the synthesis of the metal nanostructures and as a scaffold for hosting the photosensitizers. The hybrid structures were realized through a simple three-step process: (i) formation of thin PDA film on a flexible substrate through oxidative self-polymerization of dopamine; (ii) *in situ* growth of Au nanostructures using reducing ability of the catecholic moieties of PDA; and (iii) deposition of PDA layer encapsulating the photosensitizer around the plasmonic nanostructures. The photocatalytic activity in the presence of Au nanostructures, which serve as nanoantennas. Specifically, the photoregenration of NAD^+ to NADH (nicotinamide cofactor) was found to increase from 2.1% to 14.7% with the addition of Au nanostructures within the PDA film. In a more recent study, the same group has demonstrated light harvesting materials comprised Al nanoparticles and PDA coating (Figure 31a).[434]
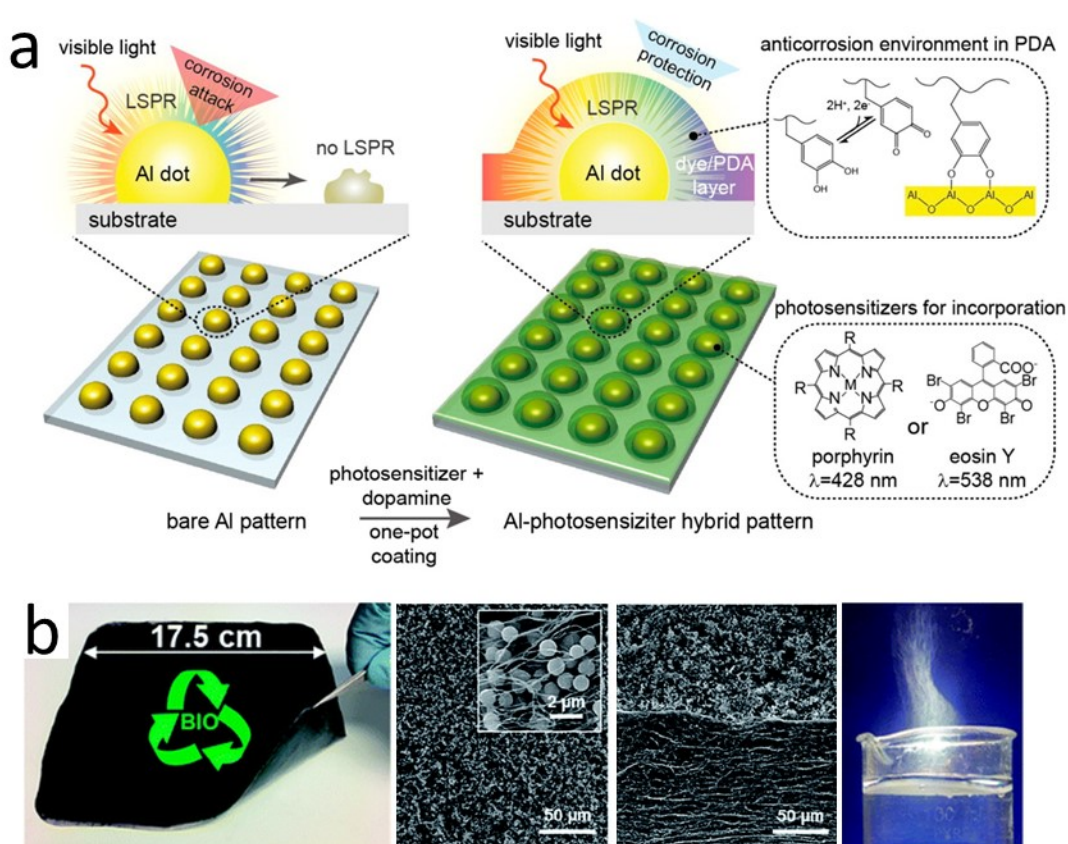
Figure 31. Light harvesting enabled by natural materials. (a) PDA encapsulated Al nanoarrays for plasmonic-enhanced light harvesting.[434] Reprinted from ref. 434 with permission from American Chemical Society, copyright 2015. (b) Biodegradable interfacial evaporator based on PDA and BNC. Photograph of a large area bilayer PDA/BNC hydrogel. SEM images of surface and cross-section of a PDA/BNC foam. Optical image of steam generation.[440] Reprinted from ref. 440 with permission from Royal Society of Chemistry, copyright 2017.

Highly efficient solar steam generation using interfacial evaporators is being widely explored as a promising water treatment and desalination.[435,436] The interfacial evaporators efficiently harvest the sunlight and result in evaporation of water that is subsequently collected as fresh water. Bacterial nanocellulose (BNC) and modified wood materials were explored as a bio-based material platform for realizing interfacial evaporators with a variety of photothermal absorbers including reduced graphene oxide (RGO), PDA nanoparticles, MoS$_2$ flakes, and metal plasmonic nanoparticles. [437,438,439] Recently, PDA nanoparticle-loaded BNC bilayered foam has been demonstrated for solar steam generation, which is comprised of a pristine BNC bottom layer and PDA particle-loaded BNC as a top layer (Figure 31b).[440] The size of the PDA particles were tuned to achieve maximum overlap between the absorption of PDA particles and the solar spectrum. Optimized light absorption was achieved for PDA particles with a diameter of ~1 μm. The PDA/BNC bilayered foam exhibited solar steam generation efficiency of ~78%. The excellent

efficiency of this interfacial evaporator completely based on natural materials is ascribed to high light absorption, outstanding photothermal conversion, excellent heat localization, and rapid water transport.

6. Conclusion and outlook

In this review, we have provided a summary of the recent research in harnessing natural materials for the fabrication of bio-enabled photonic structures. Living organisms have developed and refined materials, structures, and processes to selectively absorb, reflect, scatter, transmit, guide, and harvest light. Remarkably, nature achieved a broad range of photonic structures with relatively simple materials and at mild processing conditions, which makes them particularly attractive. These materials at the macro, micro, and nanoscales have served as a great source of inspiration for designing synthetic analogues.

Natural polymers offer numerous advantages compared to their synthetic counterparts as building blocks for photonic structures. The most significant advantages of biopolymers include not only the unique combination of optical and mechanical properties, but also important auxiliary properties, which are critical for real-world applications, such as renewability, diverse interfacial chemistries, biocompatibility, and controlled thermal properties (Figure 32).[441,442,443] Although it is possible to choose synthetic materials with a specific set of optical properties for a given photonic structure, such materials often exhibit modest mechanical or thermal properties imposing severe limitations in their real-world application. For example, glass fibers are excellent candidates as waveguides with extremely low optical loss. However, their application in biomedical research is limited by their mechanical mismatch with soft biological tissues and no biodegradability.

As has been discussed in detail in this review, naturally derived materials, which are inherently biocompatible and biodegradable offer numerous handles (e.g., physical and chemical crosslinking, tunable chemistry) to finely control the properties (chemical, mechanical, optical, thermal) and meet the requirements set by the specific applications. The rich chemical functionality of naturally derived polymers is yet another feature that makes them more attractive as compared to synthetic polymers. The chemical functionality can be harnessed to create hybrid materials (organic/inorganic, biotic/abiotic) with tailored interfaces through either integration pre-synthesized materials or *in situ* growth processes.
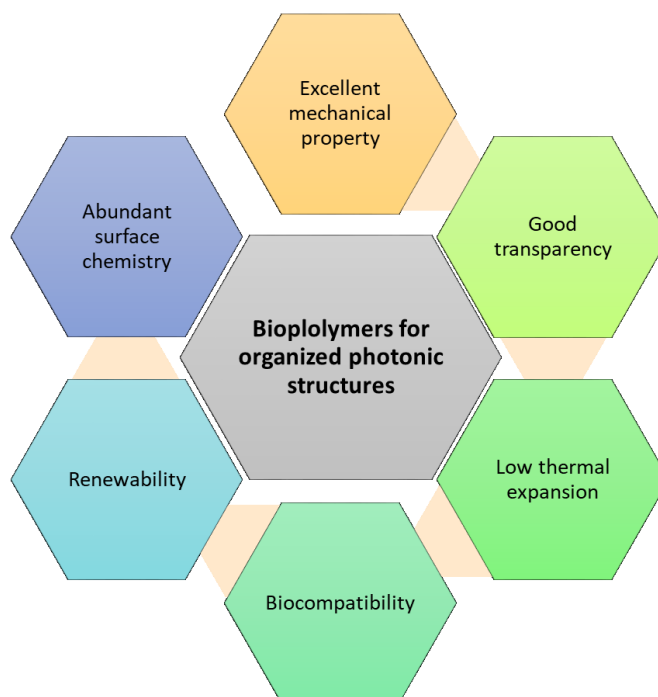
Figure 32. The general benefits of biopolymers for organized photonic structures.

To achieve the full potential of bio-enabled photonic structures, the capability of high-efficiency light transport with low loss is the most basic requirement. Most of the biopolymers are highly transparent in the visible wavelength range, although have strong light absorption at shorter wavelengths below 350 nm. In addition, the refractive index of the material components should be higher than that of the surrounding media to generate photonic phenomena. To this end, the refractive index of cellulose, chitin and silk are very similar and all are around 1.50 within 10% deviation. Another important benefit of biopolymers is their excellent mechanical robustness, elasticity, and flexibility, which are critical for the durability of photonic optical systems/devices for practical applications. For example, owing to the highly crystalline structure, cellulose and chitin nanofibers are much stronger than most synthetic polymers.[9] Finally, the coefficient of thermal expansion of biopolymers (<5 ppm k^{-1}) is much lower than regular polymer materials (20-100 ppm k^{-1}),[444] which renders photonic structures with good thermal stability that is important in the application in energy harvesting.

Natural materials have evolved to efficiently capture energy from the sun and convert it into chemical energy with an overall efficiency that cannot be matched by any manmade materials. Natural materials are evolving to be an integral part of energy harvesting systems both as passive (structural integrity) and active (light harvesting) components. Overall, photonic structures made from these naturally abundant materials can be broadly deployed in various ecosystems with

minimal environmental risk, thus enabling environmentally benign and sustainable energy collection and conversion.

Despite the exciting progress made in the past two decades, processing of naturally derived materials into large-scale photonic structures still remains a fundamental challenge. The key requirement of photonic structures is the precise organization of the building blocks across multi-length scales. Unfortunately, the current fabrication approaches are not satisfactory in terms of reproducibility and high spatial resolution. The assembly of CNCs for chiral nematic structures, for instance, is not readily reproducible even from the same batch of CNC dispersion and within large volumes in many cases. There are numerous parameters that determine the final chiral structures, and even a small variation might result in a different structural color. Naturally, such high sensitivity of the final structures to the experimental parameters leads to poor reproducibility of the experimental results within/across laboratories.

Additionally, the purity of the structural colors that is related to the uniformity of periodical structures is barely satisfactory. Although the structural color in many cases looks homogenous under naked eyes, multi-color domains can be observed under polarized microscopy and broad reflection peaks occur because of the poor homogeneity of structures. Another concern with the current fabrication techniques, such as the photolithography, is the uncertain prospects of scalability. Even though some of these techniques produce uniform photonic structures from biopolymer building blocks under rigorously controlled fabrication conditions, the scalability of such approaches remains unclear. Hence, comprehensive studies on how to efficiently control the micro and nanoscale structures of photonic materials at a large scale are still desperately needed, especially for industrial production, where cost and performance are valued equally.

The rapid emergence of additive manufacturing techniques provides new tools to construct photonic architectures over multiple length-scales and dimensions. In particular, the capability of fabricating various hierarchical 3D photonic crystal structures makes them attractive. Considering that the biopolymers are typically processed in aqueous-rich environment, the manufacturing techniques that are suitable for processing include stereo-lithography that use light to cure designed areas in biopolymer suspensions and inkjet printing. Additive-manufacturing technologies have been used to build functional architectures from biopolymers for electronic devices, electrical conductors, tissue-engineering scaffolds, sensors and actuators.[177,445,446,447] However, one can find only a few examples in literature that explore these approaches for fabricating photonic structures because most current techniques are limited to microscale features.

However, as is well known and discussed above, most of the photonic structures require submicron feature sizes on the order of the wavelength of light and, in some cases, even finer control of the structure at the nanoscale. With the unremitting efforts to improve the feature resolution, some progress has been made, although very limited to date. Recently, an aqueous multiphoton lithography has been developed to fabricate various features with resolution of 350 nm from silk solution.[177] In another study, 3D structures with high resolution (down to 50 nm) were achieved by using ion and electron beams to crystalize silk materials with very limited productivity rate though.[176] With continuing improvements in the reducing feature size and broadening materials palette, there is no doubt that additive manufacturing methods are an attractive path towards fabricating photonic materials. Simultaneously, integration of multiple micro and nanostructural materials (both biotic and abiotic) for realizing multi-photonic functionalities (e.g. including non-linear phenomena) will be the future focus in the development of bio-enabled photonic materials. Efforts on the rational integration of biotic and abiotic photonic materials, although underway, are at their inception.

The translation of the natural motifs into artificial photonic materials will require a deep understanding of the optical properties of the materials and photonic properties of the corresponding structures. It requires multiscale modelling approaches to establish structure-photonic property relationships in hierarchically organized photonic materials and to guide the design of a new class of biophotonic materials. In addition to the multi-scale approaches, it will be highly advantageous for these modelling methods to involve a multi-physics approach that enables further optimization of the materials for auxiliary properties such as enhanced mechanical properties (e.g., high flexibility, resilience, strength) and thermal properties (e.g., low thermal expansion and thermal conductivity). The complexity of the underlying processes related to the physical and chemical properties of the constituents (such as biopolymer molecular weight, nanocrystal aspect ratio, complex cross-section, local twisting power, heterogeneous surface chemistry, and blending components) hinders the understanding of the complex photonic phenomena of organized biomaterials and corresponding composites.

Additionally, integrating of natural polymers with other natural and synthetic components is challenging but very attractive for emerging applications such as soft photonic sensors, robots and actuating devices. The combination of photonic materials with photovoltaic materials might advance sustainable energy-harvesting and generation approaches. We suggest that the biophotonic materials and structures will undergo tremendous development in the next decade to

meet the demand for next-generation sustainable, biocompatible, biodegradable, lightweight, non-toxic, flexible, wearable, implantable, and ingestible photonic devices.

Overall, compared to colors generated from traditional chemical or biological pigments or metallic nanostructures, photonic-based structural colors generally exhibit little dissipative loss and biophotonic structures are able to create a gamut of bright and deep non-fading colors. Moreover, a special iridescent color effect can be generated by periodic structural systems and is particularly conspicuous to the human eye that finding applications in visual arts. Besides, the structural color generated by biophotonic structures can be complex compared to pigments and this makes them useful for security, where marks of authentication are required. Finally, a deeper and lustrous "chameleon" iridescent colors have been introduced by Mercedes-Benz and deep structural "blue paint" as "LC Structural Blue Edition" has been developed by Toyota for special editions of their Lexus brand for demanding customers (Figure 33).[448] Its appearance, to great extent, mimics the deep color of butterfly wings (compare with Figure 4b).

Figure 33. Lexus® car with dazzling "structural blue" color (with permission from Toyota Motor North America).

However, to date, there are very few other examples of the large-scale practical applications of bioinspired materials with designed structural colors realized as commercially available bio-derived or synthetic products. To promote broad applications and to make such biophotonic-inspired products truly mass-producible, the overall cost of the coating process and corresponding materials needs to be significantly reduced. Novel renewable materials and methods, especially those compatible with industrial scale production, to efficiently control the photonic structure over a large scale are required for further progress. Yet another aspect that requires consideration in real-world larger-scale applications of structural colors is the possibility of self-healing in such complex coatings. Considering that their unique optical properties are highly sensitive to the micro and nanoscale structural defects, it is important to effectively preserve objects with structural color during routine use (involving scratches, and minor collisions) and possibly restore

the fine and multi-length scale structural features after unwanted damage and wide variation of temperature through smart self-healing. Clearly, these aspects will become more important as structural colors transitioning from being a "novelty" to the "norm", even if expensive one…

ACKNOWLEDGMENTS

References

[1] S. Tadepalli, J. M. Slocik, M. K. Gupta, R. R. Naik and S. Singamaneni, *Chem. Rev.*, 2017, **117**, 12705–12763.

[2] Y. Zhao, Z. Xie, H. Gu, C. Zhu and Z. Gu, *Chem. Soc. Rev.*, 2012, **41**, 3297–3317.

[3] A. P. C. Almeida, J. P. Canejo, S. N. Fernandes, C. Echeverria, P. L. Almeida and M. H. Godinho, *Adv. Mater.*, 2018, **30**, 1703655.

[4] L. Shang, W. Zhang, K. Xu and Y. Zhao, *Mater. Horiz.*, 2019,**6**, 945-958.

[5] Y. Liu, K. He, G. Chen, W. R. Leow and X. Chen, *Chem. Rev.*, 2017, **117**, 12893–12941.

[6] M. B. Applegate, J. Coburn, B. P. Partlow, J. E. Moreau, J. P. Mondia, B. Marelli, D. L. Kaplan and F. G. Omenetto, *Proc. Natl. Acad. Sci.*, 2015, **112**, 12052–12057.

[7] T. R. Ray, J. Choi, A. J. Bandodkar, S. Krishnan, P. Gutruf, L. Tian, R. Ghaffari and J. A. Rogers, *Chem. Rev.*, 2019, **119**, 5461-5533.

[8] R. Xiong, A. M. Grant, R. Ma, S. Zhang and V. V. Tsukruk, *Mater. Sci. Eng. R Rep.*, 2018, **125**, 1–41.

[9] S. Ling, W. Chen, Y. Fan, K. Zheng, K. Jin, H. Yu, M. J. Buehler and D. L. Kaplan, *Prog. Polym. Sci.*, 2018, **85**, 1–56.

[10] S. Ling, D. L. Kaplan and M. J. Buehler, *Nat. Rev. Mater.*, 2018, **3**, 18016.

[11] E. Kontturi, P. Laaksonen, M. B. Linder, Nonappa, A. H. Gröschel, O. J. Rojas and O. Ikkala, *Adv. Mater.*, 2018, **30**, 1703779.

[12] H. Tao, D. L. Kaplan and F. G. Omenetto, *Adv. Mater.*, 2012, **24**, 2824–2837.

[13] Y. Wang, J. Guo, L. Zhou, C. Ye, F. G. Omenetto, D. L. Kaplan and S. Ling, *Adv. Funct. Mater.*, 2018, **28**, 1805305.

[14] B. D. Lawrence, M. Cronin-Golomb, I. Georgakoudi, D. L. Kaplan and F. G. Omenetto, *Biomacromolecules*, 2008, **9**, 1214–1220.

[15] T. H. Zhao, R. M. Parker, C. A. Williams, K. T. P. Lim, B. Frka-Petesic and S. Vignolini, *Adv. Funct. Mater.*, 2018, 1804531.

[16] O. Kose, A. Tran, L. Lewis, W. Y. Hamad and M. J. MacLachlan, *Nat. Commun.*, 2019, **10**, 510.

[17] T. Li, M. Zhu, Z. Yang, J. Song, J. Dai, Y. Yao, W. Luo, G. Pastel, B. Yang and L. Hu, *Adv. Energy Mater.*, 2016, **6**, 1601122.

[18] H.-L. Liang, M. M. Bay, R. Vadrucci, C. H. Barty-King, J. Peng, J. J. Baumberg, M. F. De Volder and S. Vignolini, *Nat. Commun.*, 2018, **9**, 4632.

[19] D. Shan, E. Gerhard, C. Zhang, J. W. Tierney, D. Xie, Z. Liu and J. Yang, *Bioact. Mater.*, 2018, **3**, 434–445.

[20] L. Wu, J. He, W. Shang, T. Deng, J. Gu, H. Su, Q. Liu, W. Zhang, D. Zhang, *Adv. Optical Mater.*, 2016, **4**, 195–224.

[21] *Photonics of Biopolymers*, By Nikolai L. Vekshin, Springer-Verlag Berlin Heidelberg 2002, ISBN 978-3-642-07855-2, DOI 10.1007/978-3-662-04947-1

[22] Z. Liu, M. A. Meyers, Z. Zhang and R. O. Ritchie, *Prog. Mater. Sci.*, 2017, **88**, 467–498.

[23] M. Kolle, P. M. Salgard-Cunha, M. R. J. Scherer, F. Huang, P. Vukusic, S. Mahajan, J. J. Baumberg and U. Steiner, *Nat. Nanotechnol.*, 2010, **5**, 511–515.

[24] Y. Uchida, Y. Takanishi and J. Yamamoto, *Adv. Mater.*, 2013, **25**, 3234–3237.

[25] O. Benson, *Nature*, 2011, **480**, 193–199.

[26] E. R. Dufresne, H. Noh, V. Saranathan, S. G. J. Mochrie, H. Cao and R. O. Prum, *Soft Matter*, 2009, **5**, 1792–1795.

[27] S. Kinoshita and S. Yoshioka, *ChemPhysChem*, 2005, **6**, 1442–1459.

[28] E. Shevtsova, C. Hansson, D. H. Janzen and J. Kjærandsen, *Proc. Natl. Acad. Sci.*, 2011, **108**, 668–673.

[29] F. Schenk, B. D. Wilts and D. G. Stavenga, *Bioinspir. Biomim.*, 2013, **8**, 045002.

[30] T. R. Matin, M. K. Leong, B. Y. Majlis and I. C. Gebeshuber, *AIP Conf. Proc.*, 2010, **1284**, 5–14.

[31] P. Vukusic, J. R. Sambles and C. R. Lawrence, *Nature*, 2000, **404**, 457.

[32] C. Campos-Fernández, D. E. Azofeifa, M. Hernández-Jiménez, A. Ruiz-Ruiz and W. E. Vargas, *Opt. Mater. Express*, 2011, **1**, 85–100.

[33] D. Gur, B. Leshem, D. Oron, S. Weiner and L. Addadi, *J. Am. Chem. Soc.*, 2014, **136**, 17236–17242.

[34] B. D. Wilts, K. Michielsen, H. D. Raedt and D. G. Stavenga, *Proc. Natl. Acad. Sci.*, 2014, **111**, 4363–4368.

[35] T. M. Jordan, J. C. Partridge and N. W. Roberts, *Nat. Photonics*, 2012, **6**, 759–763.

[36] D. G. Stavenga, B. D. Wilts, H. L. Leertouwer and T. Hariyama, *Philos. Trans. R. Soc. Lond. B Biol. Sci.*, 2011, **366**, 709–723.

[37] K. Sakoda, *Optical Properties of Photonic Crystals*, Springer Science & Business Media, 2004.

[38] C. Fenzl. T. Hirsch and O. S. Wolfbeis, *Angew. Chem.*, 2014, **53**, 3318-3335.

[39] J. D. Joannopoulos, S. G. Johnson, J. N. Winn and R. D. Meade, *Photonic Crystals: Molding the Flow of Light - Second Edition*, Princeton University Press, 2011.

[40] U. G. Wegst, H. Bai, E. Saiz, A. P. Tomsia and R. O. Ritchie, *Nat. Mater.*, 2015, **14**, 23.

[41] T. L. Tan, D. Wong and P. Lee, *Opt. Express*, 2004, **12**, 4847–4854.

[42] T. Starkey and P. Vukusic, *Nanophotonics*, 2013, **2**, 289–307.

[43] I. Zada, W. Zhang, Y. Li, P. Sun, N. Cai, J. Gu, Q. Liu, H. Su and D. Zhang, *Appl. Phys. Lett.*, 2016, **109**, 153701.

[44] Stavenga D.G, Foletti S, Palasantzas G and Arikawa K, *Proc. R. Soc. B Biol. Sci.*, 2006, **273**, 661–667.

[45] I. A. Sukhoivanov and I. V. Guryev, *Photonic Crystals: Physics and Practical Modeling*, Springer, 2009.

[46] S. G. Johnson and J. D. Joannopoulos, *Photonic Crystals: The Road from Theory to Practice*, Springer Science & Business Media, 2001.

[47] K. Inoue and K. Ohtaka, *Photonic Crystals: Physics, Fabrication and Applications*, Springer Science & Business Media, 2004.

[48] F. Marlow, Muldarisnur, P. Sharifi, R. Brinkmann and C. Mendive, *Angew. Chem. Int. Ed.*, 2009, **48**, 6212–6233.

[49] E. Armstrong and C. O'Dwyer, *J. Mater. Chem. C*, 2015, **3**, 6109–6143.

[50] E. Gaillou, A. Delaunay, B. Rondeau, M. Bouhnik-le-Coz, E. Fritsch, G. Cornen and C. Monnier, *Ore Geol. Rev.*, 2008, **34**, 113–126.

[51] M. A. S. Kalceff, M. R. Phillips, A. R. Moon and A. Smallwood, *Phys. Chem. Miner.*, 1997, **24**, 131–138.

[52] E. Gaillou, E. Fritsch, B. Aguilar-Reyes, B. Rondeau, J. Post, A. Barreau and M. Ostroumov, *Am. Mineral.*, 2008, **93**, 1865–1873.

[53] S. Kinoshita, *Structural Colors in the Realm of Nature*, World Scientific, 2008.

[54] J. W. Galusha, L. R. Richey, J. S. Gardner, J. N. Cha and M. H. Bartl, *Phys. Rev. E*, 2008, **77**, 050904.

[55] J. W. Galusha, M. R. Jorgensen and M. H. Bartl, *Adv. Mater.*, 2010, **22**, 107–110.

[56] S. G. Johnson, J. D. Joannopoulos, *Opt. Express*, 2001, **8**, 173-190.

[57] https://www.synopsys.com/optical-solutions/rsoft/passive-device-bandsolve.html.

[58] V. Sharma, M. Crne, J. O. Park and M. Srinivasarao, *Science*, 2009, **325**, 449–451.

[59] T. J. Bunning, L. V. Natarajan, V. P. Tondiglia and R. L. Sutherland, *Annu. Rev. Mater. Sci.,* 2000, **30**, 83–115.

[60] T. Lenau and M. Barfoed, *Adv. Eng. Mater.*, 2008, **10**, 299–314.

[61] S. Vignolini, P. J. Rudall, A. V. Rowland, A. Reed, E. Moyroud, R. B. Faden, J. J. Baumberg, B. J. Glover and U. Steiner, *Proc. Natl. Acad. Sci.*, 2012, **109**, 15712–15715.

[62] S. Kinoshita, S. Yoshioka and J. Miyazaki, *Rep. Prog. Phys.*, 2008, **71**, 076401.

[63] J. C. Weaver, G. W. Milliron, A. Miserez, K. Evans-Lutterodt, S. Herrera, I. Gallana, W. J. Mershon, B. Swanson, P. Zavattieri, E. DiMasi, et al., *Science* **2012**, 336, 1275–1280.

[64] W. J. Choi, G. Cheng, Z. Huang, S. Zhang, T. B. Norris and N. A. Kotov, *Nat. Mater.,* 2019, **18**, 820-826.

[65] Caveney S. and Pringle John William Sutton, *Proc. R. Soc. Lond. B Biol. Sci.*, 1971, **178**, 205–225.

[66] M. S. Toivonen, O. D. Onelli, G. Jacucci, V. Lovikka, O. J. Rojas, O. Ikkala and S. Vignolini, *Adv. Mater.*, 2018, **30**, 1704050.

[67] M. Burresi, L. Cortese, L. Pattelli, M. Kolle, P. Vukusic, D. S. Wiersma, U. Steiner and S. Vignolini, *Sci. Rep.*, 2014, **4**, 6075.

[68] S. M. Luke, B. T. Hallam and P. Vukusic, *Appl. Opt.*, 2010, **49**, 4246–4254.

[69] P. Vukusic, B. Hallam and J. Noyes, *Science*, 2007, **315**, 348–348.

[70] L. Cortese, L. Pattelli, F. Utel, S. Vignolini, M. Burresi and D. S. Wiersma, *Adv. Opt. Mater.*, 2015, **3**, 1337–1341.

[71] R. J. D. Tilley, J. N. Eliot and H. Yoshimoto, *Lepidoptera Sci.*, 2002, **53**, 153–180.

72 B. D. Wilts, X. Sheng, M. Holler, A. Diaz, M. Guizar-Sicairos, J. Raabe, R. Hoppe, S.-H. Liu, R. Langford, O. D. Onelli, D. Chen, S. Torquato, U. Steiner, C. G. Schroer, S. Vignolini and A. Sepe, *Adv. Mater.*, 2018, **30**, 1702057.

73 M. Li, U. Guler, Y. Li, A. B. Rea, E. K Tanyi, Y. Kim, M. A. Noginov, Y. Song, A. Boltasseva, V. M. Shalaev, N. A. Kotov, *ACS Energy Lett.*, 2018, **3**, 1578-1583.

74 L. Zhou1, Y. Tan, D. Ji, B. Zhu, P. Zhang, J. Xu, Q. Gan, Z. Yu and J. Zhu, *Sci. Adv.*, 2016, **2** e1501227.

75 Y. Zhai, Y. Ma, S. N. David, D. Zhao, R. Lou, G. Tan, R Yang and X. Yin, *Science*, 2017, **355**, 1062-1066.

76 N. Liu and T. Liedl, *Chem. Rev.*, 2018, **118**, 3032–3053.

77 S. J. Tan, M. J. Campolongo, D. Luo and W. Cheng, *Nat. Nanotechnol.*, 2011, **6**, 268–276.

78 A. Kuzyk, R. Schreiber, Z. Fan, G. Pardatscher, E.-M. Roller, A. Högele, F. C. Simmel, A. O. Govorov and T. Liedl, *Nature*, 2012, **483**, 311–314.

79 M. R. Jones, K. D. Osberg, R. J. Macfarlane, M. R. Langille and C. A. Mirkin, *Chem. Rev.*, 2011, **111**, 3736–3827.

80 B. Thomas, M. C. Raj, A. K. B, R. M. H, J. Joy, A. Moores, G. L. Drisko and C. Sanchez, *Chem. Rev.*, 2018, **118**,11575–11625.

81 D. Klemm, F. Kramer, S. Moritz, T. Lindström, M. Ankerfors, D. Gray and A. Dorris, *Angew. Chem. Int. Ed.*, 2011, **50**, 5438–5466.

82 W. Chen, Q. Li, Y. Wang, X. Yi, J. Zeng, H. Yu, Y. Liu and J. Li, *ChemSusChem*, 2014, **7**, 154–161.

83 R. Xiong, H. S. Kim, L. Zhang, V. F. Korolovych, S. Zhang, Y. G. Yingling and V. V. Tsukruk, *Angew. Chem.*, 2018, **130**, 8644–8649.

84 R. Xiong, H. S. Kim, S. Zhang, S. Kim, V. F. Korolovych, R. Ma, Y. G. Yingling, C. Lu and V. V. Tsukruk, *ACS Nano*.

85 J. Li, X. Wei, Q. Wang, J. Chen, G. Chang, L. Kong, J. Su and Y. Liu, *Carbohydr. Polym.*, 2012, **90**, 1609–1613.

86 K. Abe, S. Iwamoto and H. Yano, *Biomacromolecules*, 2007, **8**, 3276–3278.

87 W. Chen, H. Yu, Y. Liu, P. Chen, M. Zhang and Y. Hai, *Carbohydr. Polym.*, 2011, **83**, 1804–1811.

88 L. Zhang, T. Tsuzuki and X. Wang, *Cellulose*, 2015, **22**, 1729–1741.

89 T. Saito, S. Kimura, Y. Nishiyama and A. Isogai, *Biomacromolecules*, 2007, **8**, 2485–2491.

90 A. Isogai, T. Saito and H. Fukuzumi, *Nanoscale*, 2011, **3**, 71–85.

91 H. Fukuzumi, T. Saito, T. Iwata, Y. Kumamoto and A. Isogai, *Biomacromolecules*, 2009, **10**, 162–165.

92 M. Iguchi, S. Yamanaka and A. Budhiono, *J. Mater. Sci.*, 2000, **35**, 261–270.

93 Y. Huang, C. Zhu, J. Yang, Y. Nie, C. Chen and D. Sun, *Cellulose*, 2014, **21**, 1–30.

94 O. van den Berg, J. R. Capadona and C. Weder, *Biomacromolecules*, 2007, **8**, 1353–1357.

95 S. Iwamoto, W. Kai, A. Isogai and T. Iwata, *Biomacromolecules*, 2009, **10**, 2571–2576.

96 W. Y. Hamad and T. Q. Hu, *Can. J. Chem. Eng.* 2010, **88**,392-402.

97 V. F. Korolovych, V. Cherpak, D. Nepal, A. Ng, N. R. Shaikh, A. Grant, R. Xiong, T. J. Bunning and V. V. Tsukruk, *Polymer*, 2018, **145**, 334–347.

98 H. Yu, Z. Qin, B. Liang, N. Liu, Z. Zhou and L. Chen, *J. Mater. Chem. A*, 2013, **1**, 3938–3944.

99 G. Nyström, M. Arcari, J. Adamcik, I. Usov and R. Mezzenga, *ACS Nano*, 2018, **12**, 5141–5148.

100 S. Wang, A. Lu and L. Zhang, *Prog. Polym. Sci.*, 2016, **53**, 169–206.

101 H.-P. Fink, P. Weigel, H. J. Purz and J. Ganster, *Prog. Polym. Sci.*, 2001, **26**, 1473–1524.

102 H. Wang, G. Gurau and R. D. Rogers, *Chem. Soc. Rev.*, 2012, **41**, 1519–1537.

103 T. Rosenau, A. Potthast, I. Adorjan, A. Hofinger, H. Sixta, H. Firgo and P. Kosma, *Cellulose*, 2002, **9**, 283–291.

104 H. Zhang, J. Wu, J. Zhang and J. He, *Macromolecules*, 2005, **38**, 8272–8277.

105 T. R. Dawsey and C. L. McCormick, *J. Macromol. Sci. Part C*, 1990, **30**, 405–440.

106 Q. Yang, H. Fukuzumi, T. Saito, A. Isogai and L. Zhang, *Biomacromolecules*, 2011, **12**, 2766–2771.

107 A. C. O'SULLIVAN, *Cellulose*, 1997, **4**, 173–207.

108 M. A. S. Azizi Samir, F. Alloin and A. Dufresne, *Biomacromolecules*, 2005, **6**, 612–626.

109 P. S. Belton, S. F. Tanner, N. Cartier and H. Chanzy, *Macromolecules*, 1989, **22**, 1615–1617.

110 H. Yamamoto and F. Horii, *Macromolecules*, 1993, **26**, 1313–1317.

111 H. Yamamoto and F. Horn, *Cellulose*, 1994, **1**, 57–66.

112 R. J. Moon, A. Martini, J. Nairn, J. Simonsen and J. Youngblood, *Chem. Soc. Rev.*, 2011, **40**, 3941–3994.

113 N-H. K, T. Imai, M. Wada and J. Sugiyama, *Biomcaromolecules*, 2006, **7**, 274-280.

114 A. J. Stipanovic and A. Sarko, *Macromolecules*, 1976, **9**, 851-857.

115 M. Wada, Y. Nishiyama and P. Langan*, Macromolecules*, 2006, **39**, 2947-2952.

116 M. Wada, L. Heux, A. Isogai, Y. Nishiyama, H. Chanzy and J. Sugiyama, *Macromolecules*, 2001, **34**, 1237-1243.

117 M. Wadam L. Heux and J. Sugiyama, *Biomacromolecules*, 2004, **5**, 1385-1391.

118 C. K. S. Pillai, W. Paul and C. P. Sharma, *Prog. Polym. Sci.*, 2009, **34**, 641–678.

119 D. Raabe, C. Sachs and P. Romano, *Acta Mater.*, 2005, **53**, 4281–4292.

120 P.-Y. Chen, A. Y.-M. Lin, J. McKittrick and M. A. Meyers, *Acta Biomater.*, 2008, **4**, 587–596.

121 E. Atkins, *J. Biosci.*, 1985, **8**, 375–387.

122 Y. Ogawa, C. M. Lee, Y. Nishiyama and S. H. Kim, *Macromolecules*, 2016, **49**, 7025–7031.

123 S. Nikolov, M. Petrov, L. Lymperakis, M. Friák, C. Sachs, H.-O. Fabritius, D. Raabe and J. Neugebauer, *Adv. Mater.*, 2010, **22**, 519–526.

124 J.-B. Zeng, Y.-S. He, S.-L. Li and Y.-Z. Wang, *Biomacromolecules*, 2012, **13**, 1–11.

125 S. Ifuku, M. Nogi, K. Abe, M. Yoshioka, M. Morimoto, H. Saimoto and H. Yano, *Biomacromolecules*, 2009, **10**, 1584–1588.

126 Y. Fan, T. Saito and A. Isogai, *Biomacromolecules*, 2008, **9**, 1919–1923.

127 Y. Fan, T. Saito and A. Isogai, *Biomacromolecules*, 2008, **9**, 192–198.

128 P. Samyn and A. Osorio-Madrazo, in *Handbook of Nanofibers*, eds. A. Barhoum, M. Bechelany and A. Makhlouf, Springer International Publishing, Cham, 2018, pp. 1–36.

129 S. Ifuku, *Molecules*, 2014, **19**, 18367–18380.

130 H. EL. Knidri. J. Dahmani, A. Addaou, A. Laajeb and A. Lahsini, *Int. J Biol. Macromo.,* 2019, **139**, 1092-1102.

131 A. C. O'Sullivan, *Cellulose*, 1997, **4**, 173-207.

132 J. Kumirska, M. Czerwicka, Z. Kazynski, A. Bychowska, K. Brzozowski and J. Thöming, P. Stepnowski, *Mar. Drugs* 2010, **8**, 1567-1636.

133 J. D. Goodrich and W. T. Winter, *Biomacromolecules*, 2007, **8**, 252–257.

134 C. K. S. Pillai, W. Paul and C. P. Sharma, *Prog. Polym. Sci.* 2009, **34**, 641-678.

135 M. Dash, F. Chiellini, R. M. Ottenbrite and E. Chiellini, *Prog. Polym. Sci.* 2011, **36**, 981-1014.

136 H. Yi, L. Wu, W. E. Bentley, R. Ghodssi, G. W. Rubloff, J. N. Culver and G. F. Payne, *Biomacromolecules*, 2005, **6**, 2881–2894.

137 H. J. Jin and D. L. Kaplan, *Nature*, 2003, **424**, 1057.

138 W. Huang, S. Ling, C. Li, F. G. Omenetto and D. L. Kaplan, *Chem. Soc. Rev.*, 2018, **47**, 6486–6504.

139 V. Volkov, A. V. Ferreira and A. Cavaco-Paulo, *Macromol. Mater. Eng.*, 2015, **300**, 1199–1216.

140 S. Keten, Z. Xu, B. Ihle and M. J. Buehler, *Nat. Mater.*, 2010, **9**, 359–367.

141 D. N. Rockwood, R. C. Preda, T. Yücel, X. Wang, M. L. Lovett and D. L. Kaplan, *Nat. Protoc.*, 2011, **6**, 1612–1631.

142 F. Takei, Y. Kikuchi, A. Kikuchi, S. Mizuno and K. Shimura, *J. Cell Biol.*, 1987, **105**, 175–180.

143 F. Vollrath and D. Porter, *Polymer*, 2009, **50**, 5623–5632.

144 M. L. Gulrajani*, Rev. Prog. Coloration*, 1992, **22**, 79-89.

145 R. L. Hill, *Adv. Protein Chem.,* 1965, **20**, 37-107.

146 G. Freddi, G. Pessina and M. Tsukada, *Int. J. Biol. Macromol.,* 1999, **24**, 251-263.

147 K. Nultsch, L. K. Bast, M. Näf, S. El. Yakhlifi, N. Bruns and O. Germershaus. *Macromol. Mater. Eng.,* 2018, **303**, 1800408.

148 P. P. Viktorov and Z .S. Block, *Textil. Prom.,* 1933, **11**, 43-46.

149 Q. Wang, Q. Chen, Y. Yang, Z. Shao, *Biomacromolecules* 2013, **14**, 285−289

150 D. M. Philips, L. F. Drummy, D. G. Conrady, D. M. Fox, R. R. Naik, M. O. Stones, P. C. Trulove, H. C. De Long and R. A. Mantz, *J. Am. Chem. Soc.,* 2004, **126**, 14350-14351.

151 F. Zhang, Q. Lu, J. Ming, H. Dou, Z. Liu, B. Zuo, M. Qin, M. Qin, F. Li, D. Kaplan and X. Zhang*, J. Mater. Chem*. B, 2014, **2**, 3879–3885.

152 H. J. Cho, C. S. Ki, H. Oh, K. H. Lee and I. C. Um, *Int. J. Biol. Macromol.*, 2012, **51**, 336-341.

153 Y. Goto, M. Tsukada, N. Minoura, and J. Sericult. *Sci. Jpn.,* 1990, **59**, 402–409.

154 A.B. Mathur, A. Tonelli, T. Tathke and S. Hudson, *Biopolymers*, 1997, **42**, 61–74.

155 A. Ajisawa, *J. Seric. Sci. Jpn.* 1998, **67**, 91-94.

156 Y. Shimizu and J. Sericult. *Sci. Jpn.*, 1978, **47**, 417–420.

[157] X. Hu, K. Shmelev, L. Sun, E.-S. Gil, S.-H. Park, P. Cebe and D. L. Kaplan, *Biomacromolecules*, 2011, **12**, 1686–1696.

[158] C. Jiang, X. Wang, R. Gunawidjaja, Y.-H. Lin, M. K. Gupta, D. L. Kaplan, R. R. Naik and V. V. Tsukruk, *Adv. Funct. Mater.*, 2007, **17**, 2229–2237.

[159] M. Heim, D. Keerl and T. Scheibel, *Angew. Chem. Int. Ed.*, 2009, **48**, 3584–3596.

[160] S. Ling, C. Li, K. Jin, D. L. Kaplan and M. J. Buehler, *Adv. Mater.*, 2016, **28**, 7783–7790.

[161] X. Tan, W. Zhao and T. Mu, *Green Chem.*, 2018, **20**, 3625–3633.

[162] N. E. Kurland, T. Dey, S. C. Kundu and V. K. Yadavalli, *Adv. Mater.*, 2013, **25**, 6207–6212.

[163] A. Wolfberger, A. Petritz, A. Fian, J. Herka, V. Schmidt, B. Stadlober, R. Kargl, S. Spirk and T. Griesser, *Cellulose*, 2015, **22**, 717–727.

[164] S. Verma, Gaganjot, J. Tripathi, M. Katiyar and V. Verma, *Appl. Mater. Today*, 2018, **13**, 83–90.

[165] C. Ye, S. V. Nikolov, R. Calabrese, A. Dindar, A. Alexeev, B. Kippelen, D. L. Kaplan and V. V. Tsukruk, *Angew. Chem. Int. Ed.*, 2015, **54**, 8490–8493.

[166] W. Liu, Z. Zhou, S. Zhang, Z. Shi, J. Tabarini, W. Lee, Y. Zhang, S. N. G. Corder, X. Li, F. Dong, L. Cheng, M. Liu, D. L. Kaplan, F. G. Omenetto, G. Zhang, Y. Mao and T. H. Tao, *Adv. Sci.*, 2017, **4**, 1700191.

[167] N. E. Kurland, T. Dey, C. Wang, S. C. Kundu and V. K. Yadavalli, *Adv. Mater.*, 2014, **26**, 4431–4437.

[168] R. D. B. Fraser, T. P. MacRae and G. E. Rogers, *Keratins: their composition, structure and biosynthesis*. Springfield III, Charles C Thomas, 1972.

[169] B. Wang, W. Yang, J. Mckittrick and M. A. Meyers, *Prog. Mater. Sci.,* 2016, **76**, 229-318.

[170] L. Pauling, R. B. Corey, H. R. Branson, *Proc. Natl. Acad. Sci. USA*, 1951, **37**, 205–211.

[171] R. D. B. Fraser and D. A. D. Parry, *J .Struct. Biol.*, 2011,**173**, 391–405.

[172] I. Sinkiewicz, H. Staroszczyk and A. Sliwinska, *J. Food Biochem.*, 2018, **42**, e12494.

[173] S. Zhu, W. Zeng, Z. Meng, W. Luo, L. Ma, Y. Li, C. Lin, Q. Huang, Y. Lin, and X. Y. Liu, *Adv. Mater.* 2019, 1900870

[174] S. Kim, B. Marelli, M. A. Brenckle, A. N. Mitropoulos, E.-S. Gil, K. Tsioris, H. Tao, D. L. Kaplan and F. G. Omenetto, *Nat. Nanotechnol.*, 2014, **9**, 306–310.

[175] J. Park, S.-G. Lee, B. Marelli, M. Lee, T. Kim, H.-K. Oh, H. Jeon, F. G. Omenetto and S. Kim, *RSC Adv.*, 2016, **6**, 39330–39334.

[176] J. Jiang, S. Zhang, Z. Qian, N. Qin, W. Song, L. Sun, Z. Zhou, Z. Shi, L. Chen, X. Li, Y. Mao, D. L. Kaplan, S. N. G. Corder, X. Chen, M. Liu, F. G. Omenetto, X. Xia and T. H. Tao, *Adv. Mater.*, 2018, **30**, 1705919.

[177] Y.-L. Sun, Q. Li, S.-M. Sun, J.-C. Huang, B.-Y. Zheng, Q.-D. Chen, Z.-Z. Shao and H.-B. Sun, *Nat. Commun.*, 2015, **6**, 8612.

[178] W. Haske, V. W. Chen, J. M. Hales, W. Dong, S. Barlow, S. R. Marder and J. W. Perry, *Opt. Express*, 2007, **15**, 3426–3436.

[179] B. E. Kelly, I. Bhattacharya, H. Heidari, M. Shusteff, C. M. Spadaccini and H. K. Taylor, *Science*, 2019, **363**, 1075–1079.

[180] G. Huang, Y. Yin, Z. Pan, M. Chen, L. Zhang, Y. Liu, Y. Zhang and J. Gao, *Biomacromolecules*, 2014, **15**, 4396–4402.

[181] C. Zhong, A. Kapetanovic, Y. Deng and M. Rolandi, *Adv. Mater.*, 2011, **23**, 4776–4781.

[182] J. Jin, P. Hassanzadeh, G. Perotto, W. Sun, M. A. Brenckle, D. Kaplan, F. G. Omenetto and M. Rolandi, *Adv. Mater.*, 2013, **25**, 4482–4487.

[183] S. Bottan, F. Robotti, P. Jayathissa, A. Hegglin, N. Bahamonde, J. A. Heredia-Guerrero, I. S. Bayer, A. Scarpellini, H. Merker, N. Lindenblatt, D. Poulikakos and A. Ferrari, *ACS Nano*, 2015, **9**, 206–219.

[184] P. Rofouie, M. Alizadehgiashi, H. Mundoor, I. I. Smalyukh and E. Kumacheva, *Adv. Funct. Mater.*, 2018, **28**, 1803852.

[185] H. Perry, A. Gopinath, D. L. Kaplan, L. D. Negro and F. G. Omenetto, *Adv. Mater.*, 2008, **20**, 3070–3072.

[186] S. Kim, A. N. Mitropoulos, J. D. Spitzberg, H. Tao, D. L. Kaplan and F. G. Omenetto, *Nat. Photonics*, 2012, **6**, 818.

[187] K. Hou, W. Ali, J. Lv, J. Guo, L. Shi, B. Han, X. Wang and Z. Tang, *J. Am. Chem. Soc.*, 2018, **140**, 16446–16449.

[188] I. V. Nemtsev, I. A. Tambasov, A. A. Ivanenko and V. Y. Zyryanov, *Photonics Nanostructures - Fundam. Appl.*, 2018, **28**, 37–44.

189 N. Sui, Y.-H. Wang, Y.-F. Song, F.-Y. Wang, Y.-G. Ma and H.-Z. Zhang, *Appl. Phys. Express*, 2014, **7**, 025202.

190 L. Pan, H. Xu, R. Lv, J. Qiu, J. Zhao and Y. Li, *Sci. Rep.*, 2018, **8**, 4523.

191 C. I. Aguirre, E. Reguera and A. Stein, *Adv. Funct. Mater.*, 2010, **20**, 2565–2578.

192 W. J. Hyun, H. K. Lee, S. S. Oh, O. Hess, C.-G. Choi, S. H. Im and O. O. Park, *Adv. Mater.*, 2011, **23**, 1846–1850.

193 H. Lee, T. Y. Jeon, S. Y. Lee, S. Y. Lee and S.-H. Kim, *Adv. Funct. Mater.*, 2018, **28**, 1706664.

194 Y. Wang, W. Li, M. Li, S. Zhao, F. D. Ferrari, M. Liscidini and F. G. Omenetto, *Adv. Mater.*, 2019, **31**, 1805312.

195 Y. Wang, D. Aurelio, W. Li, P. Tseng, Z. Zheng, M. Li, D. L. Kaplan, M. Liscidini and F. G. Omenetto, *Adv. Mater.*, 2017, **29**, 1702769.

196 R. Xiong, S. Yu, S. Kang, K. M. Adstedt, D. Nepal, T. J. Bunning, and V. V. Tsukruk, *Adv. Mater.*,2019, DOI: doi.org/10.1002/adma.201905600.

197 G. Chu, A. Camposeo, R. Vilensky, G. Vasilyev, Pa. Martin, Da. Pisignano, and E. Zussman, *Matter*, 2019, **1**, 1–13.

198 G. Chu, D. Qu, A. Camposeo, D. Pisignano, and E. Zussman, *Mater. Horiz.* 2019, DOI: 10.1039/c9mh01485c.

199 M. C. Traub, W. Longsine and V. N. Truskett, *Annu. Rev. Chem. Biomol. Eng.*, 2016, **7**, 583–604.

200 D. Crawley, K. Nikolic and M. Forshaw, *3D Nanoelectronic Computer Architecture and Implementation*, CRC Press, 2019.

201 C. Zhang, W. Li, D. Yu, Y. Wang, M. Yin, H. Wang, Y. Song, X. Zhu, P. Chang, X. Chen and D. Li, *Adv. Mater. Interfaces*, 2017, **4**, 1601116.

202 T. Mäkelä, M. Kainlauri, P. Willberg-Keyriläinen, T. Tammelin and U. Forsström, *Microelectron. Eng.*, 2016, **163**, 1–6.

203 J. J. Amsden, P. Domachuk, A. Gopinath, R. D. White, L. D. Negro, D. L. Kaplan and F. G. Omenetto, *Adv. Mater.*, 2010, **22**, 1746–1749.

204 A. Espinha, C. Dore, C. Matricardi, M. I. Alonso, A. R. Goñi and A. Mihi, *Nat. Photonics*, 2018, **12**, 343.

205 Y. Yang, Z. Chen, X. Song, Z. Zhang, J. Zhang, K. K. Shung, Q. Zhou and Y. Chen, *Adv. Mater.*, 2017, **29**, 1605750.

206 S.-M. Chen, H.-L. Gao, Y.-B. Zhu, H.-B. Yao, L.-B. Mao, Q.-Y. Song, J. Xia, Z. Pan, Z. He, H.-A. Wu and S.-H. Yu, *Natl. Sci. Rev.*, 2018, **5**, 703–714.

207 R. M. Erb, R. Libanori, N. Rothfuchs and A. R. Studart, *Science*, 2012, **335**, 199–204.

208 Z. Dogic and S. Fraden, *Langmuir*, 2000, **16**, 7820–7824.

209 E. Grelet and S. Fraden, *Phys. Rev. Lett.*, 2003, **90**, 198302.

210 X. Mu and D. G. Gray, *Langmuir*, 2014, **30**, 9256–9260.

211 S. Matsumura, S. Kajiyama, T. Nishimura and T. Kato, *Small*, 2015, **11**, 5127–5133.

212 G. Nyström, M. Arcari and R. Mezzenga, *Nat. Nanotechnol.*, 2018, **13**, 330.

213 R. M. Parker, G. Guidetti, C. A. Williams, T. Zhao, A. Narkevicius, S. Vignolini and B. Frka-Petesic, *Adv. Mater.*, 2018, **30**, 1704477.

214 W. J. Orts, L. Godbout, R. H. Marchessault and J.-F. Revol, *Macromolecules*, 1998, **31**, 5717–5725.

215 A. Hirai, O. Inui, F. Horii and M. Tsuji, *Langmuir*, 2009, **25**, 497–502.

216 C. Schütz, M. Agthe, A. B. Fall, K. Gordeyeva, V. Guccini, M. Salajková, T. S. Plivelic, J. P. F. Lagerwall, G. Salazar-Alvarez and L. Bergström, *Langmuir*, 2015, **31**, 6507–6513.

217 B. Tjipto-Margo and G. T. Evans, *J. Chem. Phys.,* 1990, **93**, 4254

218 M. Khandelwal, and A. H. Windle, *Polymer*, 2013, **54**, 5199-5206.

219 X. M. Dong, T. Kimura, J.-F. Revol and D. G. Gray, *Langmuir*, 1996, **12**, 2076–2082.

220 X. M. Dong and D. G. Gray, *Langmuir*, 1997, **13**, 2404–2409.

221 M. Chau, S. E. Sriskandha, D. Pichugin, H. Thérien-Aubin, D. Nykypanchuk, G. Chauve, M. Méthot, J. Bouchard, O. Gang and E. Kumacheva, *Biomacromolecules*, 2015, **16**, 2455–2462.

222 J. P. Lagerwall, C. Schütz, M. Salajkova, J. Noh, J. H. Park, G. Scalia and L. Bergström, *NPG Asia Mater.*, 2014, **6**, e80.

223 J. Majoinen, E. Kontturi, O. Ikkala and D. G. Gray, *Cellulose*, 2012, **19**, 1599–1605.

224 B. D. Wilts, A. G. Dumanli, R. Middleton, P. Vukusic and S. Vignolini, *APL Photonics*, 2017, **2**, 040801.

225 A. G. Dumanli, H. M. van der Kooij, G. Kamita, E. Reisner, J. J. Baumberg, U. Steiner and S. Vignolini, *ACS Appl. Mater. Interfaces*, 2014, **6**, 12302–12306.

226 B. Frka-Petesic, G. Guidetti, G. Kamita and S. Vignolini, *Adv. Mater.*, 2017, **29**, 1701469.

227 O. O'Keeffe, P.-X. Wang, W. Y. Hamad and M. J. MacLachlan, *J. Phys. Chem. Lett.*, 2019, **10**, 278–282.

228 V. Cherpak, V. F. Korolovych, R. Geryak, T. Turiv, D. Nepal, J. Kelly, T. J. Bunning, O. D. Lavrentovich, W. T. Heller and V. V. Tsukruk, *Nano Lett.*, 2018, **18**, 6770–6777.

229 R. M. Parker, B. Frka-Petesic, G. Guidetti, G. Kamita, G. Consani, C. Abell and S. Vignolini, *ACS Nano*, 2016, **10**, 8443–8449.

230 X. Mu and D. G. Gray, *Cellulose*, 2015, **22**, 1103–1107.

231 R. S. Werbowyj and D. G. Gray, *Mol. Cryst. Liq. Cryst.*, 1976, **34**, 97–103.

232 M. H. Godinho, D. G. Gray and P. Pieranski, *Liq. Cryst.*, 2017, **44**, 2108–2120.

233 G. Kamita, B. Frka-Petesic, A. Allard, M. Dargaud, K. King, A. G. Dumanli and S. Vignolini, *Adv. Opt. Mater.*, 2016, **4**, 1950–1954.

234 H.-L. Liang, M. M. Bay, R. Vadrucci, C. H. Barty-King, J. Peng, J. J. Baumberg, M. F. L. D. Volder and S. Vignolini, *Nat. Commun.*, 2018, **9**, 4632.

235 G. Guidetti, S. Atifi, S. Vignolini and W. Y. Hamad, *Adv. Mater.*, 2016, **28**, 10042–10047.

236 B. Wang and A. Walther, *ACS Nano*, 2015, **9**, 10637–10646.

237 R. Bardet, N. Belgacem and J. Bras, *ACS Appl. Mater. Interfaces*, 2015, **7**, 4010–4018.

238 J. Pérez, J. Muñoz-Dorado, T. de la Rubia, J. Martínez, *Int. Microbiol.* 2002, **5**, 53-63.

239 K. Yao, Q. Meng, V. Bulone and Q. Zhou, *Adv. Mater.*,2017, **29**, 1701323.

240 K. M. Adstedt, V. V. Tsukruk, under submission.

241 E. Riande and E. Sáiz, *Dipole moments and birefringence of polymers*, Prentice Hall, 1992.

242 H. Janeschitz-Kriegl, *Polymer Melt Rheology and Flow Birefringence*, Springer Science & Business Media, 2012.

243 D. Meschede, Optics, Light, and Lasers: The Practical Approach to Modern Aspects of Photonics and Laser Physics, 2017, Wiley-VCH Verlag GmbH & Co. KGaA.

244 T. Hiratani, O. Kose, W. Y. Hamad and M. J. MacLachlan, *Mater. Horiz.*, 2018, **5**, 1076–1081.

245 J. Bergström, in *Mechanics of Solid Polymers*, ed. J. Bergström, William Andrew Publishing, 2015, pp. 19–114.

246 I. M. Daly, M. J. How, J. C. Partridge, S. E. Temple, N. J. Marshall, T. W. Cronin and N. W. Roberts, *Nat. Commun.*, 2016, **7**, 12140.

247 P. Tseng, B. Napier, S. Zhao, A. N. Mitropoulos, M. B. Applegate, B. Marelli, D. L. Kaplan and F. G. Omenetto, *Nat. Nanotechnol.*, 2017, **12**, 474–480.

248 D. Ye, P. Yang, X. Lei, D. Zhang, L. Li, C. Chang, P. Sun and L. Zhang, *Chem. Mater.*, 2018, **30**, 5175–5183.

249 D. Ye, Q. Cheng, Q. Zhang, Y. Wang, C. Chang, L. Li, H. Peng and L. Zhang, *ACS Appl. Mater. Interfaces*, 2017, **9**, 43154–43162.

250 Q. Liu and I. I. Smalyukh, *Sci. Adv.*, 2017, **3**, e1700981.

251 M. K. Hausmann, P. A. Rühs, G. Siqueira, J. Läuger, R. Libanori, T. Zimmermann and A. R. Studart, *ACS Nano*, 2018, **12**, 6926–6937.

252 A. S. Gladman, E. A. Matsumoto, R. G. Nuzzo, L. Mahadevan and J. A. Lewis, *Nat. Mater.*, 2016, **15**, 413.

253 N. Mittal, F. Ansari, K. Gowda.V, C. Brouzet, P. Chen, P. T. Larsson, S. V. Roth, F. Lundell, L. Wågberg, N. A. Kotov and L. D. Söderberg, *ACS Nano*, 2018, **12**, 6378–6388.

254 H. Zhu, S. Parvinian, C. Preston, O. Vaaland, Z. Ruan and L. Hu, *Nanoscale*, 2013, **5**, 3787–3792.

255 M. Nogi, S. Iwamoto, A. N. Nakagaito and H. Yano, *Adv. Mater.*, 2009, **21**, 1595–1598.

256 M. S. Toivonen, O. D. Onelli, G. Jacucci, V. Lovikka, O. J. Rojas, O. Ikkala and S. Vignolini, *Adv. Mater.*, 2018, **30**, 1704050.

257 S. Caixeiro, M. Peruzzo, O. D. Onelli, S. Vignolini and R. Sapienza, *ACS Appl. Mater. Interfaces*, 2017, **9**, 7885–7890.

258 S. Caixeiro, M. Peruzzo, O. D. Onelli, S. Vignolini and R. Sapienza, *ACS Appl. Mater. Interfaces*, 2017, **9**, 7885–7890.

259 Z. Fang, H. Zhu, C. Preston, X. Han, Y. Li, S. Lee, X. Chai, G. Chen and L. Hu, *J. Mater. Chem. C*, 2013, **1**, 6191–6197.

260 H. Yousefi, T. Nishino, M. Faezipour, G. Ebrahimi and A. Shakeri, *Biomacromolecules*, 2011, **12**, 4080–4085.

261 Y. Yao, J. Tao, J. Zou, B. Zhang, T. Li, J. Dai, M. Zhu, S. Wang, K. Kelvin Fu, D. Henderson, E. Hitz, J. Peng and L. Hu, *Energy Environ. Sci.*, 2016, **9**, 2278–2285.

262 S. Fink, *Holzforsch. - Int. J. Biol. Chem. Phys. Technol. Wood*, 2009, **46**, 403–408.

263 Y. Li, Q. Fu, S. Yu, M. Yan and L. Berglund, *Biomacromolecules*, 2016, **17**, 1358–1364.

264 M. Zhu, J. Song, T. Li, A. Gong, Y. Wang, J. Dai, Y. Yao, W. Luo, D. Henderson and L. Hu, *Adv. Mater.*, 2016, **28**, 5181–5187.

265 N. Vogel, S. Utech, G. T. England, T. Shirman, K. R. Phillips, N. Koay, I. B. Burgess, M. Kolle, D. A. Weitz and J. Aizenberg, *Proc. Natl. Acad. Sci.*, 2015, **112**, 10845–10850.

266 Y. Takeoka, S. Yoshioka, A. Takano, S. Arai, K. Nueangnoraj, H. Nishihara, M. Teshima, Y. Ohtsuka and T. Seki, *Angew. Chem. Int. Ed.*, 2013, **52**, 7261–7265.

267 M. D. Shawkey and G. E. Hill, *J. Exp. Biol.*, 2006, **209**, 1245–1250.

268 Y. Li, Z. Lu, H. Yin, X. Yu, X. Liu and J. Zi, *Phys. Rev. E*, 2005, **72**, 010902.

269 Q. Jiang, H. G. Derami, D. Ghim, S. Cao, Y.-S. Jun and S. Singamaneni, *J. Mater. Chem. A*, 2017, **5**, 18397–18402.

270 H. Gholami Derami, Q. Jiang, D. Ghim, S. Cao, Y. J. Chandar, J. J. Morrissey, Y.-S. Jun and S. Singamaneni, *ACS Appl. Nano Mater.*, 2019, **2**, 1092–1101.

271 M. Xiao, Y. Li, J. Zhao, Z. Wang, M. Gao, N. C. Gianneschi, A. Dhinojwala and M. D. Shawkey, *Chem. Mater.*, 2016, **28**, 5516–5521.

272 M. Kohri, Y. Nannichi, T. Taniguchi and K. Kishikawa, *J. Mater. Chem. C*, 2015, **3**, 720–724.

273 T.-F. Wu and J.-D. Hong, *Biomacromolecules*, 2015, **16**, 660–666.

274 M. Xiao, Y. Li, M. C. Allen, D. D. Deheyn, X. Yue, J. Zhao, N. C. Gianneschi, M. D. Shawkey and A. Dhinojwala, *ACS Nano*, 2015, **9**, 5454–5460.

275 M. Xiao, Z. Hu, Z. Wang, Y. Li, A. D. Tormo, N. L. Thomas, B. Wang, N. C. Gianneschi, M. D. Shawkey and A. Dhinojwala, *Sci. Adv.*, 2017, **3**, e1701151.

276 F. Caruso, R. A. Caruso and H. Möhwald, *Science,* 1998, **282**, 1111-1114.

277 R. Xiong, K. Hu, A. M. Grant, R. Ma, W. Xu, C. Lu, X. Zhang and V. V. Tsukruk, *Adv. Mater.*, 2016, **28**, 1501–1509.

278 J. J. Richardson, M. Björnmalm and F. Caruso, *Science*, **2015**, 348, 411.

279 K. Ariga, Y. Yamauchi, G. Rydzek, Q. Ji, Y. Yonamine, K. C.-W. Wu, and J. P. Hill, *Chem. Lett.* **2014**, 43, 36-68.

280 C. Jiang, S. Markutsya and V. V. Tsukruk, *Adv. Mater.*, **2004**, 16, 157-161.

281 V. Kozlovskaya, S., A. Sousa, M. Libera and S. A. Sukhishvili, *Macromolecules,* 2003, **36**, 8590-8592.

282 C. J. Ochs, G. K. Such, B. Städler and F. Caruso, *Biomacromolecules,* 2008, **9**, 3389-3396.

283 Z. P. Wang, Z. Q. Feng and C. Y. Gao, *Chem. Mater.* 2008*,* **20**, 4194-4199.

284 L. Zhai, A. J. Nolte, R. E. Cohen and M. F. Rubner, *Macromolecules*, 2004, **37**, 6113–6123.

285 D. P. Puzzo, L. D. Bonifacio, J. Oreopoulos, C. M. Yip, I. Manners and G. A. Ozin, *J. Mater. Chem.*, 2009, **19**, 3500–3506.

286 Z. Wu, D. Lee, M. F. Rubner and R. E. Cohen, *Small*, 2007, **3**, 1445–1451.

287 P. Kurt, D. Banerjee, R. E. Cohen and M. F. Rubner, *J. Mater. Chem.*, 2009, **19**, 8920–8927.

288 G. M. Nogueira, D. Banerjee, R. E. Cohen and M. F. Rubner, *Langmuir*, 2011, **27**, 7860–7867.

289 S. Vial, I. Pastoriza-Santos, J. Pérez-Juste and L. M. Liz-Marzán, *Langmuir*, 2007, **23***,* 4606-4611.

290 C. Jiang, S. Markutsy and V. V. Tsukruk, *Langmuir*, 2004, **20***,* 882-890.

291 J. Cho and F. Caruso, *Chem. Mater.,* 2005, **17***,* 4547-4553.

292 T. Franzl, T. A. Klar, S. Schietinger, A. L. Rogach and J. Feldmann, *Nano Lett.*, 2004, **4**,1599-1603.

293 T. A. Klar, T. Franzl, A. L. Rogach and J. Feldmann, *Adv. Mater.*, 2005, **17**, 769-773.

294 T. Franzl, D. S. Koktysh, T. A. Klar, A. L. Rogach and J. Feldmann, *Appl. Phys. Lett.*, 2001, **84**, 2904-2906.

295 E. Colusso, G. Perotto, Y. Wang, M. Sturaro, F. Omenetto and A. Martucci, *J. Mater. Chem. C*, 2017, **5**, 3924–3931.

296 P. Tzeng, D. J. Hewson, P. Vukusic, S. J. Eichhorn and J. C. Grunlan, *J. Mater. Chem. C*, 2015, **3**, 4260–4264.

297 R. Merindol, S. Diabang, O. Felix, T. Roland, C. Gauthier and G. Decher, *ACS Nano*, 2015, **9**, 1127–1136.

298 P. Podsiadlo, L. Sui, Y. Elkasabi, P. Burgardt, J. Lee, A. Miryala, W. Kusumaatmaja, M. R. Carman, M. Shtein, J. Kieffer, J. Lahann and N. A. Kotov, *Langmuir,* 2007, **23**, 7901–7906.

299 C. Nakamura, K. Manabe, M. Tenjimbayashi, Y. Tokura, K.-H. Kyung and S. Shiratori, *ACS Appl. Mater. Interfaces*, 2018, **10**, 22731−22738.

300 J. Lv, D. Ding, X. Yang, K. Hou, X. Miao, D. Wang, B. Kou, L. Huang and Z. Tang, *Angew. Chem. Int. Ed.*, 2019, **58**, 7783 –7787.

301 C. Zheng, Y. Shen, M. Liu, W. Liu, S. Wu and C. Jin, *ACS Nano*, 2019, **13**, 5583−5590.

302 Y. Kim, B. Yeom, O. Arteaga, S. J. Yoo, S.-G. Lee, J.-G. Kim and N. A. Kotov, *Nat. Mater.* 2016, **15**, 461-469.

303 A. Querejeta-Fernández, G. Chauve, M. Methot, J. Bouchard and E. Kumacheva, *J. Am. Chem. Soc.*, 2014, **136**, 4788–4793.

304 J. A. Kelly, M. Giese, K. E. Shopsowitz, W. Y. Hamad and M. J. MacLachlan, *Acc. Chem. Res.*, 2014, **47**, 1088–1096.

305 N. Vogel, M. Retsch, C.-A. Fustin, A. del Campo and U. Jonas, *Chem. Rev.*, 2015, **115**, 6265–6311.

306 H. Inan, M. Poyraz, F. Inci, M. A. Lifson, M. Baday, B. T. Cunningham and U. Demirci, *Chem. Soc. Rev.*, 2017, **46**, 366–388.

307 E. Kharlampieva, V. Kozlovskaya, R. Gunawidjaja, V. V. Shevchenko, R. Vaia, R. R. Naik, D. L. Kaplan and V. V. Tsukruk, *Adv. Funct. Mater.*, 2010, **20**, 840–846.

308 J. Olson, A. Manjavacas, L. Liu, W.-S. Chang, B. Foerster, N. S. King, M. W. Knight, P. Nordlander, N. J. Halas and S. Link, *Proc. Natl. Acad. Sci.*, 2014, **111**, 14348–14353.

309 Y. Gu, L. Zhang, J. K. W. Yang, S. Ping Yeo and C.-W. Qiu, *Nanoscale*, 2015, **7**, 6409–6419.

310 Y.-K. R. Wu, A. E. Hollowell, C. Zhang and L. J. Guo, *Sci. Rep.*, 2013, **3**, 1194.

311 P. K. Jain and M. A. El-Sayed, *Chem. Phys. Lett.*, 2010, **487**, 153–164.

312 J.-M. Guay, A. Calà Lesina, G. Côté, M. Charron, D. Poitras, L. Ramunno, P. Berini and A. Weck, *Nat. Commun.*, 2017, **8**, 16095.

313 X. Huang and M. A. El-Sayed, *J. Adv. Res.*, 2010, **1**, 13–28.

314 N. Koay, I. B. Burgess, T. M. Kay, B. A. Nerger, M. Miles-Rossouw, T. Shirman, T. L. Vu, G. England, K. R. Phillips, S. Utech, N. Vogel, M. Kolle and J. Aizenberg, *Opt. Express*, 2014, **22**, 27750–27768.

315 F. G. Omenetto and D. L. Kaplan, *Nat. Photonics*, 2008, **2**, 641–643.

316 D. Lin, H. Tao, J. Trevino, J. P. Mondia, D. L. Kaplan, F. G. Omenetto and L. D. Negro, *Adv. Mater.*, 2012, **24**, 6088–6093.

317 A. Querejeta-Fernández, B. Kopera, K. S. Prado, A. Klinkova, M. Methot, G. Chauve, J. Bouchard, A. S. Helmy and E. Kumacheva, *ACS Nano*, 2015, **9**, 10377–10385.

318 Q. Liu, M. G. Campbell, J. S. Evans and I. I. Smalyukh, *Adv. Mater.*, 2014, **26**, 7178–7184.

319 R. R. Silva, C. T. Dominguez, M. V. Santos, R. Barbosa-Silva, M. Cavicchioli, L. M. Christovan, L. S. A. Melo, A. S. L. Gomes, C. B. Araújo, S. J. L. Ribeiro, *J. Mater. Chem. C,* 2013, **1**, 7181-7190.

320 H. Qi, K. E. Shopsowitz, W. Y. Hamad and M. J. MacLachlan, *J. Am. Chem. Soc.*, 2011, **133**, 3728–3731.

321 R. C. Somers, M. G. Bawendi and D. G. Nocera, *Chem. Soc. Rev.*, 2007, **36**, 579–591.

322 X. Liu, X. Zhang, R. Wu, H. Shen, C. Zhou, X. Zhang, L.-J. Guo and L. S. Li, *Chem. Eng. J.*, 2017, **324**, 19–25.

323 S. Zhu, Y. Song, X. Zhao, J. Shao, J. Zhang and B. Yang, *Nano Res.*, 2015, **8**, 355–381.

324 D. Bera, L. Qian, T.-K. Tseng and P. H. Holloway, *Materials*, 2010, **3**, 2260–2345.

325 P. Lodahl, A. Floris van Driel, I. S. Nikolaev, A. Irman, K. Overgaag, D. Vanmaekelbergh and W. L. Vos, *Nature*, 2004, **430**, 654–657.

326 H. Zheng, W. Li, W. Li, X. Wang, Z. Tang, S. X.-A. Zhang and Y. Xu, *Adv. Mater.*, 2018, **30**, 1705948.

327 Y. Geng, A. Trajkovska, S. W. Culligan, J. J. Ou, H. M. P. Chen, D. Katsis and S. H. Chen, *J. Am. Chem. Soc.*, 2003, **125**, 14032–14038.

328 Y. Yang, R. C. da Costa, D.-M. Smilgies, A. J. Campbell and M. J. Fuchter, *Adv. Mater.*, 2013, **25**, 2624–2628.

329 S. N. Baker and G. A. Baker, *Angew. Chem. Int. Ed.*, 2010, **49**, 6726–6744.

330 E. Lizundia, T.-D. Nguyen, J. L. Vilas, W. Y. Hamad and M. J. MacLachlan, *Mater. Chem. Front.*, 2017, **1**, 979–987.

331 H. Zheng, B. Ju, X. Wang, W. Wang, M. Li, Z. Tang, S. X.-A. Zhang and Y. Xu, *Adv. Opt. Mater.*, 2018, **6**, 1801246.

332 R. Xiong, S. Yu, M. J. Smith, J. Zhou, M. Krecker, L. Zhang, D. Nepal, T. J. Bunning, V. V. Tsukruk, *ACS Nano,* **2019**, *13*, 9074–9081.

333 K. E. Shopsowitz, H. Qi, W. Y. Hamad and M. J. MacLachlan, *Nature*, 2010, **468**, 422–425.

334 K. E. Shopsowitz, W. Y. Hamad and M. J. MacLachlan, *Angew. Chem. Int. Ed.*, 2011, **50**, 10991–10995.

335 J. A. Kelly, A. M. Shukaliak, C. C. Cheung, K. E. Shopsowitz, W. Y. Hamad and M. J. MacLachlan, *Angew. Chem. Int. Ed.*, 2013, **52**, 8912–8916.

336 K. E. Shopsowitz, A. Stahl, W. Y. Hamad and M. J. MacLachlan, *Angew. Chem. Int. Ed.*, 2012, **51**, 6886–6890.

337 T.-D. Nguyen, W. Y. Hamad and M. J. MacLachlan, *Adv. Funct. Mater.*, 2014, **24**, 777–783.

338 Y. Li, J. Jun-Yan Suen, E. Prince, E. M. Larin, A. Klinkova, H. Thérien-Aubin, S. Zhu, B. Yang, A. S. Helmy, O. D. Lavrentovich and E. Kumacheva, *Nat. Commun.*, 2016, **7**, 12520.

339 S. H. Yun and S. J. J. Kwok, *Nat. Biomed. Eng.*, 2017, **1**, 0008.

340 M. Humar, S. J. J. Kwok, M. Choi, A. K. Yetisen, S. Cho and S.-H. Yun, *Nanophotonics*, 2016, **6**, 414–434.

341 T. Sakimoto, M. I. Rosenblatt and D. T. Azar, *The Lancet*, 2006, **367**, 1432–1447.

342 A. Bansal, F. Yang, T. Xi, Y. Zhang and J. S. Ho, *Proc. Natl. Acad. Sci.*, 2018, **115**, 1469–1474.

343 T. Bruegmann, T. van Bremen, C. C. Vogt, T. Send, B. K. Fleischmann and P. Sasse, *Nat. Commun.*, 2015, **6**, 7153.

344 A. V. Kravitz, B. S. Freeze, P. R. Parker, K. Kay, M. T. Thwin, K. Deisseroth and A. C. Kreitzer, *Nature*, 2010, **466**, 622.

345 R. L. Rungta, B.-F. Osmanski, D. Boido, M. Tanter and S. Charpak, *Nat. Commun.*, 2017, **8**, 14191.

346 S. Chen, A. Z. Weitemier, X. Zeng, L. He, X. Wang, Y. Tao, A. J. Huang, Y. Hashimotodani, M. Kano and H. Iwasaki, *Science*, 2018, **359**, 679–684.

347 W. Teng, Y. Huang, J. Cappello and X. Wu, *J. Phys. Chem. B*, **2011**, 115, 1608-1615.

348 S. T. Parker, P. Domachuk, J. Amsden, J. Bressner, J. A. Lewis, D. L. Kaplan and F. G. Omenetto, *Adv. Mater.*, 2009, **21**, 2411–2415.

349 X. Qiao, Z. Qian, J. Li, H. Sun, Y. Han, X. Xia, J. Zhou, C. Wang, Y. Wang and C. Wang, *ACS Appl. Mater. Interfaces*, 2017, **9**, 14665–14676.

350 Q. Li, Y. Jia, L. Dai, Y. Yang and J. Li, *ACS Nano*, 2015, **9**, 2689–2695.

351 J. Kim, T. H. Han, Y.-I. Kim, J. S. Park, J. Choi, D. G. Churchill, S. O. Kim and H. Ihee, *Adv. Mater.*, 2010, **22**, 583–587.

352 Z. Gan, X. Wu, X. Zhu and J. Shen, *Angew. Chem. Int. Ed.*, 2013, **52**, 2055–2059.

353 L. Adler-Abramovich, D. Aronov, P. Beker, M. Yevnin, S. Stempler, L. Buzhansky, G. Rosenman and E. Gazit, *Nat. Nanotechnol.*, 2009, **4**, 849.

354 S. L. Jacques, *Phys. Med. Biol.*, 2013, **58**, R37.

355 A. Handelman, N. Lapshina, B. Apter and G. Rosenman, *Adv. Mater.*, 2018, **30**, 1705776.

356 H. Xin, Y. Li, X. Liu and B. Li, *Nano Lett.*, 2013, **13**, 3408–3413.

357 A. Bezryadina, T. Hansson, R. Gautam, B. Wetzel, G. Siggins, A. Kalmbach, J. Lamstein, D. Gallardo, E. J. Carpenter and A. Ichimura, *Phys. Rev. Lett.*, 2017, **119**, 058101.

358 R. El-Ganainy, D. N. Christodoulides, Z. H. Musslimani, C. Rotschild and M. Segev, *Opt. Lett.*, 2007, **32**, 3185–3187.

359 J. S. T. Gongora and A. Fratalocchi, *Opt. Lasers Eng.*, 2016, **76**, 40–44.

360 N. Schuergers, T. Lenn, R. Kampmann, M. V. Meissner, T. Esteves, M. Temerinac-Ott, J. G. Korvink, A. R. Lowe, C. W. Mullineaux and A. Wilde, *Elife*, 2016, **5**, e12620.

361 E. De Tommasi, A. C. De Luca, L. Lavanga, P. Dardano, M. De Stefano, L. De Stefano, C. Langella, I. Rendina, K. Dholakia and M. Mazilu, *Opt. Express*, 2014, **22**, 27214–27227.

362 L. Miccio, P. Memmolo, F. Merola, P. A. Netti and P. Ferraro, *Nat. Commun.*, 2015, **6**, 6502.

363 C. Wang, J. Luan, S. Tadepalli, K.-K. Liu, J. J. Morrissey, E. D. Kharasch, R. R. Naik and S. Singamaneni, *ACS Appl. Mater. Interfaces*, 2016, **8**, 26493–26500.

364 J. Zhang, E. Pritchard, X. Hu, T. Valentin, B. Panilaitis, F. G. Omenetto and D. L. Kaplan, *Proc. Natl. Acad. Sci.*, 2012, **109**, 11981–11986.

365 Q. Lu, X. Wang, X. Hu, P. Cebe, F. Omenetto and D. L. Kaplan, *Macromol. Biosci.*, 2010, **10**, 359–368.

366 Z. Chen, A. Taflove and V. Backman, *Opt. Express*, 2004, **12**, 1214–1220.

367 A. Heifetz, S.-C. Kong, A. V. Sahakian, A. Taflove and V. Backman, *J. Comput. Theor. Nanosci.*, 2009, **6**, 1979–1992.

368 C. B. Lin, Z.-H. Huang and C.-Y. Liu, *Opt. Lett.*, 2019, **44**, 667–670.

369 J. N. Monks, B. Yan, N. Hawkins, F. Vollrath and Z. Wang, *Nano Lett.*, 2016, **16**, 5842–5845.

370 Z. Wang, W. Guo, L. Li, B. Luk'yanchuk, A. Khan, Z. Liu, Z. Chen and M. Hong, *Nat. Commun.*, 2011, **2**, 218.

371 Z. Wang, *Nanoscience*, 2016, **3**, 193–210.

372 H. Tao, J. M. Kainerstorfer, S. M. Siebert, E. M. Pritchard, A. Sassaroli, B. J. Panilaitis, M. A. Brenckle, J. J. Amsden, J. Levitt and S. Fantini, *Proc. Natl. Acad. Sci.*, 2012, **109**, 19584–19589.

373 H. M. Whitney, M. Kolle, P. Andrew, L. Chittka, U. Steiner and B. J. Glover, *Science*, 2009, **323**, 130–133.

374 B. D. Wilts, K. Michielsen, H. De Raedt and D. G. Stavenga, *Interface Focus*, 2011, **2**, 681–687.

375 P. Vukusic, J. R. Sambles and C. R. Lawrence, *Proc. R. Soc. Lond. B Biol. Sci.*, 2004, **271**, S237–S239.

376 J. Zi, X. Yu, Y. Li, X. Hu, C. Xu, X. Wang, X. Liu and R. Fu, *Proc. Natl. Acad. Sci.*, 2003, **100**, 12576–12578.

377 E. Lee, J. Miyazaki, S. Yoshioka, H. Lee and S. Sugita, *Ornithol. Sci.*, 2012, **11**, 59–64.

378 S. Yoshioka, B. Matsuhana, S. Tanaka, Y. Inouye, N. Oshima and S. Kinoshita, *J. R. Soc. Interface*, 2010, **8**, 56–66.

379 S. Torquato, T. M. Truskett and P. G. Debenedetti, *Phys. Rev. Lett.*, 2000, **84**, 2064.

380 Y. Y. Diao, X. Y. Liu, G. W. Toh, L. Shi and J. Zi, *Adv. Funct. Mater.*, 2013, **23**, 5373–5380.

381 B. Richter, D. Goldston, G. Crabtree, L. Glicksman, D. Goldstein, D. Greene, D. Kammen, M. Levine, M. Lubell and M. Savitz, *Rev. Mod. Phys.*, 2008, **80**, S1.

382 H. Coles and S. Morris, *Nat. Photonics*, 2010, **4**, 676.

383 Y. Cao, L. Lewis, W. Y. Hamad and M. J. MacLachlan, *Adv. Mater.*, **2019**, 1808186, DOI: doi.org/10.1002/adma.201808186.

384 Z. Sun, F. Lv, L. Cao, L. Liu, Y. Zhang and Z. Lu, *Angew. Chem. Int. Ed.*, 2015, **54**, 7944–7948.

385 Z. Q. Liu, D. Jiao and Z. F. Zhang, *Biomaterials*, 2015, **65**, 13–21.

386 N. A. Pattanashetti, G. B. Heggannavar and M. Y. Kariduraganavar, *Procedia Manuf.*, 2017, **12**, 263–279.

387 T.-D. Nguyen, B. U. Peres, R. M. Carvalho and M. J. MacLachlan, *Adv. Funct. Mater.*, 2016, **26**, 2875–2881.

388 Y.-D. He, Z.-L. Zhang, J. Xue, X.-H. Wang, F. Song, X.-L. Wang, L.-L. Zhu and Y.-Z. Wang, *ACS Appl. Mater. Interfaces*, 2018, **10**, 5805–5811.

389 S. N. Fernandes, P. L. Almeida, N. Monge, L. E. Aguirre, D. Reis, C. L. P. de Oliveira, A. M. F. Neto, P. Pieranski and M. H. Godinho, *Adv. Mater.*, 2017, **29**, 1603560.

390 S. Caveney, *Proc. R. Soc. Lond. B Biol. Sci.*, 1971, **178**, 205–225.

391 M. V. Santos, A. Tercjak, J. Gutierrez, H. S. Baruda, M. Napoli, M. Nalina, S.J.L. Ribeiro, *Carbohyd. Polym.*, 2017, **168**, 346–355.

392 T. Wu, J. Li, J. Li, S. Ye, J. Wei and J. Guo, *J. Mater. Chem. C*, 2016, **4**, 9687–9696.

393 J. Y. Wang, Y. Cao, Y. Feng, F. Yin and J. P. Gao, *Adv. Mater.*, 2007, **19**, 3865–3871.

394 H. Xing, J. Li, J. Guo and J. Wei, *J. Mater. Chem. C*, 2015, **3**, 4424–4430.

395 L. Phan, W. G. Walkup, D. D. Ordinario, E. Karshalev, J.-M. Jocson, A. M. Burke and A. A. Gorodetsky, *Adv. Mater.*, 2013, **25**, 5621–5625.

396 F. Fu, L. Shang, Z. Chen, Y. Yu and Y. Zhao, *Sci. Robot.*, 2018, **3**, eaar8580.

397 P. Liu, T. Sheng, Z. Xie, J. Chen and Z. Gu, *ACS Appl. Mater. Interfaces*, 2018, **10**, 29378–29384.

398 H. Shafiee, E. A. Lidstone, M. Jahangir, F. Inci, E. Hanhauser, T. J. Henrich, D. R. Kuritzkes, B. T. Cunningham and U. Demirci, *Sci. Rep.*, 2014, **4**, 4116.

399 J.-N. Liu, Q. Huang, K.-K. Liu, S. Singamaneni and B. T. Cunningham, *Nano Lett.*, 2017, **17**, 7569–7577.

400 S. Chakravarty, B. Gogoi, B. B. Mandal, N. Bhardwaj and N. S. Sarma, *Biosens. Bioelectron.*, 2018, **112**, 18–22.

401 Y. Yang, Z. Shao, X. Chen and P. Zhou, *Biomacromolecules*, 2004, **5**, 773–779.

402 J. Chi, B. Gao, M. Sun, F. Zhang, E. Su, H. Liu and Z. Gu, *Anal. Chem.*, 2017, **89**, 7727–7733.

403 J. Chi, C. Shao, X. Du, H. Liu and Z. Gu, *ACS Appl. Mater. Interfaces*, 2018, **10**, 39144–39150.

404 J. I. L. Chen, G. von Freymann, S. Yeun Choi, V. Kitaev and G. A. Ozin, *J. Mater. Chem.*, 2008, **18**, 369–373.

405 Y. Xu, X. Zhang, C. Luan, H. Wang, B. Chen and Y. Zhao, *Biosens. Bioelectron.*, 2017, **87**, 264–270.

406 F. Fu, L. Shang, F. Zheng, Z. Chen, H. Wang, J. Wang, Z. Gu and Y. Zhao, *ACS Appl. Mater. Interfaces*, 2016, **8**, 13840–13848.

407 Y. Zhao, X. Zhao and Z. Gu, *Adv. Funct. Mater.*, 2010, **20**, 2970–2988.

408 B. Zhang, Y. Cai, L. Shang, H. Wang, Y. Cheng, F. Rong, Z. Gu and Y. Zhao, *Nanoscale*, 2016, **8**, 3841–3847.

[409] L. Shang, F. Fu, Y. Cheng, H. Wang, Y. Liu, Y. Zhao and Z. Gu, *J. Am. Chem. Soc.*, 2015, **137**, 15533–15539.

[410] P. Liu, T. Sheng, Z. Xie, J. Chen, and Z. Gu, *ACS Appl. Mater. Interfaces* 2018, **10**, 29378-29384.

[411] H. Ko, S. Singamaneni and V. V. Tsukruk, *Small*, 2008, **4**, 1576–1599.

[412] C. H. Lee, L. Tian and S. Singamaneni, *ACS Appl. Mater. Interfaces*, 2010, **2**, 3429–3435.

[413] C. H. Lee, M. E. Hankus, L. Tian, P. M. Pellegrino and S. Singamaneni, *Anal. Chem.*, 2011, **83**, 8953–8958

[414] K. Kneipp, H. Kneipp, V. B. Kartha, R. Manoharan, G. Deinum, I. Itzkan, R. R. Dasari and M. S. Feld, *Phys. Rev. E*, 1998, **57**, R6281–R6284.

[415] C. J. Johnson, N. Zhukovsky, A. E. G. Cass and J. M. Nagy, *PROTEOMICS*, 2008, **8**, 715–730.

[416] G. V. P. Kumar, R. Selvi, A. H. Kishore, T. K. Kundu and C. Narayana, *J. Phys. Chem. B*, 2008, **112**, 6703–6707.

[417] E. Bailo and V. Deckert, *Angew. Chem. Int. Ed.*, 2008, **47**, 1658–1661.

[418] A. F. de Oliveira, I. D. de A. O. Santos, S. B. Cartaxo, R. A. Bitar, M. M. S. e S. Enokihara, H. da S. Martinho, A. A. Martin and L. M. Ferreira, *Acta Cir. Bras.*, 2010, **25**, 434–439.

[419] L. Wu, W. Wang, W. Zhang, H. Su, Q. Liu, J. Gu, T. Deng and D. Zhang, *NPG Asia Mater.*, 2018, **10**, e462.

[420] G. Song, H. Zhou, J. Gu, Q. Liu, W. Zhang, H. Su, Y. Su, Q. Yao and D. Zhang, *J. Mater. Chem. B*, 2017, **5**, 1594–1600.

[421] D. Yan, L. Qiu, M. Xue, Z. Meng and Y. Wang, *Mater. Des.*, 2019, **165**, 107601.

[422] Z. Yan, M. Xue, Q. He, W. Lu, Z. Meng, D. Yan, L. Qiu, L. Zhou and Y. Yu, *Anal. Bioanal. Chem.* 2016, **408**, 8317-8323.

[423] J. Barber, *Chem. Soc. Rev.*, 2009, **38**, 185–196.

[424] S. Caffarri, K. Broess, R. Croce and H. van Amerongen, *Biophys. J.*, 2011, **100**, 2094–2103.

[425] E. Jin Son, J. Hong Kim, K. Kim and C. Beum Park, *J. Mater. Chem. A*, 2016, **4**, 11179–11202.

[426] R. E. Blankenship, *Plant Physiol.*, 2010, **154**, 434–438.

[427] R. E. Blankenship, D. M. Tiede, J. Barber, G. W. Brudvig, G. Fleming, M. Ghirardi, M. R. Gunner, W. Junge, D. M. Kramer, A. Melis, T. A. Moore, C. C. Moser, D. G. Nocera, A. J. Nozik, D. R. Ort, W. W. Parson, R. C. Prince and R. T. Sayre, *Science*, 2011, **332**, 805–809.

[428] Y. Liu, K. Ai and L. Lu, *Chem. Rev.*, 2014, **114**, 5057–5115.

[429] H. Lee, S. M. Dellatore, W. M. Miller and P. B. Messersmith, *Science*, 2007, **318**, 426–430.

[430] J. H. Kim, M. Lee and C. B. Park, *Angew. Chem.*, 2014, **126**, 6482–6486.

[431] J. Yang, G.-Q. Qi, L.-S. Tang, R.-Y. Bao, L. Bai, Z.-Y. Liu, W. Yang, B.-H. Xie and M.-B. Yang, *J. Mater. Chem. A*, 2016, **4**, 9625–9634.

[432] A. Xie, K. Zhang, F. Wu, N. Wang, Y. Wang and M. Wang, *Catal. Sci. Technol.*, 2016, **6**, 1764–1771.

[433] M. Lee, J. U. Kim, J. S. Lee, B. I. Lee, J. Shin and C. B. Park, *Adv. Mater.*, 2014, **26**, 4463–4468.

[434] M. Lee, J. U. Kim, K. J. Lee, S. Ahn, Y.-B. Shin, J. Shin and C. B. Park, *ACS Nano*, 2015, **9**, 6206–6213.

[435] W. Shang and T. Deng, *Nat. Energy*, 2016, **1**, 16133.

[436] H. Ghasemi, G. Ni, A. M. Marconnet, J. Loomis, S. Yerci, N. Miljkovic and G. Chen, *Nat. Commun.*, 2014, **5**, 4449.

[437] Q. Jiang, L. Tian, K.-K. Liu, S. Tadepalli, R. Raliya, P. Biswas, R. R. Naik and S. Singamaneni, *Adv. Mater.*, 2016, **28**, 9400–9407.

[438] L. Tian, J. Luan, K.-K. Liu, Q. Jiang, S. Tadepalli, M. K. Gupta, R. R. Naik and S. Singamaneni, *Nano Lett.*, 2016, **16**, 609–616.

[439] M. Zhu, Y. Li, F. Chen, X. Zhu, J. Dai, Y. Li, Z. Yang, X. Yan, J. Song, Y. Wang, E. Hitz, W. Luo, M. Lu, B. Yang and L. Hu, *Adv. Energy Mater.*, 2018, **8**, 1701028.

[440] Q. Jiang, H. G. Derami, D. Ghim, S. Cao, Y. Jun and S. Singamaneni, *J. Mater. Chem. A*, 2017, **5**, 18397-18402.

[441] N. Mittal, R. Jansson, M. Widhe, T. Benselfelt, K. M. O. Håkansson, F. Lundell, M. Hedhammar and L. D. Söderberg, *ACS Nano*, 2017, **11**, 5148–5159.

[442] J. Jin, D. Lee, H.-G. Im, Y. C. Han, E. G. Jeong, M. Rolandi, K. C. Choi and B.-S. Bae, *Adv. Mater.*, 2016, **28**, 5169–5175.

[443] D.-H. Kim, J. Viventi, J. J. Amsden, J. Xiao, L. Vigeland, Y.-S. Kim, J. A. Blanco, B. Panilaitis, E. S. Frechette, D. Contreras, D. L. Kaplan, F. G. Omenetto, Y. Huang, K.-C. Hwang, M. R. Zakin, B. Litt and J. A. Rogers, *Nat. Mater.*, 2010, **9**, 511–517.

444 H. Zhu, Z. Xiao, D. Liu, Y. Li, N. J. Weadock, Z. Fang, J. Huang and L. Hu, *Energy Environ. Sci.*, 2013, **6**, 2105–2111.

445 Q. Wang, J. Sun, Q. Yao, C. Ji, J. Liu and Q. Zhu, *Cellulose*, 2018, **25**, 4275–4301.

446 V. Kuzmenko, E. Karabulut, E. Pernevik, P. Enoksson and P. Gatenholm, *Carbohydr. Polym.*, 2018, **189**, 22–30.

447 L. Dai, T. Cheng, C. Duan, W. Zhao, W. Zhang, X. Zou, J. Aspler and Y. Ni, *Carbohydr. Polym.*, 2019, **203**, 71–86.

448 https://www.lexus.eu/discover-lexus/lexus-news/lc-structural-blue.

TOC